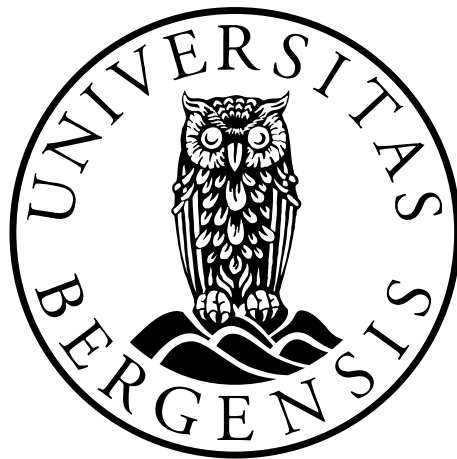# Characterization and Tracking of Melanoma and Lung Brain Metastasis-Derived Extracellular Vesicles *in vitro*

Sunniva Juliussen

This thesis is submitted in partial fulfilment of the requirements for the degree of Master in Biomedical Sciences - Biomedicine

Department of Biomedicine

University of Bergen

Spring 2024

Acknowledgements

Bergen, May 2024
Sunniva Juliussen

Table of Contents

Abbreviations

AFC = Automatic Fraction Collector
APC = antigen-presenting cell
ARRDC1 = arrestin domain-containing protein 1
BBB = blood-brain barrier
BC = breast cancer
BM = brain metastasis
BRAF = v-Raf murine sarcoma viral oncogene homolog B
CAF = cancer-associated fibroblast
CAM = cell adhesion molecules
CNS = central nervous system
CSF = cerebrospinal fluid
CT = computed tomography
CTC = circulating tumor cells
CTLA-4 = cytotoxic T-lymphocyte-associated protein 4
DC = dendritic cell
DLS = dynamic light scattering
DMEM = Dulbecco's Modified Eagle Medium
DMSO = dimethyl sulfoxide
DTC = disseminated tumor cell
EC = endothelial cell
ECM = extracellular matrix
EGF = epidermal growth factor
EGFR = epidermal growth factor receptor
EMT = epithelial-mesenchymal transition
ER = endoplasmic reticulum
ERe = estrogen receptor
ESCRT = endosomal sorting complex required for transport
EV = extracellular vesicle
FA = flip angle
FBS = fetal bovine serum
FLAIR = fluid attenuated inversion recovery
FLOT1 = flotillin-1
FOV = field of view
HIF = hypoxia-inducible factor
HER2 = human epidermal growth factor receptor 2
HRP = horseradish peroxidase
IGF2 = insulin-like growth factor II
IHC = immunohistochemistry
ILV = intraluminal vesicle
KRAS = Kirsten rat sarcoma viral oncogene homolog
LBM = lung cancer brain metastasis
LDS = lithium dodecyl sulfate
mAb = mouse antibody
MAPK/ERK = mitogen activated protein kinase pathway/extracellular signal-regulated kinase
MBM = melanoma brain metastasis
MDSC = myeloid-derived suppressor cells
MHC = major histological compatibility complex
miRNA = microRNA

MISEV = Minimal Information for Studies of Extracellular Vesicles
MMP = matrix metalloproteinase
MNP = magnetic nanoparticle
MRI = magnetic resonance imaging
mRNA = messenger RNA
MVB = multivesicular bodies
ncRNA = non-coding RNA
NK = natural killer cell
NSCLC = non-small cell lung cancer
NTA = nanoparticle tracking analysis
OS = overall survival
PBS = phosphate buffer saline
PC = pericyte
PD-L1 = programmed death-ligand 1
PD-1 = programmed cell death protein 1
PDGF = platelet derived growth factor B
PET = positron emission tomography
PFA = paraformaldehyde
PMN = premetastatic niche
PR = progesterone receptor
qEV = size exclusion columns for EV isolation
REC = Regional Ethical Committee
RF = radiofrequency
rRNA = ribosomal RNA
ROS = reactive oxygen species
RT = room temperature
SCLC = small cell lung cancer
SDS-PAGE = sodium dodecyl sulfate polyacrylamide gel electrophoresis
SEC = size exclusion chromatography
sEV = small extracellular vesicle
SNARE = N-ethylmaleimide-sensitive factor attachment protein receptor
SPION = superparamagnetic iron oxide nanoparticle
SR-SIM = super-resolution structured illumination microscopy
SRS = stereotactic radiosurgery
STR = short tandem repeat
T1 = relaxation time of longitudinal magnetization
T2 = relaxation time of transverse magnetization
T1w = T1-weighted image
T2w = T2-weighted image
TAM = tumor-associated macrophages
TE = echo time
TEM = transmission electron microscopy
TIL = tumor infiltrating lymphocyte
TJ = tight junction
TME = tumor microenvironment
TNF = tumor necrosis factor
TR = repetition time
TSG = tumor susceptibility gene
VEGF = vascular endothelial growth factor
WBRT = whole-brain radiotherapy

Summary

Brain metastasis (BM) occurs when cancer cells from a primary tumor elsewhere in the body spread to the brain. It poses significant challenges in cancer treatment due to its aggressive nature and limited therapeutic options, with overall survival (OS) is reported to be 6 months or less. Recent research has focused on the role of intercellular communication in metastasis development, aiming to deepen our understanding of this process and develop novel therapeutic approaches. Extracellular vesicles (EVs) derived from primary tumors have emerged as key players in the formation of a pre-metastatic niche (PMN), disrupting the blood-brain barrier (BBB), and stimulating the proliferation of metastatic tumor cells.

A comparative analysis of EV isolation through differential centrifugation and size exclusion chromatography (SEC) was conducted. The findings revealed that SEC outperformed differential centrifugation in several aspects. SEC yielded up to 20 times more EVs compared to differential centrifugation based on EV protein measurements. Additionally, SEC was time-saving and required less conditioned culture medium, making it a more efficient and practical method for EV isolation. EVs derived from melanoma BM cell lines H16 and H10, as well as from the lung BM cell line LBM1, were characterized using SEC. Differential centrifugation was exclusively used for characterizing EVs derived from H16.

Labeling EVs with superparamagnetic iron oxide nanoparticles (SPIONs) facilitates their tracking using magnetic resonance imaging (MRI). By tracking SPION-labeled EVs, MRI provides a non-invasive method for researchers to visualize the distribution and behavior of the labeled EVs within the body. Electroporation was initially attempted for EV labeling but proved unsuccessful. However, successful labeling of LBM1- and H16-derived EVs was achieved through cell incubation with dextran-coated and uncoated SPIONs at concentrations ranging from 50 to 200 µg/mL prior to EV isolation. The findings indicated that uncoated SPIONs were the most optimal for labeling at high concentrations.

Lastly, agar phantoms containing SPION-labeled and unlabeled LBM1 cells were created and subjected to MRI. Different concentrations of labeled and unlabeled cells were imaged, revealing that a concentration of 4000 labeled cells/µL was excessive. Moreover, SPION-labeled EVs derived from LBM1 were effectively visualized in agar phantoms using MRI.

1.   Introduction

1.1   Cancer

Cancer is a large group of diseases that is marked by the uncontrolled proliferation of cells that have evaded central endogenous control mechanisms[1]. The World Health Organization states that cancer is a leading global cause of death, responsible for nearly 10 million deaths worldwide in 2020. The most common types of cancers include breast, lung, colon, prostate, and skin, but there are nearly 200 different types of cancer[2]. Risk factors can be categorized into several groups, such as lifestyle factors, environmental exposures, genetic factors, and infectious agents[3]. The risk for developing cancer can be reduced by for instance avoiding the use of tobacco, maintaining a healthy diet, reducing exposure to environmental carcinogens, vaccination, and regular screening. It is estimated that 30-50% of cancers can be prevented by avoiding risk factors[4]. Treatment varies by cancer type and includes surgery, radiotherapy, chemotherapy, immunotherapy, hormone therapy, and targeted therapy. In cases where curative treatments fall short in managing cancer, the implementation of palliative care becomes crucial, relieving symptoms and enhancing the overall quality of life. Hence, the early diagnosis of cancer and the implementation of screening are important as it significantly enhances survival rates[4,5].

Tumors, also known as neoplasms, are categorized as either benign or malignant based on their distinct characteristics. Benign tumors exhibit slow growth, well-defined borders, and a lack of invasion into surrounding tissues or other parts of the body. Typically, benign tumors pose minimal risk to surrounding tissues unless their growth exerts pressure or compression on vital organs. Certain types of benign tumors, however, have the potential to transform into malignant tumors. Close monitoring is necessary for such cases, and surgical removal may be recommended as a preventive measure[6,7]. In contrast, malignant (cancerous) tumors tend to grow rapidly, displaying irregular borders[8]. They frequently invade and destroy surrounding tissues and possesses the capability to spread through blood vessels, lymph nodes, or penetrate the immediate surrounding tissue.

1.2   Metastasis

Most cells of the body stay within a specific tissue or organ, and organs have well-demarked boundaries defined by surrounding basement membranes. A characteristic of cancer is the

rapid development of abnormal cells that have the ability to grow beyond their typical boundaries, break the protective basement membrane, and subsequently invade nearby areas of the body, eventually spreading to other organs through a process called metastasis[9]. The word metastasis origins from the Greek word *Methistanai*, meaning a "rapid transition from one point to another"[10]. Hanahan and Weinberg stated that "activating invasion and metastasis" is a Hallmark of Cancer[6], and tumor metastasis is responsible for about 90% of cancer-related deaths[11]. Interactions with the tumor microenvironment (TME) enable metastasizing cancer cells to handle stromal challenges, establish themselves, and colonize. These features of cancer cells are driven by genetic and epigenetic changes occurring both within the tumor cells and in their surrounding environment. Despite metastasis being the main contributor to failure of therapy and eventual mortality, our understanding of this process remains limited and incomplete[4,12,13]. This underscores the importance of prioritizing and exploring the idea of metastasis in research to improve cancer therapy outcomes. Finding ways to target the metastatic processes to prevent or slow down the spread of cancer is therefore the key goal for many researchers.

The most common sites for metastatic spread are to lung, liver, bones, and brain (this is discussed further in chapter 1.5.3). Symptoms of metastatic cancer can vary widely and may be minimal, depending on the location of the metastasis. For instance, brain metastasis (BM) may lead to headaches, speech difficulties, nausea, difficulty in walking, and disorientation. Liver metastasis may present with symptoms such as abdominal pain, loss of appetite, nausea, ascites, or jaundice. The diagnosis of metastatic cancer commonly involves imaging techniques including computed tomogram (CT) scans, X-ray, or magnetic resonance imaging (MRI), complemented with analysis of blood samples[14]. While recent improvements in immunotherapy highlight the importance of targeting molecules and cells within tumor and metastatic microenvironments, the development of better tools to identify patients at risk for metastasis and improve initial treatments to prevent metastatic development is still required. One potential avenue is focusing on therapies that target premetastatic niches (PMNs), which are distant, inflammation-induced environments favorable for tumor metastasis, supported by tumor-secreted soluble factors and extracellular vesicles (EVs)[15].

1.3   The Metastatic Niche

The metastatic niche refers to the immediate microenvironment surrounding disseminated tumor cells (DTCs), ostensibly metastatic cells, and plays a role in facilitating cell growth. Steven Paget's "seed and soil" hypothesis proposed that metastatic growth required an interaction between the tumor cells ("seed") and a compatible tissue/organ ("soil") to facilitate their growth. This concept laid the foundation for the metastatic niche, which has been validated through recent studies[16,17]. Before the arrival of tumor cells, the secondary site where DTCs will eventually invade and proliferate forms what is known as the PMN. The establishment and characteristics of the PMN involve several key factors. These include remodeling of the extracellular matrix (ECM) to provide a scaffold that facilitates the attachment and invasion of tumor cells[18]. Immune cells, including macrophages and neutrophils, are recruited to the niche and reprogrammed to create an immunosuppressive environment that protects the tumor cells. Additionally, endothelial cells (ECs) promote angiogenesis to supply nutrients and oxygen[19]. Fibroblasts, another cellular component of the PMN, provide biomechanical support and play a key role in immunosuppression[20].

The primary tumor can release molecular components into the bloodstream, including EVs, cytokines, chemokines, and growth factors. Their release helps to form a supportive microenvironment by altering the ECM, modulating immune responses to create an immunosuppressive milieu, and ensuring an adequate nutrient supply[19]. Once the PMN is established, it provides a supportive niche for the incoming tumor cells, facilitating their survival, proliferation, and adaption[21]. The transition from PMN to the metastatic niche begins after circulating tumor cells (CTCs) arrive in this pre-established TME, where the primary goal of the initial micro-metastasis is to ensure self-survival and establish stable growth and invasion[22]. This intricate interplay between tumor-derived factors and the microenvironment underscores the complexity of the metastatic cascade, revealing potential therapeutic targets for mitigating metastasis.

1.4   The Metastatic Cascade

The identification and characterization of metastatic niches are crucial for both the prevention and treatment of metastatic cancer. Colonization of a distant organ is widely recognized as the most rate-limiting step in the metastatic cascade[23]. The metastatic cascade is the process where aggressive cancer cells travel from the primary tumor through the blood vessels or the

lymphatic channels and reach distant organs. Here, the cancer cells have the ability to develop one or several metastases[24]. The cascade is typically divided into local invasion, intravasation into circulatory systems, transport, extravasation of CTCs, and subsequent survival, proliferation, and metastatic colonization[25]. A tumor is more complex than merely an isolated mass of cancer cells, as it also involves tissue that recruits and receives signals from neighboring normal cells, namely the TME. This interaction between the tumor and the surroundings affects the metastatic ability, meaning that not all cancer cells have the ability to metastasize[9].

Malignant cells must effectively detach from their parent tissues to successfully invade surrounding tissues. This means that they must breach the basement membrane that surrounds and supports epithelial tissues (**Fig. 1.4**). Enzymes known as matrix metalloproteinases (MMPs) play a key role in degradation of collagen in the breakage of the basement membrane. These enzymes degrade the ECM, allowing cancer cells to penetrate and move into the surrounding stroma[26,27]. Cell adhesion molecules (CAMs) are cell surface proteins that are involved in cell-to-cell and cell-to-ECM anchoring by maintaining cell signaling and tissue structure[28]. Cadherins are a type of CAMs that are calcium-dependent and interact with the cytoskeleton via catenins. Catenins can bind transcription factors and induce gene expression in the nucleus. Integrins are a family of cell adhesion receptors made up of α and β subunits that mediate interactions between cells and the ECM. They play a critical role in cell migration, proliferation and survival as they are involved in cell adhesion to the ECM[9]. Tumor-secreted factors include vascular endothelial growth factor (VEGF), cytokines, (e.g. interleukins and tumor necrosis factor (TNF)), chemokines and EVs which help promoting growth, angiogenesis, immune evasion, and metastasis[29].

Epithelial-mesenchymal-transition (EMT) is a fundamental biological process characterized by the transformation of closely connected epithelial cells into highly mobile mesenchymal cells. This mesenchymal cell phenotype is characterized by enhanced migratory capacity, increased invasiveness, elevated resistance to apoptosis, and increased production of ECM components. Activation of transcription factors (i.e. Slug, Snail, and Twist) through growth factors released from the tumor stroma, expression of cell-surface proteins, cytoskeletal reorganization, and production of ECM-degrading enzymes are examples of molecular processes involved in the initiation and completion of EMT[30]. Another hallmark of the EMT is the "cadherin-switch", involving the downregulation of epithelial markers like E-cadherin

and upregulation of mesenchymal proteins, including N-cadherin. Additionally, there is increased secretion of MMPs. These changes promote a shift from tight cell-to-cell and cell-basement membrane connections and contribute to the aggressive tumor phenotype with the capability to escape from the primary tumor[9,31].

Upon successful breaching the basement membrane, cancer cells have the potential to intravasate into either lymphatic vessels or the blood vasculature. Once within the vessels, their survival depends on anchorage to solid substrates. Without which, migrating cells may undergo aniokis, a rapid apoptosis triggered by detachment from a solid substrate like the ECM[27]. CTCs travel alone or anchored to active platelets, called emboli, which protect tumor cells from sheer forces inside the blood stream[9,32]. The larger size of cancer cells, exceeding 20 μm, poses transportation challenges compared to smaller and more flexible red blood cells, which are around 7 μm in size. Additionally, when anchored to platelets, cancer cells become even larger, making them susceptible to entrapment in larger vessels such as arterioles[27].

For cancer cells to exit a blood or lymphatic vessel (extravasation), they must adhere to the endothelial surface, traverse through ECs and the basement membrane, and infiltrate the surrounding stroma. The attachment of cancer cells to the endothelium is facilitated by E-selectin expressed on ECs. This interaction with E-selectin also initiates a signal transduction cascade helping the cancer cells to pass through the ECs[9].

After entering the parenchyma of a new tissue, metastatic cancer cells will start to build a PMN and eventually give rise to micrometastases. Some of these have the potential to grow into detectable, macroscopic metastases[27]. The successful establishment of secondary tumors in distant organs requires a balance between the cancer cells, the requirements of the PMN, and the activation of anabolic pathways that support rapid growth and the creation of larger metastatic lesions[33]. The colonization step is also defined as the most rate-limiting step of metastasis[9]. Considering the described factors of the metastatic cascade, it is a highly complex and inefficient process with less than 0,01% of invasive cells producing metastasis in the end[34].
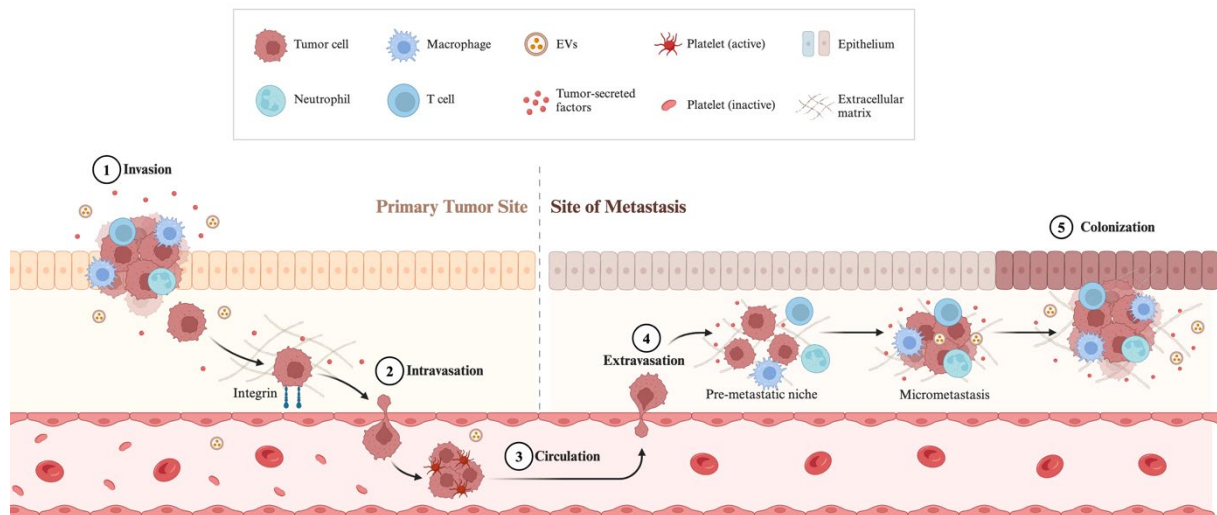
Figure 1.4 – The metastatic cascade*: A multistep process involving several stages. 1) Local invasion: tumor cells migrate into nearby tissues by breaching the basement membrane and invading the ECM. 2) Intravasation: cancer cells along enter the bloodstream or the lymphatics, where they 3) circulate either as single cells or together with platelets, surviving shear stress and evading immune surveillance. 4) Extravasation: upon reaching distant organs, tumor cells attach to ECs and extravasate into the tissue. 5) PMN: establishment of micrometastases. In this stage they may remain dormant for years before proliferating into macrometastases in 5) colonization. Tumor-secreted factors including EVs and cytokines contribute to the formation of a PMN and support the survival of the DTCs. Adapted from the template "Overview of the Metastatic Cascade", by BioRender.com (2024) with inspiration from [35].*

1.5   Brain Metastases (BM)

BM, or secondary brain tumors, occur when metastatic cells successfully enter the brain, proliferate, and cause local invasion, displacement, and inflammation. It is a common complication of cancer, occurring in 10-26% of patients who die from their cancer, and accounts for 15-25% of intracranial tumors in adults. In 1 of 3 cases, the primary tumor remains unidentified at the time of neurosurgical intervention. BM are linked to poor survival outcomes and present several clinical challenges[36,37]. Although a cure is rare when cancer has spread to the brain, long-term survival and palliation with minimal adverse effects are possible[36,38]. BM represent the most prevalent variant of intracranial tumor[39] and the estimated overall survival (OS) is six months [40]. This underscores the importance of early tumor detection, preferably before cancer cells breach the blood-brain barrier (BBB) and form metastases. On the other hand, newer technology like advanced imaging techniques and modern treatment are allowing patients suffering from BM to live longer even though the

cancer itself cannot be cured[41]. In situations where a cure is not possible, palliative care and emotional and physiological support play a crucial role[42].

Certain types of cancer are more prone to spread to the brain. The most common include lung cancer, breast cancer, melanoma, colorectal, and renal cancer[43]. Symptoms can vary depending on the site of metastasis, as different parts of the brain serve different functions. Patients may experience symptoms including headache, seizures, neurological deficits, fatigue, nausea and vomiting, and cognitive impairment. The majority of these symptoms are related directly to brain compression from the tumor or the edema[42].

1.5.1   Diagnosis of BM

The diagnosis of BM mainly involves a neurological examination, imaging studies, and biopsy sampling and testing[44]. The neurological examination commonly includes checks for vision, hearing assessment, speech evaluation, balance testing, assessment of strength, coordination examination, and memory assessment[45]. A comprehensive description of symptoms, including their duration and intensity, should be provided, with a focus on questions based on headaches, blurry vision, and nausea. Computerized tomography (CT) provides a quick examination, but MRI is preferred for a more comprehensive assessment, since this methodology provides much better anatomical information than CT. Thus, MRI is the gold standard when diagnosing BM. T1-weighted MRI with and without gadolinium contrast agent, and T2-weighted fluid attenuated inversion recovery (FLAIR) sequences, are the preferred imaging methods for determination of size, morphology, and macroscopic structures of BM. New technology enhances the visibility of metastases, with advanced MRI techniques such as diffusion- and perfusion-weighted MRI, and spectroscopy may be capable of extending beyond anatomical imaging to characterize microstructures, cellularity, physiology, perfusion, and metabolism[46]. Further, CT combined with positron emission tomography (PET) is also commonly used to provide information about for instance metabolic activity, detection of tumor recurrence and assessment of treatment responses. Blood samples should be followed up by analyzing complete blood count, metabolic panel, and liver function[45].

1.5.2 Treatment of BM

BM are commonly treated using a combination of surgery, radiation therapy (whole-brain radiotherapy (WBRT) and/or stereotactic radiosurgery (SRS)), chemotherapy, immunotherapy, and targeted therapy. The determination of treatment is based on the number of lesions, tumor size, and location of the BM, as well as the patient's health and condition and the primary tumor[47]. The first step typically involves treatment of intracranial edema by receiving orally or intravenous steroids, for example dexamethasone. Antiepileptic drugs can help treating seizures, and anticoagulation medications can help prevent possible blood clot formation in the brain. Surgical resection may be relevant for patients with surgically accessible and limited lesions and good performance status. WBRT is a treatment option often given to patients with multiple lesions and poor performance status, where the whole brain is receiving daily radiotherapy treatments. SRS is a more specific way of treating a distinct lesion to one specific area of the brain, but with high doses of radiation. Radiation therapy has in general the potential to reduce tumor size and also stop tumor growth [45,47]. Therefore, frequent MRI scans for patient follow-up are crucial for detecting tumor regrowth.

Only small lipid-soluble molecules can pass through the BBB, posing a challenge for the penetration of an intact brain vasculature by chemotherapeutic agents. However, certain chemotherapeutic agents, designed to penetrate the BBB may be used in combination with surgery or radiation therapy. The decision to use chemotherapy upfront for BM should depend on how well the primary tumor responds to the chosen chemotherapy, rather than solely on whether the drug can pass through the BBB[48].

Initially, there was skepticism about the efficacy of immunotherapy for patients with brain tumors and metastases due to concerns about these agents crossing an intact BBB and the limited immune response in the brain. Yet, recent studies have indicated that immunotherapy alone or in combination with other treatment options, has been showing promising results in decreasing the spread of BM and reducing tumor size[49,50]. Immunotherapy has also demonstrated promising results in the OS. The principle behind this type of treatment is that it uses components of the immune system made by the body itself or developed in a laboratory to give the immune system a boost, helping it to recognize and kill foreign cancer cells. Immune checkpoint inhibitors, adoptive cellular immunotherapy, treatment vaccines, and oncolytic virus therapy are the four main forms of immunotherapy being studied in patients

suffering from BM. Anti-programmed death-ligand 1/anti-programmed cell death protein 1 (anti-PD-L1/anti-PD-1) and anti-cytotoxic T-lymphocyte-associated protein 4 (anti-CTLA-4) are examples of immunotherapy drugs targeting specific proteins (PD-L1, PD-1 and CTLA-4) to enhance the immune system´s ability to recognize and attach cancer cells. These drugs have shown success in lung cancer and melanoma but may cause immune-related side effects[50].

Collaborations between physicians, neurosurgeons, pathologists, radiologists, and oncologists are important to achieve an effective treatment of BM[51]. Additionally, combined therapies enhance clinical efficacy in advanced cancer patients, with each individual case requiring careful consideration.

1.5.3   Causes and Risk Factors of BM

While different primary cancers can metastasize to the brain, certain types carry a greater risk of developing BM. The chance of an extracranial tumor generating metastases in the brain depends on the cancer cells´ capacity from the primary tumor to adapt to the brain microenvironment, as demonstrated by Stephen Paget in his "seed and soil" hypothesis[27]. Additionally, variations in occurrence of BM are present across different racial, gender, and age groups in terms of incidence proportions[52]. **Fig. 1.5.3** illustrates most common primary tumors and their incidence proportions of causing BM.
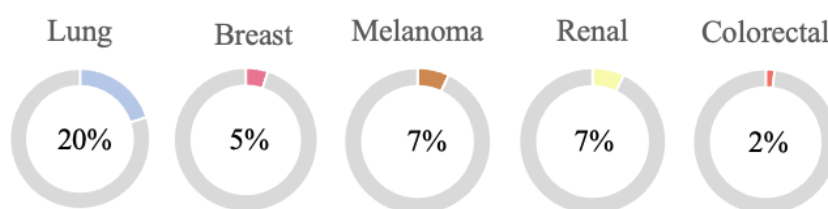
Figure 1.5.3 - Prevalence rates of BM associated with various common primary tumors: The values are taken from Davis et al. [52]

Breast cancer (BC) carries a risk of developing BM, especially triple negative breast cancer (TNBC), characterized by the absence of three specific receptors: estrogen receptors (ERe), progesterone receptors (PR), and human epidermal growth factor receptor 2 (HER2)[53]. Additionally, overexpression of HER2 presents a higher chance of BM. These subtypes may exhibit more aggressive behavior and can easily spread to distant organs like the brain.

Advanced stages of BC, such as stage IV, indicate that the cancer has already spread to distal organs, increasing the risk of BM. Young age at the time of BC diagnosis also poses a risk factor for metastasis to the brain. Larger tumor size and higher tumor grade are associated with an increased risk of metastasis, as well as whether the cancer has spread to the lymph nodes or not[54].

Epidermal growth factor receptor (EGFR) is a transmembrane tyrosine kinase receptor often overexpressed in certain types of lung cancer. As much as 70% of EGFR-mutant non-small cell lung cancer (NSCLC) patients develop BM. EGFR mutations are more prevalent in specific populations, such as Asian non-smokers and patients with adenocarcinoma histology[55]. Mutations in v-Raf murine sarcoma viral oncogene homolog B (BRAF), particularly the V600E mutation, are typically found in melanomas metastasizing to the brain. The BRAF gene encodes a protein involved in the mitogen activated protein kinase pathway/extracellular signal-regulated kinase (MAPK/ERK), regulating cell growth and proliferation. The V600E mutation leads to constitutive activation of the BRAF protein and continuous stimulation of the pathway[56]. Kirsten rat sarcoma viral oncogene homolog (KRAS) mutations are present in approximately 35-45% of colorectal cancers[57]. These mutations can lead to continuous activation of the MAPK/ERK signaling pathway, promoting uncontrolled cell growth[58].

1.6   Lung Cancer BM

Lung cancer is one of the most common cancers that can metastasize to the brain, and the development of BM is a significant complication in the management of lung cancer. NSCLC is the most common primary cancer to develop metastases in the brain. 30-43% of patients with NSCLC develop BM with no other proven metastases to other organs. MRI of the brain is recommended for patients that have been newly diagnosed with lung cancer, as it may not necessarily present metastatic symptoms[36,59]. Also, females are more prone to develop BM from lung cancer than men[36,52]. In small cell lung cancer (SCLC), BM were observed in more than 20% of the patients. One treatment option is the use of prophylactic cranial irradiation to prevent metastases to the brain and prolonging disease-free and survival in SCLC[36]. Patients with lung cancer BM have a poor prognosis, but frequent use of early imaging techniques facilitates diagnosis at an earlier stage. Thus, the median patient survival has increased to around 12 months[59]. In addition, the combination of different treatment options like WBRT

and SRS may improve OS in patients with favorable prognostic outcomes, compared to only using WBRT[60]. The systemic treatment of NSCLC has been improved over the last decade by introduction of targeted therapies such as tyrosine kinase inhibitors and immunotherapy, including drugs like bevacizumab[59].

1.7 Melanoma BM

It is estimated that approximately 10-40% of patients with advanced melanoma will develop BM during the course of their disease, which is associated with high morbidity and mortality[61,62]. The majority of patients with MBM will develop multiple brain lesions[63]. The median OS of melanoma patients with BM ranges between 2 and 8 months. The standard treatments of MBM includes surgery, radiosurgery, WBRT, and chemotherapy, often used in combination[61]. Unfortunately, these treatments have not shown improvement in the OS. New treatments like targeted therapies and immunotherapy, such as BRAF inhibitors, have shown improved outcomes[64]. A CT scan is recommended, and MRI must be used to investigate more precisely the characteristics of the lesions[65].

1.8 Physiology and Microenvironment of the Brain

The brain includes cellular, molecular, and structural components that maintain normal brain function[66]. Neurons and glial cells are the two main cell types.

A mature brain consists of more than 100 billion specialized cells called neurons, which are the primary computing element and transmits information via electrical pulses through an axon that connects with other neurons. At synapses, information is transmitted through the release of neurotransmitters from boutons at the axon terminals. These molecules diffuse to receptor molecules on the receiving neuron, converting the chemical code into an electrical signal for transmission along the next axon[66,67]. The precise balance of neurotransmitters in the brain microenvironment is essential for proper neuronal function.

Glial cells, comprised of astrocytes, oligodendrocytes, and microglia, are essential components of the brain microenvironment and have a supportive, protective, and regulatory role. Astrocytes occupy 25% of the total brain volume and are divided into protoplasmic and fibrous astrocytes. They provide structural support, regulate the extracellular microenvironment, and contribute to the integrity of the BBB. Oligodendrocytes produce

myelin, a proteolipid which maintains electrical impulse conduction and maximizes velocity. If the myelin sheath is damaged, nerve signals will be sent more slowly or can be blocked. Microglia are phagocytic cells and represents the brain´s immune system[66,67]. They serve as brain macrophages but differ from other macrophages as they have their own unique homeostatic phenotype and tight regulation by the brain microenvironment. Some of their tasks are elimination of microbes, dead cells, protein aggregates, and other agents that could pose a threat to the central nervous system (CNS)[68].

Cerebrospinal fluid (CSF) helps maintain a stable microenvironment by surrounding the brain and spinal cord, providing mechanical support, supplying and exchanging nutrients, and removing waste products[69].

1.8.1   The Blood-Brain Barrier (BBB)

The BBB, first described by Paul Ehlrich in 1885, is a highly selective semipermeable membrane between the blood vessels and the brain. It consists of ECs forming the capillary walls in the brain. Tight junctions (TJs) connect these ECs, with pericytes (PCs), astrocyte end-feet, and the basal lamina surrounding them (**Fig. 1.8.1**). Together, these components play a crucial role in creating the highly selective nature of the BBB. This selectivity limits the passage of ions, molecules, and cells from the blood to the brain more effectively than any other capillaries in the body[70,71]. As the CNS has special structures and requires a steady environment different from the rest of the body, a balanced brain microenvironment is needed so that the CNS can work without interference[72].
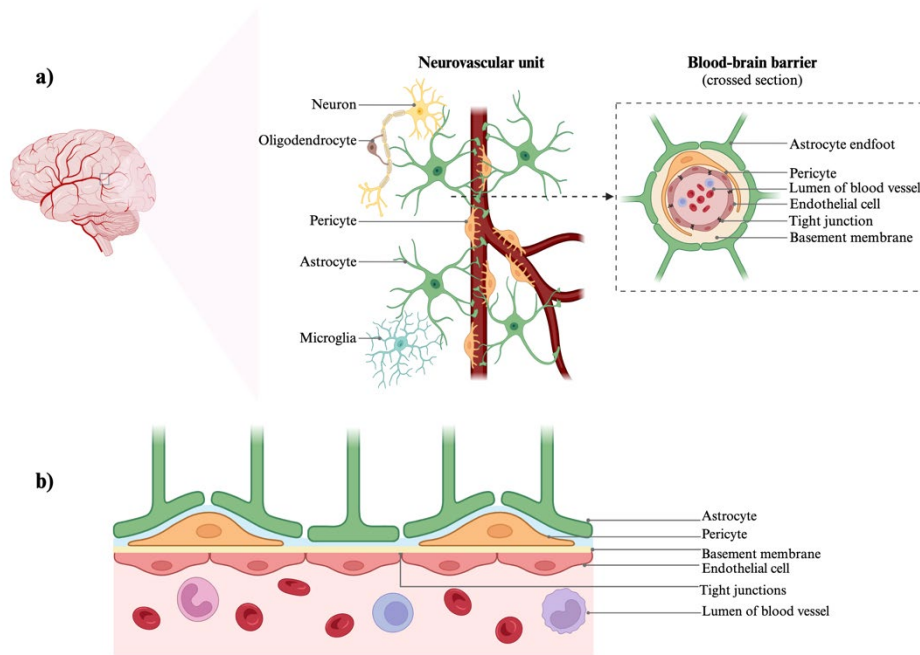
Figure 1.8.1 – The neurovascular unit and the BBB: a) The neurovascular unit consists of neurons, glial cells, ECs, and PCs within the CNS, along with a cross section of the BBB with its cellular components and their arrangement. b) Structure of the BBB showing astrocyte end-feet surrounding the vessels, PCs, the basement membrane, and TJs between ECs. The figure was created with BioRender.com with inspiration from [73].

The ECM is a non-cellular, three-dimensional network of proteins and other molecules that provide structural support, guides neuronal migration, and influence cellular behavior. Comprising collagen, fibronectin, laminin, elastin, and other glycoproteins, the ECM forms a scaffold supporting brain tissue architecture. It plays a crucial role in synaptic plasticity, regulates the BBB, and contributes to tissue repair after injury. The ECM´s influence on cell signaling affects processes such as cell survival, proliferation, and differentiation[74].

1.9   The Tumor Microenvironment (TME)

Besides cancer cells, a tumor contains a variety of other components that influence the cancer progression, including stromal cells like ECs, PCs, fibroblasts, immune cells, and non-cellular components (**Fig. 1.9**). These various components and cell types engage in crosstalk, triggering cell activation and differentiation, and inducing alterations and biological properties of the ECM that facilitate tumor proliferation and invasion[75-77]. When the metastasizing cancer cells arrive to a distant organ, they encounter a foreign microenvironment that is different from the niche of the primary tumor. Therefore, cancer cells can manipulate and hijack normal cell function to help them expand and establish. For

example, ECs constitute blood vessels which provides nutrition and oxygen to the tumor and promote metastasis by allowing cancer cells to translocate into the blood vessel lumen. In addition, ECs are one of the main sources of cancer-associated fibroblasts (CAFs), which are highly heterogenous cells that play a key role in the migration and invasion abilities of cancer cells. Thus, the endothelium indirectly contributes to the process of metastasis[78].

Hypoxia is an important feature of the TME due to a combination of factors associated with rapid tumor growth and inadequate blood supply. Tumor hypoxia can activate angiogenesis, thereby enhancing aggressiveness, increasing risk of metastasis and developing resistance to radio- or chemotherapy[79,80]. By targeting pro-angiogenic factors and their receptors, including VEGF, VEGF receptor-1,-2, basic fibroblasts growth factor (bFGF), platelet derived growth factor B (PDGF), insulin-like growth factor II (IFG2) and epidermal growth factor (EGF), hypoxia regulates the production of new blood vessels through hypoxia-inducible factor (HIF) transcription factors[80].

Immune cells are another type of stromal cells found in the TME, which can either possess tumor-antagonizing or tumor-promoting functions. While immune cells within the TME initially target and eliminate cancer cells in the early stages of tumorigenesis, cancer cells eventually evade immune surveillance and hinder the cytotoxic functions of these immune cells[81]. Tumor infiltrating lymphocytes (TILs), including CD4+ and CD8+ T cells, play a key role in the anti-tumor response. Tumor-associated macrophages (TAMs), dendritic cells (DCs), natural killer (NK) cells, myeloid-derived suppressor cells (MDSCs), regulatory T cells (Tregs), and B cells contribute to the intricate interplay within the TME[82]. Immune cells can secrete signaling molecules such as cytokines and chemokines in an inflammatory microenvironment, which contributes to increased cancer cell survival, phenotypic plasticity, and adaptation to the surrounding environment[83].

Figure 1.9 – Main components of the TME: *The TME consists of both cellular and non-cellular components. Cellular elements include cancer cells, ECs, PCs, CAFs, and various immune cells e.g., T cells, NK-cells, TAMs, and DCs. The ECM represents the non-cellular components, serving as a scaffold. Interactions within the TME occur through cell-cell contacts, interactions with the ECM, and the release of cytokines, chemokines, and EVs. Created with BioRender.com with inspiration from [84].*

1.10 Extracellular Vesicles (EVs)

EVs are small, lipid bound vesicles released by cells into the extracellular environment. In general, EVs are released by all forms of living cells and can be found in almost all body fluids, including CSF, peripheral blood, ascites, breast milk, and urine. A single cell can release multiple types of EVs, and there can be differences within each type of EVs released by the same cell[85]. EVs are classified into three main types: exosomes, microvesicles, and apoptotic bodies[86]. These small membrane vesicles were initially regarded as waste from cells and "platelet dust" lacking biological significance[87]; however, there is increasing evidence for their crucial role in the regulation of normal physiological processes and contributing to the pathology of various diseases[88]. It has been shown that EVs can serve as drug delivery platforms in cancer therapy, offering unique advantages due to their biocompatibility and immune compatibility. As engineered EVs evolve, they are increasingly applied in combination therapy to target heterogenous cancer cells and the complex TME[89].

Exosomes are the smallest type of EVs, typically ranging in size from 30-150 nm. They play an important role in EV-mediated cell-to-cell interactions, both locally and systemically, by transferring proteins, lipids, nucleic acids, and other bioactive molecules from their parental

cells to others and alter their phenotypes. Exosomes released by a specific parent cell, including those from diseases cells, possess the capacity to influence the activities of neighboring cells, the microenvironment surrounding the parent cell, and the characteristics of distant cells and tissues[90]. Given their ability to transport bioactive molecules and traverse biological barriers, EVs are increasingly explored for their potential as therapeutic agents[91]. Under a scanning electron microscope, exosomes appear as small, round, or cup-shaped vesicles. The membrane of exosomes can be visualized as a lipid bilayer surrounding the internal cargo[92].

Microvesicles, (or shedding vesicles) are larger than exosomes, with diameters ranging from 100 nm to 1 μm. They are released from cells into the extracellular area by outward budding of the plasma membrane. Microvesicles carry a variety of molecules, including proteins and nucleic acids[93]. Apoptotic bodies are larger EVs, reported to range in size from 50 nm up to 5 μm, and are generated by blebbing of the plasma membrane during programmed cell death, apoptosis. Apoptotic bodies contain cellular remnants from a dying cell, including fragmented DNA and organelles[86,94].

1.10.1   Composition and Biological Relevance of EVs

The cargo of EVs consists of lipids (e.g., cholesterol, sphingolipids, and ceramide), metabolites (e.g., amino acids and sugars), proteins (e.g., tetraspanins, heat shock proteins), and nucleic acids, including DNA and RNA[95-97] (**Fig. 1.10.2**). The vesicles contain various types of RNA including microRNA (miRNA), messenger RNA (mRNA), ribosomal RNA (rRNA), and non-coding RNAs (ncRNAs)[95,98]. The specific composition of EVs can vary depending on the cell of origin, physiological state, and cargo sorting mechanisms. CD63, CD81, and CD9 are examples of tetraspanins commonly found in EVs. Different components are present in some subtypes of EVs and not in others. For example, histones, proteasomes, and ribosome components are secreted in bigger plasma membrane-derived EVs and/or apoptotic bodies rather than exosomes. Flotillin-1 (FLOT1) and annexin are two common fusion and transfer proteins found in EVs. Other components are enzymes, cytoskeletal proteins, growth factors, cytokines, signaling molecules, and major histological compatibility complex (MHC) class I/II[99,100].

Beyond their role as intercellular messengers, EVs can influence immune responses by transporting immunomodulatory molecules and antigens. They can either stimulate or suppress the immune system, contributing to the development of inflammatory, autoimmune, and infectious diseases[101]. EVs derived from antigen-presenting cells (APCs) can carry MHC molecules and antigens. Subsequently, other immune cells can internalize these EVs, aiding in the presentation of antigens to T cells and facilitating immune recognition and response[102]. They also play a role in tissue homeostasis and provide tissue repair and regeneration[103]. In the context of cancer, tumor-derived EVs can influence immune responses. They may carry tumor antigens, promoting antitumor immunity, or they can contribute to immune evasion by suppressing immune cell activities[104]. Nevertheless, EVs are actively investigated as drug delivery carriers because of their high bioavailability, biostability, small size, endogenous origin, and low toxicity[105,106]. After being taken up, they can induce intercellular signaling and molecular alterations that may influence the recipients physiological or pathological conditions[107].

1.10.2   Biogenesis and Release of EVs

Exosomes are formed as intraluminal vesicles (ILVs) within multivesicular bodies (MVBs). This process involves different pathways, including the endosomal sorting complex required for transport (ESCRT)-dependent and ESCRT-independent mechanisms facilitated by proteins like syntenin, lipids, and tetraspanins. Upon ILV formation, MVBs are transported to the plasma membrane or lysosome, aided by Rab proteins. Fusion of MVBs with the plasma membrane, mediated by the soluble N-ethylmaleimide-sensitive factor attachment protein receptor (SNARE) complex, leads to exosome release. Microvesicles are directly released via outward budding from the plasma membrane, involving ESCRT, arrestin domain-containing protein 1 (ARRDC1), lipids, Rho proteins, and Ca^{2+}. Apoptotic bodies are products of apoptotic cells and are shed from the cell surface[105] (**Fig. 1.10.2**).

EVs can travel through the interstitial space, where they may adhere to the ECM or diffuse to reach other target cells, as well as enter blood or lymphatic capillaries[108]. EVs are taken up by various endocytic pathways, including clathrin-dependent endocytosis, as well as clathrin-independent routes like caveolin-mediated uptake, micropinocytosis, phagocytosis, and lipid raft-mediated internalization. A heterogenous population of EVs may use different pathways for cellular entry, and the specific mechanism may be influenced by surface proteins and

glycoproteins on both the vesicle and the target cell. Uptake can occur very quickly, with EVs detected inside cells as early as 15 minutes after their initial introduction[109]. EVs of varying sizes appear to have different targeting and uptake rates. Small EVs (sEVs) (<100 nm) are taken up by recipient cells more rapidly than larger EVs, facilitating efficient delivery of their cargo and signals. Due to their small size, exosomes can specifically target tumor tissue through enhanced permeability and retention[110].
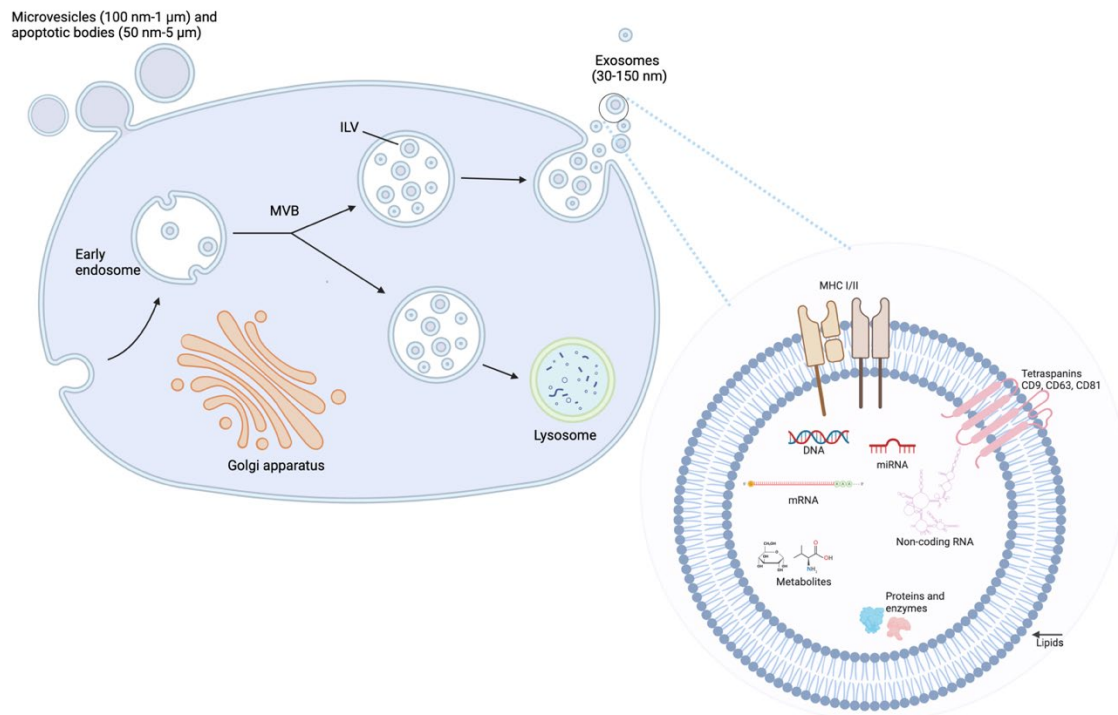
Figure 1.10.2 – The release and composition of EVs (exosomes, microvesicles, and apoptotic bodies). *Exosomes originate from endosomes and are the smallest of the EVs. Microvesicles are larger and are formed by budding or exocytosis of the plasma membrane. Apoptotic bodies are the largest, resulting from membrane blebbing during apoptosis. The content includes lipids, DNA, both coding and ncRNAs, soluble and membrane-associated proteins, metabolites, nucleic acids, and small molecules. The lipid bilayer membrane consists of phospholipids and cholesterol derivates. The composition between exosomes and microvesicles have some variations due to their different biogenesis. The figure was created in BioRender.com inspired by [111,112].*

1.10.3 Function of EVs in the TME and Cancer Progression

Cancer cells are known for releasing a higher quantity of EVs compared to their nonmalignant counterparts[113]. The cargo of cancer-derived EVs is associated with promoting cell growth, metastasis, angiogenesis, therapy resistance, and immune evasion[114]. Within tumors, EVs contribute to the formation of a supportive TME and PMN as they play a key role in the

communication between tumor cells and stromal cells both within local and distant microenvironments. EVs serve as critical mediators that establish communication channels among malignant, endothelial, stromal and immune cells within the TME[106].

In BM, EV cargo has been observed to breach the BBB and modify the vascular environment, facilitating the formation of a secondary tumor[92,115]. The interaction between cancer cells, via the exchange of EVs, can facilitate the transfer of oncogenes and miRNA (onco-miRNAs/oncomirs) from one cell to another. This process may result in the reprogramming of the recipient cell, enhancing pro-metastatic behavior[92]. MiRNAs regulate about 30% of human genes and a majority of these are identified as tumor-associated[116]. At the University of Bergen, Rigg and colleagues have shown that EVs derived from MBM significantly contribute to the progression of BM by increased levels of miR-146a-5p, and that its knock-down inhibits MBM progression[117]. A deeper understanding of the role of EVs in BM is crucial for advancing cancer research. The Brain Metastasis Research Group at the University of Bergen is actively focusing on this area to reveal the complexities of BM and identifying potential therapeutic strategies.

1.11 Magnetic Resonance Imaging (MRI)

MRI is a non-invasive medical imaging technique used to produce detailed images of the internal structures of the body. It uses a strong magnetic field and radio waves to generate images of organs, tissues, and other structures with high clarity and resolution[118]. MRI is particularly useful for examining soft tissues including the brain, spinal cord, muscles, and organs like the heart and liver[119]. The MR machine is comprised of a primary magnet, three gradient coils, shim coils, and an integrated radiofrequency (RF) coil. The strength of the magnetic field is measured in Tesla (T), and the clinical MRI is usually performed at 1,5-3T[120].

MRI uses the body´s natural magnetic properties to generated detailed images from the body, focusing on the hydrogen nucleus as it contains one single proton, making it a net positive charge. The single proton is used in imaging purposes because of its abundance in water and fat[121]. Normally, the protons are randomly distributed in all directions. However, within the magnetic field of the MRI scanner, hydrogen protons align uniformly like tiny bar magnets due to their positive and negative pole, forming a magnetic vector along the scanner´s axis.

Varying radio wave frequencies cause hydrogen nuclei to resonate based on the magnetic field strength. The primary magnet produces a static magnetic field called B_0, and the gradient coils modify the magnetic field strength locally, allowing different body slices to resonate at various frequencies. Positioned within the primary magnet´s bore, the x, y, z coils correspond to their respective axes. The z coil produces axial images, the y coil produces coronal images, and the x coil generates sagittal images. RF coils capture the emitted radio wave signal when the magnetic vector returns to its relaxation state, translating it into grayscale images[120,121].

RF pulses highlight specific tissues or abnormalities based on differences in tissue relaxation rates. Proton relaxation time is measured in two ways: T1 (longitudinal relaxation time), which measures the time for the magnetic vector to return to its resting state, with 63% of longitudinal magnetization recovered, and T2 (transverse relaxation time), which is the time for axial spin to return to its resting state, measuring the time required before transverse magnetism is decreased to 37%[121]. The repetition time (TR) refers to the duration between RF pulses, while the echo time (TE) is the time between the RF pulse and the signal recording. T1w images, with a short TR/short TE offer the clearest anatomical detail, while T2w images, with a long TR/long TE, are often necessary to reveal pathology. The net magnetization can be decomposed into longitudinal (M_z) and transverse (M_{xy}) components relative to the B_0[122]. **Fig. 1.11** illustrates the basic principle of MRI. T2* relaxation involves the decay of transverse magnetization due to both spin-spin relaxation and magnetic field inhomogeneity. T2*-weighted images are sensitive to susceptibility effects and are often used to detect hemorrhage, calcification, and iron deposition in tissues[123].
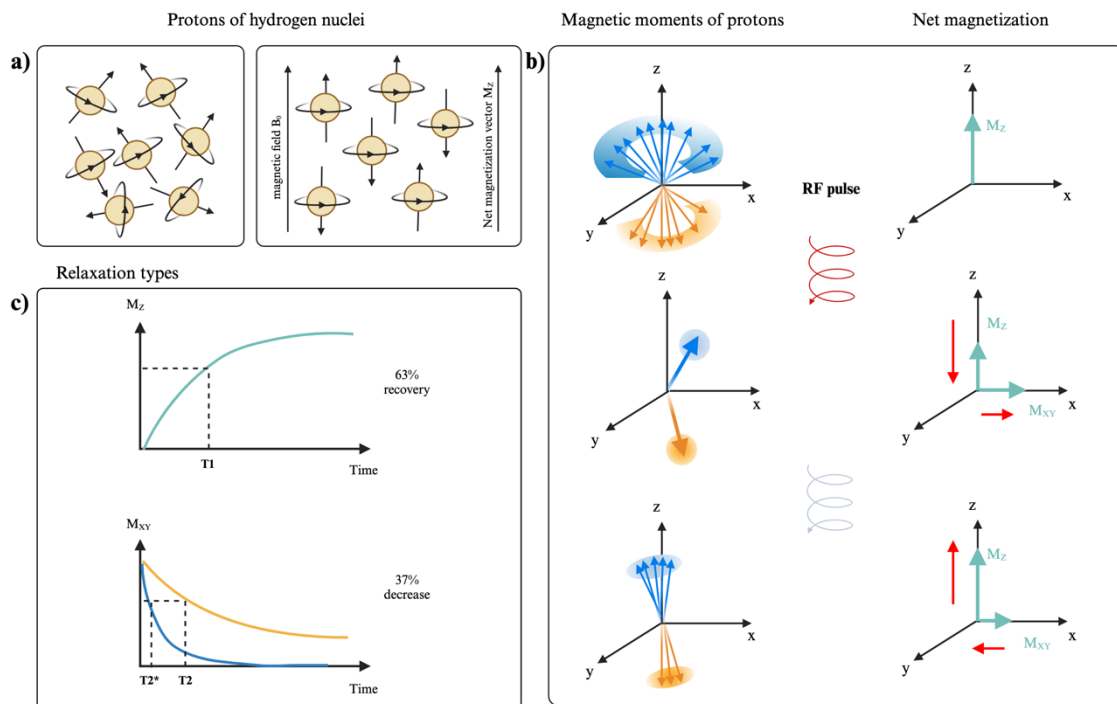
Figure 1.11 – Basic principle of MRI: *a) Hydrogen protons spin with their axes randomly aligned under normal circumstances, whereas in a magnetic field, the protons´ axes all line up either parallel or anti-parallel to the magnetic field. b) Upon an RF pulse, there is a reduction in longitudinal magnetization (M_z) and generation of transverse magnetization (M_{xy}). After a certain time, the nuclear spins return to their relaxation state. c) Different relaxation types: T1 describes the time it takes for the restoration of M_z back towards its initial maximum level, T2 describes the time it takes for the MR signal to decay in the transverse plane, and T2* describes the time it takes for the decay of the MR signal due to both spin-spin relaxations and magnetic field inhomogeneities. Adapted from the template "Basic mechanism of the MRI signal", by BioRender.com (2024)*

1.11.1 Labeling Cells and EVs With Superparamagnetic Iron Oxide Nanoparticles (SPIONs) for MRI

MRI is the best method for visualization of brain pathologies due to its high spatial resolution and tissue contrast. However, it falls short in detecting micrometastases or tracking single tumor cells within the brain. Consequently, the high magnetic signal properties of superparamagnetic iron oxide nanoparticles (SPIONs) make them increasingly used as contrast agents for visualizing cells through MRI, facilitating the detection of labeled objects[124,125]. SPIONs are mostly used for their ability to produce negative enhancement effects on T2- an T2*-weighted sequences. However, their impact on T1 relaxation time can also be advantageous if the appropriate imaging sequences are selected[126]. There are findings indicating that SPION-labeling empowers *in vivo* tracking of single cancer cells within the

brain[127]. In the context of early cancer detection or treatment monitoring, this is an important technique.

SPIONs are attractive probes for EV labeling due to their small size and biocompatibility and can be used to track the biodistribution and fate of EVs *in vivo* using MRI. This enables non-invasive monitoring and tracking of EV delivery to target tissues or organs. Some techniques used for labeling EVs are electroporation, natural incubation, and cell extrusion. The targeting and delivery of therapeutic agents to specific cells or tissues can be enhanced by loading SPIONs into EVs, as the SPION-loaded EVs can be guided to the target site using the magnetic fields[124]. False positives, low sensitivity, and lack of accurate quantification are drawbacks associated with the use of SPIONs[128]. Nonetheless, integrating SPIONs into EVs offers promising opportunities for cancer diagnosis, treatment, and disease monitoring. Despite the potential, there is still much to learn about the interactions between EVs and SPIONs.

2.   Aims

The objective of this study was to label EVs derived from melanoma and lung BM with iron nanoparticles, with the aim of establishing a model for future tracking the EVs *in vitro* and *in vivo*, investigating their role in the metastatic process, and the cell types they target. This thesis seeks to enhance our understanding of disease microenvironments for improved detection and treatment strategies. Several sub-aims were carried out to achieve this:

1: Characterize EVs from BM cell lines using two different isolation methods, comparing and evaluating the two methods based on a comprehensive assessment and the final EV yield.

2: Label EVs with SPIONs and compare two different labeling methods using two different SPIONs with variations in size and coating.

3: To create phantoms of iron-labeled cells and EVs to simulate and validate imaging through MRI, before conducting *in vivo* experiments, which will be a part of a bigger future project.

Overall, this study aims to strengthen our understanding of EVs' role in the metastatic process in the brain, with a future goal of contributing to the development of more effective strategies for the diagnosis and treatment of BM.

3.   Materials and Methods

The methodology in the current work follows the recommendations presented in the Minimal Information for Studies of Extracellular Vesicles (MISEV2018 and MISEV2023) guidelines [30,129]. This approach ensures a standardized and rigorous reporting framework for EV research, emphasizing clarity and robustness in the experimental design and data interpretation.

3.1   Cell Lines and Cell Culture

In this study, three BM cell lines were used for the experiments. The H10 cell line was developed from a melanoma brain metastasis (MBM) of a 62-year-old female and H16 was derived from an MBM of a 65-year-old male. The LBM1 cell line was developed from a lung-brain metastasis (LBM) from a 61-year-old female patient with NSCLC. The collection of biopsies for cell culturing found place during brain tumor surgery at Haukeland University Hospital and cell lines were established in the Brain Metastasis Research Group from the collected tumor samples. Prior to the collection of tumor material, comprehensive informed written consent was obtained from each participating patient. The Regional Ethical Committee (REC) granted approval for tissue procurement, biobank storage of tumor biopsies, and the creation and utilization of cell lines (REC Approvals 2013/720 and 2020/65185). To ensure their authenticity and fidelity, the origin of these cell lines was verified through short tandem repeat (STR) fingerprinting prior to their use in the experiments. Furthermore, the cells were regularly tested for mycoplasma.

3.1.1   Cell Subculturing

The cell culture work was performed within a LAF-bench with continuous air flow. The bench and all equipment that were transferred to the bench were always sterilized with 70% ethanol prior to use, to keep the work as sterile as possible. All cell lines were grown in Dulbecco´s Modified Eagle Medium (DMEM) combined with the ingredients listed in **Table 3.1,** hereafter referred to as culture medium. Three sizes (25 cm^2, 75 cm^2 and 175 cm^2) of Nunc^{TM} EasYFlask filtered cap cell culture flasks (Thermo Fisher Scientific, Nunc, Roskilde, Denmark) were used. Newly thawed cells were cultured in a T25 flask, before transferring them to a T75 flask the next day, and thereafter into a T175 flask when the cells reached 75-80% confluency. Thus, collection of culture medium from cells for EVs extraction were done

by using T175 flasks. The cells were maintained in an incubator at 37°C with 100% humidity and 5% CO_2, hereafter referred to as standard incubator conditions.

Table 3.1: Name of reagents and the belonging producers used in cell culture handling.

REAGENT	COMPANY
DMEM-ALT	
Dulbecco´s Modified Eagle Medium	Sigma-Aldrich Inc., St. Louis, MO, USA
50 mL 10% heat-inactivated calf serum	Sigma-Aldrich
50 µg/mL Plasmocin	Invitrogen, Carlsbad, CA, USA
2% L-Glutamine	BioWhittaker, Verviers, Belgium
100 IU/mL Penicillin	BioWhittaker
100 µL/mL Streptomycin	BioWhittaker
1x Phosphate Buffer Saline (PBS)	
10x Dulbecco´s Phosphate Buffered Saline	Sigma-Aldrich
Autoclaved Milli-Q® water	Sigma-Aldrich
0,25% Trypsin-EDTA	Thermo Fisher Scientific, Nunc, Roskilde, Denmark
0,4% Trypan Blue Solution	Thermo Fisher Scientific

Cells were trypsinized at 75-80% confluency using 0,25% Trypsin-EDTA (Thermo Fisher Scientific). Before trypsinization, the flasks were rinsed with 8 mL of 1x PBS. Following this rinsing step, 3 mL of pre-warmed trypsin was added to the flasks, and they were subsequently placed in the incubator for a duration of 3-5 minutes. The cells were inspected in the microscope to confirm that they were detached before 7 mL of pre-warmed culture media was added to neutralize the trypsin. The cell culture was mixed well by pipetting up and down to prevent clumping. When splitting, 1/4-1/3 of the cell suspension was kept for further growing, while the rest was discarded. Fresh culture media was then added to the cells to a total amount of 20-30 mL in the T175 flask. To maintain phenotypic stability, genetic integrity, and the retention of specific cell features, a new vial of cells was thawed after a maximum of ten passages. Furthermore, each passage introduces a potential for contamination, which can be minimized to a greater extent by limiting cell use to ten passages at a time.

3.1.2 Cell Counting

For cell counting, a Countess^{TM} Automatic Cell Counter (Invitrogen) was used. 10 µL of cell suspension was mixed with 10 µL of 0,4% Trypan Blue Solution (Thermo Fisher Scientific). 10 µL of the well-mixed stained cell solution was then pipetted into each side of a cell counter

chamber slide (Invitrogen) before insertion into the automatic cell counter. The mean value of live cells/mL were based on the mean of two individual counts.

3.1.3   Thawing and Cryopreservation

When a new vial was taken up from the liquid nitrogen tank, a T25 flask with 5 mL prewarmed culture medium was prepared. The newly taken up vial was kept on ice until it was placed in a 37°C water bath. After a quick thawing, the cell suspension was pipetted into the flask, which then was placed in the incubator at standard incubator conditions.

When the cells were 75-80% confluent, the flask was washed with 1x PBS, trypsinized with Trypsin-EDTA and neutralized by adding culture medium as described in **Section 3.1.1**. The cell suspension was then transferred to a 15 mL Falcon tube (Sarstedt AG & Co. KG, Nümbrecht, Germany) for counting and centrifuged at 248 x g for 5 min (Jouan B4i, Thermo Fischer Scientific). The supernatant was removed, and the cell pellet was resuspended in a pre-made freezing solution. A 10 mL freezing solution consisted of 8 mL culture medium, 1 mL dimethyl sulfoxide (DMSO) (Sigma-Aldrich) and 1 mL fetal bovine serum (FBS) (Thermo Fisher Scientific). Approximately 2 000 000 cells in 1 mL of the cell suspension were pipetted into each cryotube (Nunc CryoTube^{TM} vials, Thermo Fisher Scientific). The tubes were placed in an isopropanol freezing container (Mr. Frosty^{TM} Freezing Container, Thermo Fisher Scientific) and placed in a -80°C freezer overnight. The tubes were transferred to the liquid nitrogen tank the following day.

3.2   Assessment of Uptake of SPIONs Into Cells

3.2.1   Prussian Blue Staining

H16 and LBM1 cells were seeded in 24-well dishes (Nunc^{TM}, Thermo Fisher Scientific) at a concentration of 100 000 cells per well. On the following day, once the cells had firmly adhered to the bottom of the wells, they were incubated with dextran-coated SPIONs (Molday SPIONs; BioPAL Inc., Worcester, MA, USA, catalog #CL-50Q02-6A-50, particle size 35 nm, stock solution 2 mg Fe/mL) and uncoated SPIONs (Sigma-Aldrich, catalog #725331, particle size 5 nm, stock solution 5 mg Fe/mL). The cells were incubated at concentrations of 50, 100, and 200 µg/mL in culture medium. The choice of SPION concentrations was based on earlier research for optimal concentration for subsequent analyses[130]. In addition to the samples, a negative control was included where cells were not incubated with SPIONs. After

incubation for 24 or 48 hours, the medium was removed, and the cells were washed three times with 1x PBS. Subsequently, the cells were fixed in 4% paraformaldehyde (PFA) (in 1x PBS) for 20 minutes and washed three times for 5 minutes with 1x PBS. Next, the cells were rinsed once with distilled H_2O (dH_2O) and once with 70% EtOH for 2 minutes. The cells were then rinsed again with dH_2O and stained with potassium ferrocyanide (Sigma-Aldrich), diluted in dH_2O ($K_4[Fe(CN)_6]$ x $3H_2O$) (**Table 3.2**), for 20 minutes while being protected from light (Prussian blue staining). After the staining process, cells were rinsed three times for 5 minutes with dH_2O. The plate was wrapped in parafilm and stored in the fridge until imaging unless the images were captured immediately. Imaging was performed using the Nikon Eclipse brightfield microscope (Nikon Corporation, Tokyo, Japan) with a Fi3 color camera. Images were taken with both 20x and 10x objectives, and quantification of cellular SPION uptake was carried out using the Fiji Software (version 2.14.0/1.54f). All staining experiments were performed in triplicates.

Table 3.2: Name of reagents and the amount added to make the Prussian blue staining. The Prussian blue stain was freshly made the morning before use.

REAGENT	VOLUME
dH_2O	9,95 mL
Concentrated HCl	0,05 mL
($K_4[Fe(CN)_6]$ x $3H_2O$) (potassium ferrocyanide)	0,1 g

3.2.2 Preparation of Cell Samples Prior to TEM (Transmission Electron Microscopy)

$8,5x10^5$ of H16 cells were seeded into each of three separate T25 flasks containing culture medium. One flask served as a control, while the remaining two were designated to receive uncoated SPIONs at concentrations of 50 and 100 μg/mL. After seeding, the flasks were incubated overnight at standard incubator conditions to facilitate cell adhesion. On the subsequent day, the appropriate SPION concentrations were added to the designated flasks. Following a 24-hour incubation, the flasks were washed twice with 1x PBS to remove any residual SPIONs before trypsinization. The cells were then neutralized by adding culture medium as described in **Section 3.1.1**. The cell suspension was transferred to a 15 mL Falcon tube (Sarstedt AG & Co.) and centrifuged at 248 x g for 5 minutes (Jouan B4i, Thermo Fischer Scientific). After removing the supernatant, the cell pellet was resuspended in 1x PBS and centrifuged again at 248 x g for 5 minutes. This washing step was repeated twice.

Karnovsky´s fixative was then added to the cell pellet and mixed thoroughly. The samples were fixed overnight at 4°C. Karnovsky´s fixative was prepared as outlined in **Table 3.2.2**, with 1 mL of fixative added to each pellet.

Table 3.2.2: Karnovsky´s fixative with a final volume of 5 mL.

REAGENT	VOLUME	COMPANY
0,2 M Na Cacodylate Buffer	2,5 mL	
0,2 M Dimethylarsinic acid sodium salt trihydrate		Sigma-Aldrich
0,2 M Sucrose		Sigma-Aldrich
0,005 M Calcium chloride dihydrate		Sigma-Aldrich
50% Glutaraldehyde		Electron Microscopy
	250 μL	Sciences (Hatfield, PA, USA)
10% PFA	1 mL	Sigma-Aldrich
Milli-Q water	1,25 mL	Sigma-Aldrich

The following day, samples were fixed in 2,5% glutaraldehyde (in 0,1 M Na cacodylate buffer) and 2% PFA for 24 hours at 4°C. Postfixation was done for 1 hour on ice in 1% osmium tetroxide (Electron Microscopy Sciences, #19134) diluted in 0,1 M Na cacodylate buffer, followed by two washes. The samples were then dehydrated using a graded ethanol series (30%, 50%, 70%, 96%, and 100%) and transferred to a 1:1 solution of 100% ethanol and propylene oxide for 15 minutes. Next, they were transferred to 100% propylene oxide for 15 minutes before gradually introducing Agar 100 resin (Agar Scientific, Stansted, UK, R1031). The samples were then placed in a small drop of 100% resin to let the excess propylene oxide evaporate for 1 hour. They were then transferred to 100% resin, placed in molds (beam capsules), and left at RT overnight. The molds were then placed at 60°C for 48 hours to polymerize. Ultrathin sections (~60 nm) were placed on 200 mesh formvar-coated (EMD Millipore Corporation, Darmstadt, Germany, #15820) copper grids (Electron Microscopy Sciences, #G100H-Cu) and stained with 2% uranyl acetate (Electron Microscopy Sciences, #22400) and lead citrate (VWR International, Radnor, PA, USA, #1,07398). Grids were imaged through a transmission electron microscopy (TEM) using a HT7800 RuliTEM instrument (Hitachi, Tokyo, Japan) at 100 kV.

3.3   Proliferation Assay of Cells Incubated with SPIONs

A cell proliferation assay was performed after a 24-hour SPION incubation. 100 000 cells were seeded per well in flat bottom 24-well plates (Nunc™, Thermo Fisher Scientific) and placed in the incubator at standard incubator conditions for 24 hours. The following day dextran-coated and uncoated SPIONs were added in three different concentrations (50, 100, and 200 µg/mL) in duplicates, beside an untreated control, and placed in the incubator overnight. The next day all wells were washed twice with 1x PBS before new culture medium was added and the plate was placed in the IncuCyte® Live-Cell Analysis System (Sartorius AG, Göttingen, Germany) at standard incubator conditions. The cells were imaged every two hours for 48 hours, and their confluency was determined using masking analysis in the IncuCyte® S3 software (Sartorius AG). Data was analyzed using GraphPad Prism 10 for MacOS (version 10.1.0 (264), GraphPad Software Inc., La Jolla, CA, USA). The experiments with dextran-coated SPIONs were performed in triplicate, whereas experiments involving uncoated SPIONs were performed once.

3.4   Isolation of EVs

EVs can be isolated using various methods. Two common approaches are differential centrifugation and size exclusion chromatography (SEC). Differential centrifugation applies different centrifugal forces to separate cellular debris, larger microvesicles, and smaller EVs. While widely used, it risks co-pelleting non-vesicular contaminants, altering EV morphology and integrity, and is time-consuming. SEC offers a gentler alternative by separating particles based on size, with larger particles eluting first[131]. This method, described in detail by Sidhom et al., uses qEV columns to minimize larger vesicles and debris, resulting in higher purity and better preservation of EV integrity. Additionally, SEC is more efficient, yielding higher concentrations of EVs compared to differential centrifugation

3.4.1   EV-Depleted Culture Medium for Isolation of EVs

FBS is used to supplement cell culture medium as a nutrient, but it also contains significant quantities of bovine-EVs, necessitating depletion of them from the FBS before the EV isolation experiments were carried out. The FBS (Sigma-Aldrich) was transferred to ultracentrifuge sealing tubes (Beckman Coulter, Brea, CA, USA), topped up with filtered 1x PBS and sealed with a Tube Topper (Beckman Coulter). Then, the tubes were centrifuged at

1,17x10^5 x *g* for 18 hours at 4°C in an ultracentrifuge (L-70 Ultracentrifuge, Beckman Coulter). After centrifugation, the supernatant was transferred to 50 mL Falcon Tubes (Sarstedt AG & Co.) through a 2 µm syringe filter (Sigma-Aldrich) to remove any remaining large particles or debris. Further, the filtered FBS was heat-inactivated in a water bath at 56°C for 30 minutes to inhibit the activity of complement components, inactivate potential virus, and prevent contamination of mycoplasma. The EV-free, heat inactivated FBS was subsequently stored at -20°C until use. Culture medium without EVs (referred to as EV-free culture medium) was prepared following the guidelines outlined in **Table 3.4.1.**

Table 3.4.1: Reagents, providers, and amount needed to make EV-free culture medium.

REAGENT	VOLUME	COMPANY
DMEM	450 mL	Sigma-Aldrich
FBS (filtered as described above)	50 mL	Sigma-Aldrich
L-Glutamine	10 mL	BioWhittaker
Penicillin/Streptomycin	10 mL	BioWhittaker
NEAA 100x MEM Non-Essential Amino Acids	16 mL	Biowest, Nuaillé, France
Plasmocin	100 µL	Invitrogen

For isolation of EVs, cells were cultured in T175 flasks with 25 mL of EV-free culture medium which supported cell growth for 48-72 hours (~90% confluency). The cells were washed with 1x PBS, collected as described in **Section 3.1.1**, and counted as described in **Section 3.1.2**. 10 mL of the cell suspension was centrifuged at 248 x *g* for 5 minutes (Jouan B4i, Thermo Fischer Scientific). Thereafter, the cell pellet was resuspended in 10 mL 1x PBS and recentrifuged at same speed and time. Then, the cell pellet was preserved by freezing at -80°C until use, serving as a cell-specific control for Western blotting.

3.4.2   Isolation of EVs Through Differential Centrifugation

Conditioned culture medium from eight T175 flasks was transferred to a total of four 50 mL Falcon Tubes (Sarstedt AG & Co.) and centrifuged at 248 x *g* for 5 minutes (Jouan B4i, Thermo Fisher Scientific) to remove cell debris. Thereafter, the supernatant was centrifuged at 2000 x *g* for 20 minutes (Eppendorf® AG Centrifuge 581/5810R, Hamburg, Germany) at 4°C for removal of apoptotic bodies. Subsequently, the supernatants were transferred to six ultracentrifuge sealing tubes (Beckman Coulter) with a 50 mL syringe (BD, Becton Dickinson and Company, Franklin Lanes, NJ, USA) with a disposable hypodermic needle (B. Braun,

Melsungen, Germany) and topped up with filtered 1x PBS. All potential air bubbles were removed before sealing with a Tube Topper (Beckman Coulter) and placed in a Ti70 rotor (Beckman Coulter) for ultracentrifugation at $1,88x10^4$ x g and 4°C for 25 minutes using a Beckman Optima L-70 Ultracentrifuge (Beckman Coulter). Subsequently, the supernatants were transferred to new ultracentrifuge tubes, topped up with filtered 1x PBS, and centrifuged at $1,17x10^5$ x g and 4°C for 2 hours (Beckman Optima L-70 Ultracentrifuge, Beckman Coulter) to get a pellet of EVs in each tube. The top of the tubes was then cut off to discard all the conditioned culture medium. The pellets were transferred to one 5 mL Open-Top ultracentrifuge tube (Beckman Coulter) by pipetting the pellet carefully. The tube bottoms were rinsed twice with 500 μL of filtered 1x PBS to ensure optimal collection of EVs. The Open-Top ultracentrifuge tube was topped up with filtered 1x PBS, placed in the MLS-50 swinging-bucket rotor (Beckman Coulter) in the Optima MAX-XP tabletop ultracentrifuge (Beckman Coulter), and centrifuged at 100 000 x g and 4°C for 1 hour to rinse the EVs. The isolation process from cell culturing to concentrated EV sample through differential centrifugation is illustrated in **Fig. 3.1**.
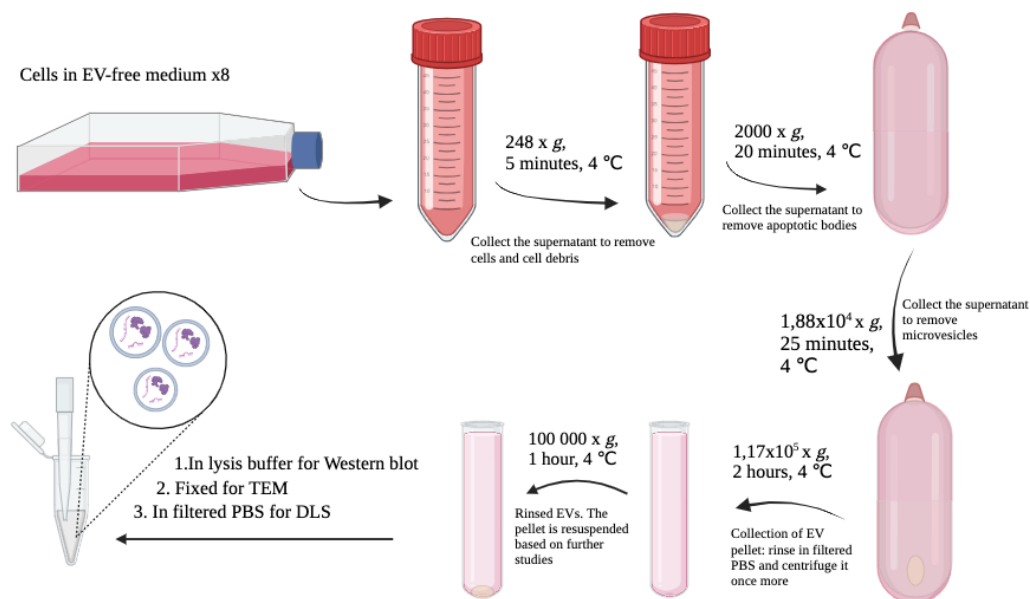
Figure 3.1: Overview of the isolation process using differential centrifugation from cell culturing to concentrated EV sample ready for analysis in DLS (dynamic light scattering), Western blot and TEM. A detailed illustration of the initial ultracentrifugation steps including speed, temperature, and duration leading to resuspension of the pellet with 1x filtered PBS, fixative, or lysis buffer before storage in the freezer (-80°C) for future analyses. The samples were used in DLS for EV size measurements, in Western blot for detecting EV markers, and in TEM for validating the typical EV shape and size. Created with BioRender.com.

3.4.2.1 Processing of the Pellet After Differential Centrifugation

The EV pellet was processed differently, according to the subsequent experiments. For DLS, the pellet was resuspended in 100 µL filtered 1x PBS and transferred to an Eppendorf tube. 10 µL was removed and mixed with a drop of 2,5% glutaraldehyde for TEM (**Table 3.4.2**).

For Western blot analysis, the pellet was resuspended in 30 µL lysis buffer (**Table 3.4.2**) and transferred to an Eppendorf tube. When resuspending in this buffer, a procedure of lysis was performed which included a total amount of 30 minutes on ice, while the sample was being vortexed every 10 minutes. After 30 minutes, the Eppendorf tube was centrifuged at 13 523 x g and 4°C for 10 minutes (Eppendorf^{TM} 5424R Microcentrifuge, Thermo Fisher Scientific). Following this step, the supernatant was transferred to a new Eppendorf tube and frozen at -80°C until use.

Table 3.4.2: Reagents for making lysis buffer and 2,5% glutaraldehyde.

REAGENT	COMPANY
Lysis buffer (final volume of 1 mL)	
900 µL RIPA buffer	Thermo Fisher Scientific
100 µL 10x protease and phosphatase inhibitors	Thermo Fisher Scientific
2,5 % Glutaraldehyde (final volume of 1 mL)	
950 µL 0,2 M Na Cacodylate Buffer	
0,2 M Dimethylarsinic acid sodium salt trihydrate	Sigma-Aldrich
0,2 M Sucrose	Sigma-Aldrich
0,005 M Calcium chloride dihydrate	Sigma-Aldrich
50 µL 50% Glutaraldehyde	Electron Microscopy Sciences

For quantification of resuspended EVs, 5 µL was transferred from the 100 µL 1x filtered PBS/pellet-resuspension to a new Eppendorf tube supplemented with 5 µL of lysis buffer (**Table 3.4.2**). Subsequently, the procedure of lysis was performed as mentioned above, and quantification done by applying 2 µL of the lysed sample to Direct Detect® Assay-free Cards (MilliporeSigma, Burlington, MA, USA) measured on the Direct Detect® Spectrometer (MilliporeSigma).

3.4.3 Isolation of EVs Using the Automatic Fraction Collector (AFC)

Cells were cultured in two T175 flasks containing 25 mL of EV-free culture medium for 48-72 hours (~90% confluency) and incubated at standard incubator conditions. The conditioned culture medium was collected into a 50 mL Falcon tube (Sarstedt AG & Co.) and centrifuged

following the protocol described in **Section 3.4.2** stopping after the centrifugation step at 2000 x g for 20 minutes at 4°C (Eppendorf® Centrifuge 581/5810R). The supernatant was kept aimed at removing apoptotic bodies. Cells were harvested as described in **Section 3.1.1**, counted as described in **Section 3.1.2**, and cell pellet from 10 mL EV-free culture medium was frozen as described in **Section 3.4.2**.

For up-concentration, the sample was loaded onto a Merck Amicon^{TM} Ultra-15 Centrifugal Filter (MilliporeSigma), and centrifuged at 3000 x g for 10 minutes x 5-7 at 4°C (Eppendorf® AG Centrifuge 581/5810R). The eluted medium was then discarded, and the filter was filled up with the remaining conditioned culture medium between the spins. Upon complete loading of the tube with medium, it underwent further centrifugation until reaching a final volume of 500 µL, resulting in an up-concentrated sample which was transferred to an Eppendorf tube. The number of required 10-minute spins to achieve a final volume of 500 µL ranged from 5 to 7, depending on how concentrated the sample was.

After concentration through ultracentrifugation, an Automatic Fraction Collector (AFC) (Izon Science, Christchurch, New Zealand) and a qEVoriginal (500 µL) 70 nm Gen 2 Isolation Column (Izon Science) were used to isolate EVs. First, the collector was calibrated using a 10 g weight to ensure the accuracy, precision, and reliability of fraction collection. Then, 13 Eppendorf tubes were labelled and positioned in the carousel. The isolation column, along with a funnel, was then set in place and filled with 1x filtered PBS for a thorough flushing process. After a 10-minute flush, the concentrated 500 µL sample was loaded onto the column, and the collection commenced. Once the entire sample volume had been absorbed by the column, the top of the column was filled with 1x filtered PBS. The obtained fractions were stored in the fridge until further use.

During the isolation of EVs from a new cell line, it was crucial to identify the fractions containing EVs. To achieve this, a Western blot analysis was performed on all the fractions, following the procedure outlined in **Section 3.5**. The fractions rich in EVs and low in proteins, based on the Western blot result, were collected, and used for further analysis.

The fractions containing EVs, as confirmed by the Western blot analysis, were transferred to a Merck Amicon^{TM} Ultra-0.5 Centrifugal Filter Units (MilliporeSigma) and centrifuged at 16 000 x g for 2 minutes (Eppendorf^{TM} 5424 Microcentrifuge, Thermo Fisher Scientific).

Following the initial spin, the eluted content was discharged, and the filter was replenished with remaining sample. Upon completing the concentration of all fractions containing EVs and those comprising only proteins, the desired final volume was standardized to 300 µL. The number of required 2-minute spins to achieve a final volume of 300 µL ranged from 7 to 10, depending on the concentration of the sample. This volume was aliquoted into small Eppendorf's, with each containing 30 µL of sample, and subsequently frozen at -80°C until further analysis. The isolation process from cell culturing to concentrated EV sample through SEC is illustrated in **Fig. 3.2**.
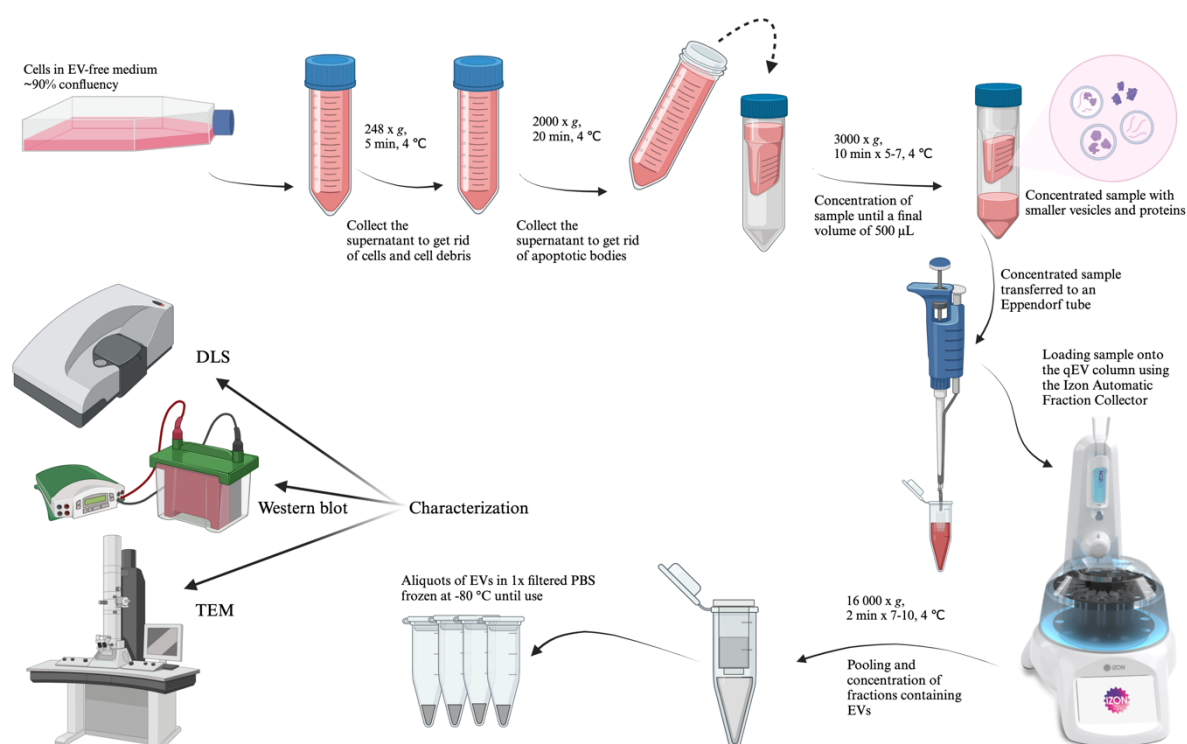
Figure 3.2: Schematic overview of the isolation process using AFC from cell culturing to concentrated EV sample ready to be analyzed in DLS, Western blot and TEM. A detailed illustration of the initial centrifugation steps leading to SEC using the IZON AFC technology and the final up-concentration of the EV sample before storage in the freezer for future analyses. The samples were used in DLS for EV size measurements, in Western blot for detecting EV markers, and in TEM for validating the typical EV shape and size. Created with BioRender.com.

3.5   SDS-PAGE and Western Blot for Detection of EV Proteins

Sodium dodecyl sulfate polyacrylamide gel electrophoresis (SDS-PAGE) and Western blot analyses were used to detect EV markers in the fractions obtained from the EV isolation process, as detailed in **Section 3.4.3**. During the initial characterization of EVs from a novel cell line, Western blotting was performed on all fractions from the isolation to ascertain which

ones contained EVs. Subsequent rounds of experiments focused on selectively pooling fractions containing EVs. The pooled material underwent Western blot analysis together with lysed cells collected before centrifugation (**Section 3.4.1**). The fractioned samples were aliquoted into Eppendorf tubes, each containing 30 µL, and stored at -80°C until use.

Table 3.5: Reagents used for SDS-PAGE and Western blot.

REAGENT	COMPANY
Running buffer	
50 mL MOPS SDS Running Buffer (20x)	NuPAGE®, Invitrogen
950 mL distilled water	-
500 µL Antioxidant	NuPAGE®, Invitrogen
Transfer buffer	
50 mL Transfer buffer (20x)	NuPAGE®, Invitrogen
100 mL methanol	Sigma-Aldrich
1 mL antioxidant	NuPAGE®, Invitrogen
850 mL Milli-Q® water	Sigma-Aldrich
10x Tris-Buffered Saline (10x TBS)	
24 g Tris Base	Sigma-Aldrich
88 g NaCl	Sigma-Aldrich
1000 mL Milli-Q® water	Sigma-Aldrich
1x TBS, 0,1% Tween®	
100 mL 10x TBS (pH 7,6)	
900 mL distilled water	
1 mL Tween® 20	Sigma-Aldrich
Blocking buffer	
50 mL 1x TBS-Tween®	
2,5 g Skim milk powder	Sigma-Aldrich
Lithium dodecyl sulfate (LDS) Sample Buffer (4x)	NuPAGE®, Invitrogen
Sample Reducing Agent (10x)	Bolt^{TM}, Invitrogen
PageRuler^{TM} Plus Prestained Protein Ladder 10-250 kDa	Thermo Fisher Scientific
SuperSignal^{TM} West Pico PLUS Chemiluminiscent Substrate	Thermo Fisher Scientific
SuperSignal^{TM} West Femto Maximum Sensitivity Substrate	Thermo Fisher Scientific
Ponceau staining	
0,1% Ponceau	Sigma-Aldrich
5% Acetic acid	Sigma-Aldrich
Primary antibodies	
Calnexin (C6C9) Rabbit mouse antibody (mAb). Cat. #2679	Cell Signaling Technology
FLOT1 (D2V7J) XP ® Rabbit mAb. Cat. #18634	(Danvers, MA, USA)
TSG101 (E6V1X) Rabbit mAb. Cat. #72312	
CD9 (D8O1A) Rabbit mAb. Cat. #13174	

CD81 (D3N2D) Rabbit mAb. Cat. #56039	
Secondary antibody	
Goat F(ab´)₂ Fragment Anti-Rabbit IgG (H+L)-Peroxidase (PN: IM0831) diluted 1:1 in glycerol	Immunotech, Beckman Coulter (Marseille, France)

The samples were thawed on ice, and Western blot preparation involved adding 5 µL of LDS Sample Buffer (4x), 2 µL of Sample Reducing Agent (10x), and 20 µg of the sample to Eppendorf tubes (**Table 3.5**). Milli-Q® water (Sigma-Aldrich) was then added to reach a final volume of 20 µL. The tubes were then placed on a 70°C heat block (Thermomixer R, Eppendorf) for 10 minutes to denature the proteins. This step ensured the disruption of non-covalent bonds and tertiary structures, allowing the uniform unfolding of proteins and enhancing their binding to sodium dodecyl sulfate (SDS). The samples were then vortexed and centrifuged (VWR International, Ministar Silverline) at 2000 x g for 20 seconds to ensure even mixing of the denatured sample components and remove any insoluble material that may have formed during the denaturation step.

A 1,5 mm 12-well/15-well 4-12% Bis-Tris gel (Invitrogen) was placed in a Western blot chamber (Mini Gel Tank, Thermo Fisher Scientific), and filled with running buffer (**Table 3.5**). The first lane received 8 µL of the PageRuler™ Plus Prestained Protein Ladder (Thermo Fisher Scientific), while the subsequent lanes were loaded with 37 µL of each sample. Long tips were used for sample loading to minimize the risk of contamination and enhance accuracy. The chamber, placed in a box of ice, ensured gel integrity and optimized protein separation and migration. Electrophoresis was conducted at a constant voltage of 200V for 50 minutes. After this step, the transfer from gel to a 0,2 µM pore nitrocellulose membrane (Amersham™, Protran™, Cytiva, Marlborough, MA, USA) was done using the freshly made transfer buffer (**Table 3.5**) in the XCell SureLock™ Mini-Cell Electrophoresis System (Invitrogen). The transfer chamber was prepared with pre-soaked filter paper, sponges, and the nitrocellulose membrane. The transfer, performed at a voltage of 30V, lasted 90 minutes while the system was kept on ice. The cooling on ice was maintained to prevent excessive heat generation, ensuring the preservation of protein integrity during the transfer process. After the transfer process, the membrane was incubated in Ponceau staining solution (**Table 3-5**) for 2-5 minutes at RT to confirm a successful transfer. Subsequently, the Ponceau staining was removed by washing with Milli-Q® water (Sigma-Aldrich). The membrane was then strategically cut using the ladder to estimate the positions of proteins. The sectioned membranes were then blocked with blocking buffer (**Table 3.5**) for 1 hour at RT on a SSL4

Rocker (Antylia Scientific, Vernon Hill, IL, USA). Following the blocking step, the membrane sections were washed twice with 1x TBS-Tween® for 5 seconds. Subsequently, they were incubated with primary antibodies (**Table 3.5**), diluted 1:1000 in blocking buffer, overnight at 4°C on a rocker.

The primary antibodies used were the following: Calnexin, predominantly located in the endoplasmic reticulum (ER) and is cell-specific, served as a negative marker for EVs due to its ER localization. Calnexin has an approximate size of 90 kDa. Flotillin-1 (FLOT1), associated with lipid rafts, is often used as a marker for EV-enriched fractions confirming the presence of EV fractions. Its size is approximately 49 kDa. Tumor susceptibility gene 101 (TSG101), commonly found in EVs, has an approximate size of 44 kDa. CD9 and CD81, tetraspanin proteins prevalent on the EV surface, contribute significantly to EV biogenesis and interactions with target cells. CD9 has an approximate size of 24-27 kDa, while CD81 is around 26 kDa.

The following day, the membranes were retrieved from 4°C and positioned on a rocker at RT. They were washed with 1x TBS-Tween®: 2x 5 seconds, 1x 15 minutes and 2x 5 minutes. 2 mL of the secondary antibody (**Table 3.5**) was applied to the sectioned membranes and incubated at RT for 1 hour. Following incubation, the membranes underwent washing steps with 1x TBS-Tween®: 2x 5 seconds, 1x 15 minutes and 4x 5 minutes. Both diluted primary antibodies and secondary antibodies were transferred to a 15 mL Falcon tube (Sarstedt AG & Co.) and frozen at -20°C for subsequent use as they can be thawed and reused 4-5 times.

The protein bands were visualized using Luminescent Image Analyzer LAS-3000 (Fujifilm Life Sciences, Cambridge, MA, USA). For protein detection, 200 µL of either SuperSignal™ West Pico PLUS Chemiluminiscent Substrate (Thermo Fisher Scientific) or SuperSignal™ West Femto Maximum Sensitivity Substrate (Thermo Fisher Scientific) was applied to the membranes. While in the Luminescent Image Analyser, the chemiluminescent substrates generate light through their reaction with horseradish peroxidase (HRP).

3.6 Analysis of EV Size Distribution Using Dynamic Light Scattering (DLS)

DLS is a technique employed to determine the size distribution profile of small particles. The method functions by shedding light on the dimensions of particles. Light scatters in all directions when hitting small particles (<250 nm), revealing information about particle movement over time due to Brownian motion. The samples were diluted to 5x, 10x, and 50x and placed in a clean, dust-free Malvern Panalytical 40 µL cuvette (Malvern Panalytical, Malvern, Worcestershire, UK). The samples were kept on ice until measurement and analyzed in the Zetasizer Nano ZS instrument (Malvern Panalytical, Malvern, Worcestershire, UK) at 4°C. Each cell line was analyzed in triplicate measurements.

3.7 Transmission Electron Microscopy

TEM is an imaging technique that allows visualization of structures at the nanoscale. By transmitting electrons through thin sections of EV samples, TEM produces detailed images, providing insights into EV size, shape, and contents. It is a highly appreciated technique in the study of EVs, offering high-quality images detailing morphology and internal structures.

3.7.1 Fixation of EVs and Negative Staining for TEM

A carbon-copper grid was positioned over a 10 µL droplet of a concentrated EV sample for a duration of 10-15 minutes. Following this, the grid underwent a triple wash with droplets of 30 µL of 1x filtered PBS. Next, the sample was post-fixed by adding a droplet of 2,5% glutaraldehyde (**Table 3.4**) to the grid for 10 minutes before repeating washing five times using droplets of dH_2O placed onto parafilm. Subsequently, the grid was held onto a droplet of 2% uranyl acetate, and the excess was absorbed by filter paper. This was repeated with a secondary droplet of uranyl acetate, with the grid left on this droplet for 30 seconds. Grids were air-dried and placed in a grid storage box until use. The post-fixation step served to enhance sample contrast and visibility.

3.7.2 EV Imaging

To capture images of EVs using a TEM, a specific process was followed to ensure high-quality results. The HT7800 RuliTEM instrument (Hitachi) was used, equipped with a 120 kV TEM and an Emsis Zarosa bottom-mounted CMOS camera (Emsis, Muenster, Germany).

Loaded copper grids coated by formvar carbon film were carefully inserted into the TEM holder and subsequently inserted into the TEM chamber. The TEM was set to the appropriate voltage, typically 100 kV for EV imaging. The focus and astigmatism controls were used to obtain a sharp image, and images were captured using the camera system attached to the TEM. During the imaging process, various settings, including contrast, brightness, and magnification were adjusted to achieve the desired results and to visualize the typical shape of EVs. Detailed metadata, including acquisition date, sample details and experimental conditions was maintained for thorough record-keeping and future reference. This was done in triplicate to ensure validity of the results.

3.8 Electroporation of EVs with Dextran-Coated SPIONs

The isolated EVs were labelled with dextran-coated SPIONs through electroporation. Electroporation involves applying an external electric field, surpassing the membrane´s dielectric strength. A short, high-voltage electric pulse temporarily disrupts the bilipid layer, enhancing EVs cargo leakage and uptake of surrounding molecules. Incubation of EVs with SPIONs during the electric pulse allows the substance to enter the lumen and be trapped upon membrane releasing. A more detailed description of the principle of electroporation of EVs is described in Lennaárd et al.[132]. For this, 50 µg of the EV sample was added to 10 µL of 50 mM Trehalose buffer (from a stock of 500 mM) together with 10 µL dextran-coated SPIONs. The volume was adjusted to 100 µL with 1x filtered PBS, as illustrated in **Table 3.8.1**. For determination the required volume for a 50 µg target, a calculation was performed using an example concentration of 1,071 µg/µL measured by the Direct Detect® Cards and Spectrometer (MilliporeSigma):

$$Volume\ of\ EVs: 50\ \mu g\ x\ \left(\frac{1}{1,071\ \mu g/\mu L}\right) = 46,7\ \mu L\ \text{of sample with EVs}$$

Table 3.8.1: Preparation for electroporation samples.

COMPONENTS	VOLUME (µL)
EV sample	46,7
500 mM Trehalose buffer	10
Dextran-coated SPIONs	10
1x filtered PBS	33,3
Total	**100**

Three samples were prepared: a control sample underwent electroporation without SPIONs, a "passive control" was incubated with SPIONs but not electroporated, and the electroporated sample was both incubated with SPIONs and electroporated. The NEPA21 Electroporator (NEPA GENE Co., Ltd., Shioyaki, Ichikawa, Chiba, Japan) was used with conditions detailed in **Table 3.8.2**.

Table 3.8.2: Conditions of electroporation of EVs using the NEPA21 Electroporator.

PULSE	CONDITIONS
Poring pulse	200 V, 5 ms length, 50 ms interval, 2 pulses, 10% decay rate
Transfer pulse	20 V, 50 ms length, 50 ms interval, 5 pulses, 40% decay rate

The samples were transferred to electroporation cuvettes (NEPA GENE Co., Ltd.), care was taken to avoid bubbles, and electroporated under the conditions listed in **Table 3.8.2**. Following electroporation, the cuvettes were removed, and the samples were gently pipetted into clean Eppendorf tubes, and then kept on ice for 1 hour. To purify the EVs, the samples were transferred to 5 mL Open-Top ultracentrifuge tubes (Beckman Coulter), filled with cold, filtered PBS, and centrifuged at 100 000 x g for 1 hour at 4°C in the MLS-50 swinging-bucket rotor (Beckman Coulter). The resulting pellet was resuspended in 50 µL 1x filtered PBS. 10 µL of the resuspended sample was used for TEM preparation as described in **Section 3.7.1**, and the remaining 40 µL was saved for the iron assay as described in **Section 3.10**.

3.9 Cell Incubation with Dextran-Coated and Uncoated SPIONs Prior to SEC

6×10^6 cells were seeded into each of three separate T175 flasks containing EV-free culture medium. One flask served as a control, while the remaining two were designated to receive dextran-coated or uncoated SPIONs at concentrations of 50 and 100 µg/mL, respectively. After seeding, the flasks were incubated overnight at standard incubator conditions to facilitate cell adhesion. On the subsequent day, the appropriate SPION concentrations were added to the designated flasks. Following incubation for 24 hours, the flasks underwent two washes with 1x PBS to remove any residual SPIONS, after which fresh EV-free culture medium was replenished. The flasks were then returned to the incubator and maintained for 48 hours before subsequent isolation through SEC as described in **Section 3.4.3** were carried out on the final day.

3.10 Determination of EV SPION Uptake by Iron Assay

The Iron Assay Kit (Sigma-Aldrich) was used to quantify the amount of iron content in the EV samples. To establish an iron standard curve, 10 µL of the 100 mM Iron Standard was diluted with 990 µL of distilled water, resulting in a 1 mM standard solution. Subsequently, 0, 2, 4, 6, 8, and 10 µL of the 1 mM standard solution were added to a 96-well plate (Sarstedt AG & Co.) to generate standard solutions of 0, 2, 4, 6, 8, and 10 nmol/well standards. The Iron Assay Buffer was added to each standard well to bring the total volume to 100 µL. Additionally, 5 µL of the Iron Reducer was added to each standard well.

For sample preparation, duplicate wells were used for a control with EVs not containing SPIONs, and another duplicate set for the sample incubated with SPIONs. To ensure uniform sample loading, the EV concentrations in the respective samples were measured using the Direct Detect® Assay-free Cards and Spectrometer (MilliporeSigma). To maintain procedural consistency, 60 µg of EVs were loaded each round the iron assay was performed. Iron Assay Buffer was then added to each sample well to reach a final volume of 100 µL. The plate was incubated for 30 minutes at 25°C. Subsequently, 100 µL of Iron Probe was added to both standards and samples, followed by another incubation, protected from light, for 60 minutes at 25°C. Absorbance was measured at 593 nm using a multi-well spectrophotometer (Multiskan^{TM} FC Microplate Photometer, Thermo Fisher Scientific). Below is an example demonstrating calculations for determining the iron content in the EV sample. These calculations are based on the results provided in **Section 4.5**.

Example of calculation: H16 incubated with 100 µg/mL dextran coated SPIONs
- $y \ (blanked \ Abs_{595}) \ = \ 0{,}1335$
- $x \ (nmol \ iron/well) = {}^{0{,}1335 \, - \, 0{,}0094}/_{0{,}0602} = 2{,}06 \ nmol \ iron/well$

  $(finding \ the \ x \ from \ the \ formula \ of \ the \ standard \ curve)$
- $x \ is \ plotted \ against \ y \ on \ the \ standard \ curve$

Calculating nmol iron/µg EV:
1. $µg \ EVs/well = \ 4{,}913 \ µg/µL \ x \ 12{,}2 \ µL \ = \ 59{,}94 \ µg \ EVs$

   Where 4,913 µg/uL is the concentration of EVs from Direct Detect® test, and 12,2 µL is the volume of sample added to the well
2. $nmol \ iron/µg \ EV = {}^{2{,}06 \ nmol \ iron/well}/_{59{,}94 \ µg \ EV/well} =$

   $\mathbf{0{,}034 \ nmol \ iron}/\mathbf{µg \ EV}$

3.11 MRI Analysis of Agar Phantoms Containing Cells or EVs Labeled with Uncoated SPIONs

First, LBM1 cells were prelabelled with uncoated SPIONs at a concentration of 200 µg/mL for 24 hours, following the procedure outlined in **Section 3.5**. A 2% Difco Agar Noble solution (BD, Becton Dickinson and Company) was prepared in Milli-Q® water (Sigma-Aldrich), microwaved, and placed in a water bath (50°C). Afterward, the agar solution was mixed in a 1:1 ratio with growth medium containing prelabeled cells. The resulting agar/cell solution was then aliquoted into four separate 2 mL Eppendorf tubes, each at concentrations of 500, 1000, 2000, and 4000 cells/µL. As negative controls, unlabeled cells were aliquoted into five additional 2 mL Eppendorf tubes, using the same cell concentrations as previously mentioned.

Second, EVs derived from LBM1, labeled with uncoated SPIONs at a concentration of 100 µg/mL, were isolated as described in **Section 3.4.3**. A 2% agar solution was prepared as described above and 2 mL agar was pipetted into each 2 mL Eppendorf tube. After allowing the tube to stand at RT for two minutes, 20 µL EV-SPIONs were added to the center of one Eppendorf tube, while another tube received 10 µL of EV-SPIONs using a BD insulin syringe with an Ultra-Fine™ 6 mm needle (BD, Becton Dickinson and Company). A third tube served as a control and contained 20 µL of 1x PBS.

MRI of phantoms was done using a 7 Tesla small animal MR scanner (MR Solutions, Guildford, UK) equipped with a circular transmit/receive coil. Imaging protocols included the acquisition of T2, T2 map, and T2* map, using the scan parameters presented in **Table 3.7**. These parameters encompassed the field of view (FOV) in mm, matrix size, slice thickness in mm, TR in ms, TE in ms, number of averages, and flip angle (FA°). This experiment was done once due to time constraints.

Table 3.7: Scan parameters for MRI of phantoms with cells and EVs.

		FOV (mm)	Matrix size	Slice thickness (mm)	TR (ms)	TE (ms)	Averages	FA°
Cells	T2	20x20	256x252	1	3000	45	2	90
	T2 map	20x20	256x192	1	2000	15	1	90
	T2* map	20x20	256x256	1	1000	4	1	60

EVs	T2	25x25	256x252	1	3000	45	2	90
	T2 map	25x25	256x192	1	2000	15	1	90
	T2* map	25x25	256x256	1	1000	4	2	60

4. Results

4.1   Characterization of EVs

4.1.1 Characterization of EVs from a Melanoma BM Cell Line with Differential Centrifugation

EVs were isolated from H16 cells incubated in EV-free culture medium. Due to change of method, EVs from H10 and LBM1 were not isolated through differential centrifugation. TEM was utilized to visualize the isolated EVs for characterization of their morphology, including shape, membrane structure, and size. **Fig. 4.1.1 a** illustrates a heterogeneity in size distribution and the cup-shaped morphology, which is characterized by a darker center and a lighter surrounding region representing the lipid bilayer structure.

Western blot, which is a commonly used method to detect proteins in EV samples, was performed as an additional method to confirm the successful isolation of EVs presented in **Fig. 4.1.1 b**. Calnexin, a cellular marker which served as a negative control, was positive solely in cells. The EV markers FLOT1 and TSG101 exhibited positive expression in both cells and EVs. However, as these markers may also be present in other cellular component, additional EV markers, CD9 and CD81, were included in this experiment. Selective positivity of CD9 and CD81 in the isolated EV fraction validates their presence within the EV population.

Quantification of particle size through DLS was used as a third method to confirm the successful isolation of EVs obtained through differential centrifugation, as presented in **Fig. 4.1.1 c**. Different dilutions were studied to see if a higher dilution could prevent aggregation of EVs in the sample, and potentially reduce multiple scattering. The curves for all three dilutions spanned from 50 nm to 1000 nm, with each reaching its highest peak around 180-200 nm. **Table 4.1.1** shows the triplicate measurements with the three different dilutions and the average. The results presented a small variation between the dilutions. However, the 50x dilution had the most defined peak, as the peaks for 5x and 10x dilutions carried over into larger particle sizes, as illustrated in **Fig. 4.1.1 c,** suggesting aggregation. The 50x dilution also exhibited the least variation between triplicate measurements (**Table 4.1.1**).
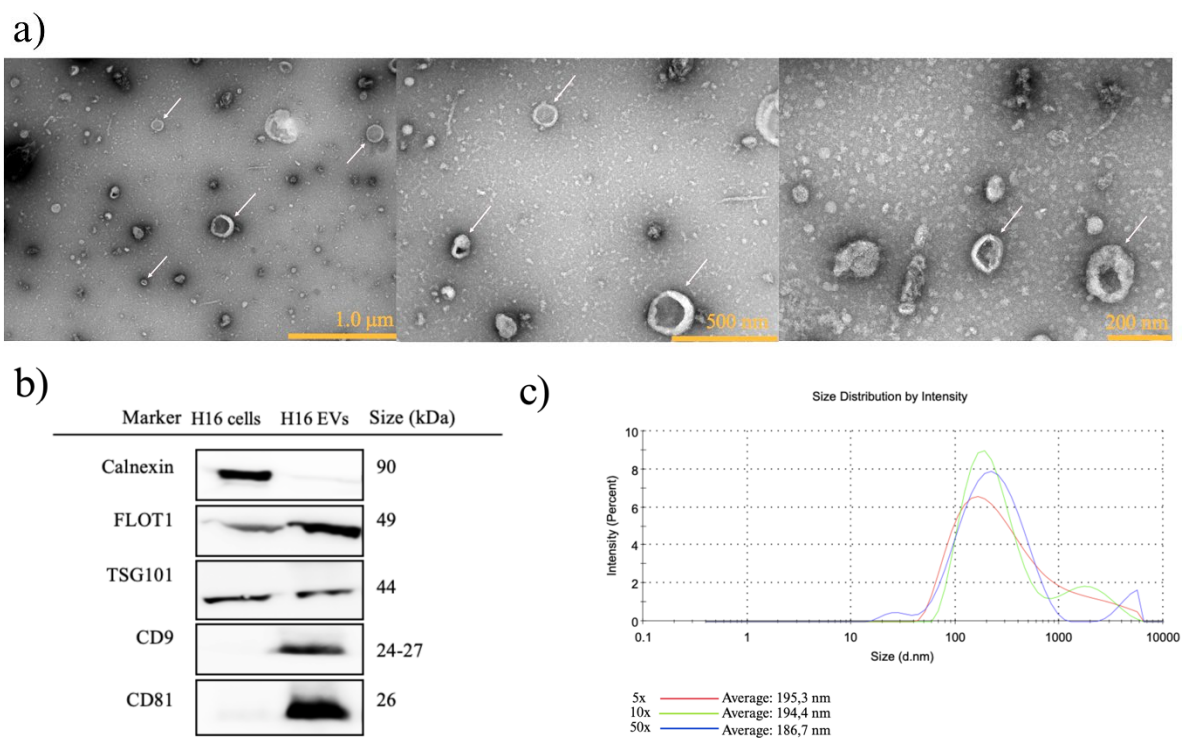
a)

b)

c)

Figure 4.1.1 – Characterization of H16-derived EVs after isolation through differential centrifugation: a) TEM images showing a wide field with EVs, magnified view of a smaller region within the sample, and further magnification of a smaller area to visualize the morphology details (white arrows). b) Western blot analysis of positive and negative EV markers in H16 cell and EV lysates. c) Size distribution plot of EVs retrieved from DLS with information about size (diameter in nm) and the intensity (%) of scattered light. The plot shows EVs in three different dilutions.

Table 4.1.1 – Particle size analysis (DLS) of H16-derived EVs with three dilutions in 1x filtered PBS.

Dilution	H16 EV size (d.nm)			Average ± SD (d.nm)
5x	195,3	220,0	351,6	255,6 ± 68,6
10x	194,9	226,4	322,6	248,0 ± 54,3
50x	186,7	227,5	279,6	231,3 ± 38,0

Table 4.1.1 includes EV size in diameter nanometer (d.nm) of three different experiments. The average and standard deviation between triplicate measurements is also presented in d.nm.

DLS provided insights into the size distribution profiles of H16-derived EVs, revealing distributions encompassing the upper size range typical for exosomes (30-150 nm) as well as the smaller size-range characteristic of microvesicles (100 nm-1 μm). Furthermore, TEM imaging provided visual confirmation of their characteristic morphology and dimensions, complemented by Western blot analysis demonstrating the absence of the cellular marker

calnexin in EVs but its presence in cells, along with the presence of EV-specific markers. These findings collective provide strong evidence supporting the successful isolation of EVs through differential centrifugation.

4.1.1.1 Calculating Yield of EVs After Differential Centrifugation

The concentration of EVs in the samples was determined by EV protein detection using Direct Detect® Spectrometer, and the EV yield was calculated by multiplying the measured concentration by the final volume of the sample. **Table 4.1.1.1** shows measurements from three rounds of isolation through differential centrifugation of H16-derived EVs. The results ranged from 100-300 μg per 100 μL sample from originally eight T175 flasks of MBM cells in EV-free culture medium.

Table 4.1.1.1 – Quantification of H16-derived EVs after isolation through differential centrifugation: (mean of triplicate measurements).

Cell line	EV protein concentration ± SD (μg/μL)	Final volume (μL)	EV yield ± SD (μg)
H16	1,861 ± 0,897	100	186,1 ± 89,7

4.1.2 Characterization of EVs from BM Cell Lines Through SEC

EVs were isolated through SEC from H16, H10, and LBM1 cells in conditioned culture medium. TEM was used to visualize the isolated EVs for characterization of their morphology, including shape, membrane structure, and size. The EVs displayed a predominantly uniform population, though with minor size variations indicating slight heterogeneity. Their morphology was characterized by the typical spherical structure, featuring lipid bilayers. TEM imaging illustrated a comprehensive representation of EVs across all three cell lines, as shown in **Fig. 4.1.2.1 a-i**.
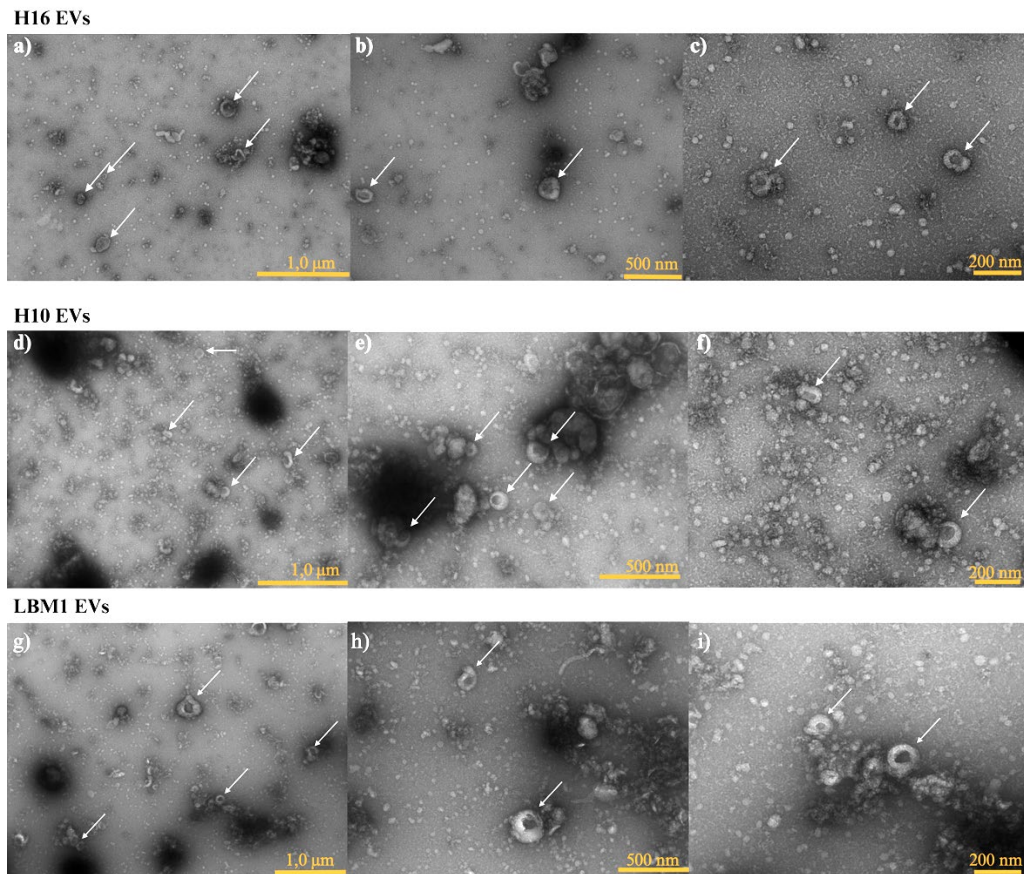
H16 EVs

H10 EVs

LBM1 EVs

Figure 4.1.2.1 – Images of EVs viewed by TEM to confirm successful isolation through SEC: a-c) EVs derived from H16 cells, d-f) EVs derived from H10 cells, and g-i) EVs derived from LBM1 cells. The images were captured at various magnifications, with scale bars representing 1 μm, 500 nm, and 200 nm, providing different levels of detail. White arrows show EVs.

Western blot analysis was performed as an additional validation of the isolation through SEC to detect specific protein markers in cell lysates and EVs. The results of H16, H10, and LBM1 revealed that the cellular marker calnexin was exclusively positive in cell lysates, with no presence in the EV fractions. Both FLOT1 and TSG101 proteins were detected in both lysates and EV fractions, indicating their presence in both cellular and extracellular samples. However, TSG101 exhibited stronger expression in cell lysates compared to EVs. The EV markers CD9 and CD81 were exclusively positive in the EV fractions, confirming their selective presence in the EVs (**Fig. 4.1.2.2**).
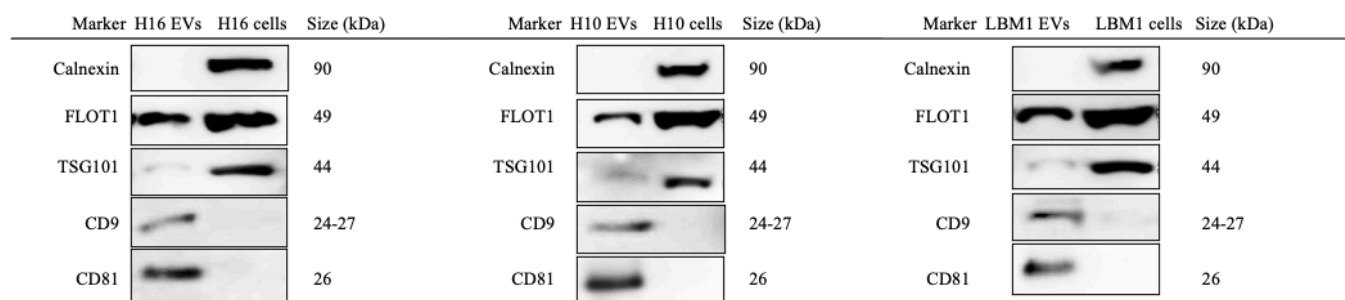
Figure 4.1.2.2 – Western blot analysis of cellular and EV markers within cell lysates and EVs derived from H16, H10 and LBM1.

DLS was performed to investigate the size distribution profiles of EVs derived from the three cell lines. To assess whether higher dilution could prevent EV aggregation, three dilutions were examined. **Fig. 4.1.2.3** illustrates that these dilutions displayed minor variations in average size. Notably, all dilutions exhibited two predominant curves: one smaller curve representing smaller vesicles (10-100 nm) and another with higher intensity spanning 100-1000 nm, indicating a polydisperse sample. The average EV sizes (**Table 4.1.2**) were within the typical range for sEVs (30-150 nm). However, some variability, particularly for H10, showed occasional larger vesicles (>150 nm).
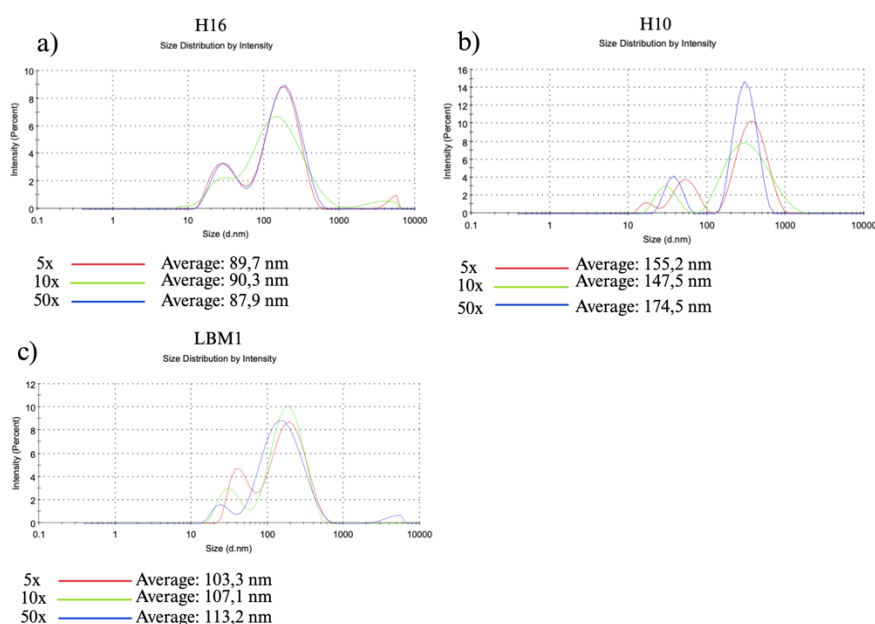
Figure 4.1.2.3 – Size distribution plot of EVs with three dilutions: Size distribution plot of EVs retrieved from DLS with information about size (diameter in nm) and the intensity (%) of scattered light. a) H16-derived EVs, b) H10-derived EVs, and c) LBM1-derived EVs. Average (size in nm) for the three dilution of each cell line is presented below the graphs.

Table 4.1.2 – DLS analysis results of EVs derived from H16, H10, and LBM1 isolated through SEC.

Dilution	EV size (d.nm)			Average ± SD (d. nm)
	H16			
5x	58,80	74,36	89,67	74,3 ± 12,6
10x	83,40	75,37	90,29	83,0 ± 6,1
50x	70,48	80,17	87,91	79,5 ± 7,1
	H10			
5x	181,2	155,2	90,32	142,2 ± 38,2
10x	182,8	147,5	84,91	138,4 ± 40,5
50x	171,9	174,5	83,10	143,1 ± 42,5
	LBM1			
5x	148,1	74,15	103,3	108,5 ± 30,4
10x	202,9	70,82	107,1	126,9 ± 55,7
50x	64,20	69,37	113,2	82,3 ± 22,0

4.1.2.1 Calculating Yield of EVs After SEC

The concentration of EVs in the samples was determined by protein detection using Direct Detect® Spectrometer, and the EV yield was calculated by multiplying the measured concentration by the final volume of the sample. **Table 4.1.2.1** shows measurements from three rounds of isolation through SEC of EVs derived from H16, H10, and LBM1. The results ranged from 600-1300 µg per 300 µL sample from originally two T175 flasks of cells in conditioned culture medium.

Table 4.1.2.1 – Quantification of EVs derived from H16, H10, and LBM1 following isolation through SEC (mean of triplicate measurements)

Cell line	Mean EV protein concentration ± SD (µg/µL)	Final volume (µL)	Mean EV yield ± SD (µg)
H16	3,490 ± 0,608	300	1047,1 ± 182,5
H10	2,784 ± 0,337	300	835,4 ± 101,1
LBM1	2,443 ± 0,576	300	732,9 ± 172,7

Table 4.1.2.2 compares the two isolation methods, taking into account the volume of conditioned culture medium used and the total EV yield based on EV protein concentration measured by the Direct Detect® Spectrometer. The comparison indicates that SEC yields up to 20 times more EVs compared to the widely recognized standard method of differential centrifugation.

Table 4.1.2.2: Comparison of two different methods of EV isolation and yield in perspective of conditioned cultured volume needed

Method of isolation	Cell line	Total EV yield (µg)	Conditioned culture medium (mL)	Concentration of EVs per mL medium (µg EV/mL)
Differential centrifugation	H16	186,1	200	0,931
SEC	H16	1047,1	50	20,940
SEC	H10	835,4	50	16,708
SEC	LBM1	732,9	50	14,658

4.2   Electroporation of EVs to Incorporate SPIONs

Electroporation was used to load SPIONs into EVs by briefly disturbing the phospholipid bilayer with an electrical current, allowing the iron nanoparticles to enter the EVs. Due to change of labeling method, electroporation was performed exclusively with EVs derived from H16 cells, and only with dextran-coated SPIONs. The isolation method used was differential centrifugation, with SEC being introduced at a later stage.

In TEM, SPION-loaded EVs are expected to exhibit darker regions compared to EVs without SPIONs, indicating the presence of the iron oxide nanoparticles within the vesicles. In some cases, it is possible to visualize the individual nanoparticles themselves. As seen in **Fig. 4.2.1 b**), the TEM images revealed a sparse presence of EVs across all samples, with only a limited number of EVs observed, particularly evident in the electroporated control and electroporated EV-SPION sample. In addition, darker regions in the EVs indicative of SPION uptake were not observed in the TEM images. The iron assay (**Fig. 4.2.1 a**) did not reveal any detectable iron in the electroporated sample. Only a small amount of iron was observed in the passive control, indicative of low levels of SPION when the EVs were only incubated with SPIONs and not electroporated.
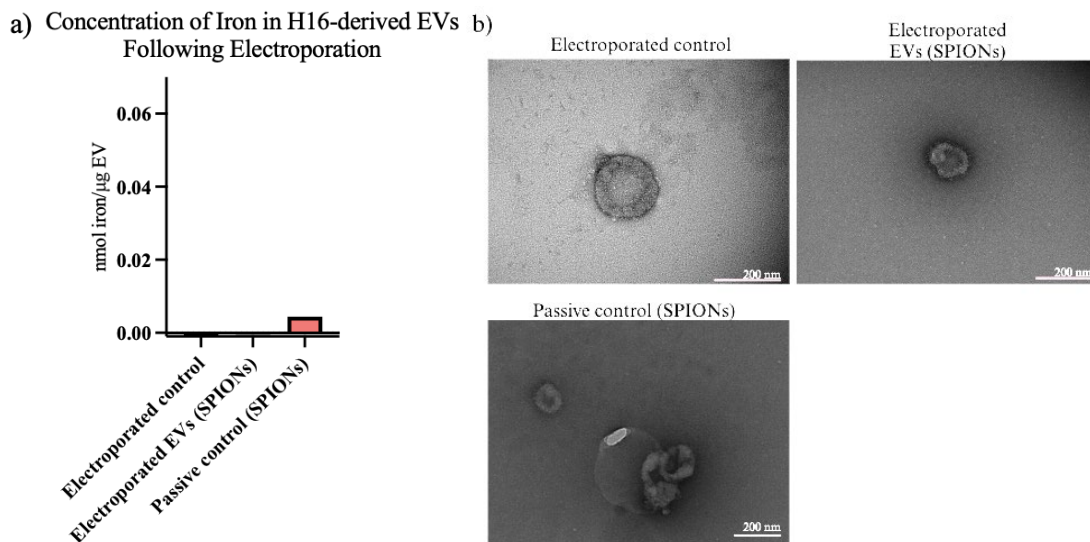
Figure 4.2.1 – Concentration of iron and TEM images of H16-derived EVs after electroporation: *a) nmol iron/μg EV in control, electroporated EVs and passive control. b) TEM images of samples after electroporation (upper images) and passive incubation with dextran-coated SPIONs (lower image). Scale bar=200 nm.*

4.3 Prussian Blue Staining and TEM for Visualization of Cellular Uptake of SPIONs

Prussian blue staining was done to visualize iron within H16 (**Fig. 4.3.1 a-b**) and LBM1 (**Fig. 4.3.1 c-d**) cells. The staining revealed successful presence of both SPION variants, with every single cell exhibiting a blue color, indicating uptake of the iron oxide nanoparticles. It was evident from the results that cell viability decreased with the high concentrations of dextran-coated SPIONs, particularly for H16 after 48 hours of incubation. There was a notable decrease in confluency compared to the untreated control, suggesting cell death, also characterized by round-shaped and clumped cells (**Fig. 4.3.1 a-b**). Conversely, cells exposed to uncoated SPIONs (5 nm) appeared to maintain higher viability, as indicated by a more confluent cell population across the three concentrations tested, with no major differences observed between the 24-hour and 48-hour incubation periods. Hence, cells incubated with 200 μg/mL of uncoated SPIONs seemed to be less confluent and exhibited a tendency towards increased aggregation (**Fig. 4.3.1 c-d**).

H16: Dextran-coated SPIONs (35 nm)
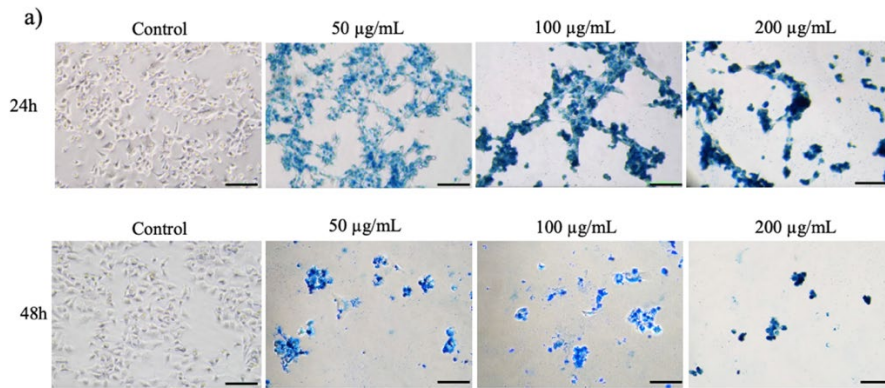
LBM1: Dextran-coated SPIONs (35 nm)
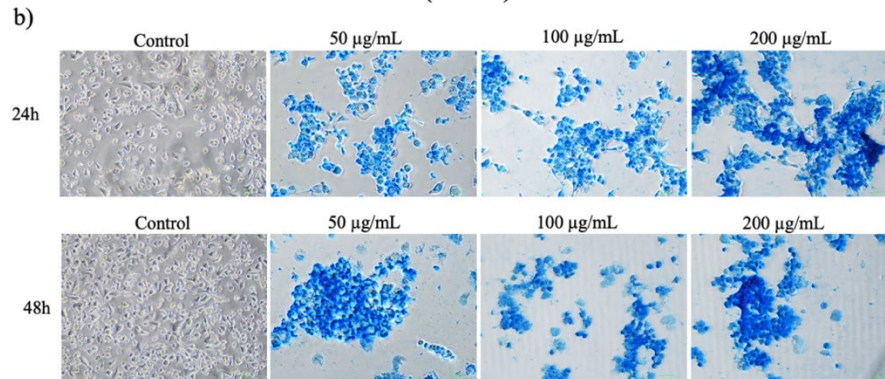
H16: Uncoated SPIONs (5 nm)

LBM1: Uncoated SPIONs (5 nm)

Figure 4.3.1 – Microscopic images after Prussian blue staining of H16 and LBM1 cells with two different SPIONs. *The cells have been incubated for 24 and 48 hours with 50, 100,*

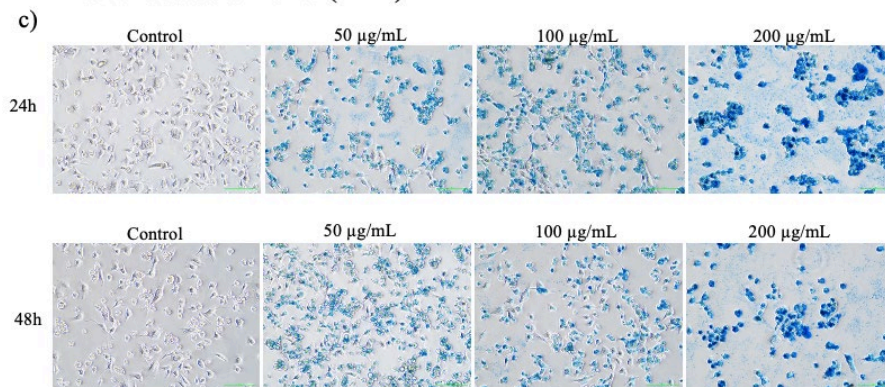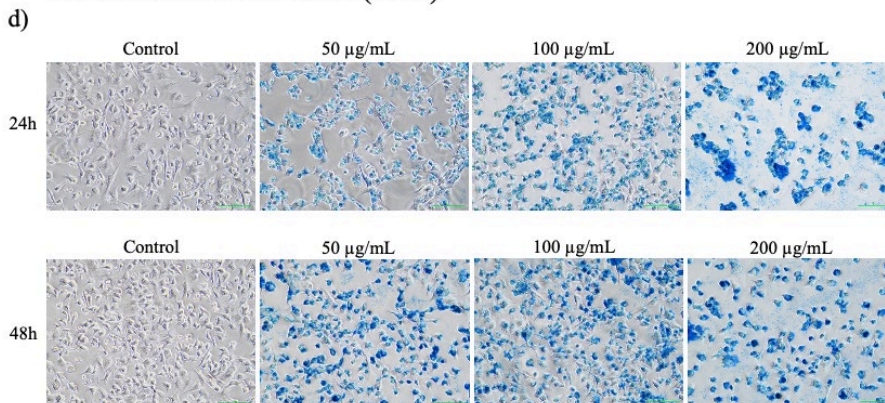*and 200 μg/mL dextran-coated and uncoated SPIONs, including a control without SPIONs. a) H16 cells incubated with dextran-coated SPIONs, b) LBM1 cells incubated with dextran-coated SPIONs, c) H16 cells incubated with uncoated SPIONs, and d) LBM1 cells incubated with uncoated SPIONs. The images were taken with a 20x objective. All scale bars are 100 μm and are highlighted in the first figure (a). N=3.*

TEM was used to visualize the internalization of uncoated SPIONs within H16 cells. Prior to embedding, cells were incubated for 24 hours with concentrations of 50 and 100 μg/mL, alongside an unlabeled control sample. Distinct granular structures visualized as clustered black dots, indicative of SPION presence, were successfully visualized in both concentrations, as presented in **Fig. 4.3.2.** These granular structures appeared to be oriented within intracellular vesicles (i.e. endosomes/lysosomes), suggesting an endocytic pathway for nanoparticle uptake. Furthermore, the SPIONs were in general observed in close proximity to or bound to the cell membrane, and not in the nucleus. No notable differences were observed between cells incubated with 50 μg/mL SPIONs and those incubated with 100 μg/mL SPIONs. In addition, no cellular damage was observed.

H16 50 μg/mL uncoated SPIONs
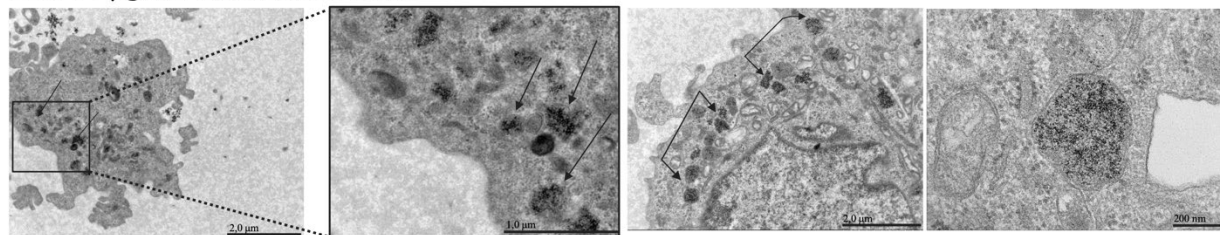
H16 100 μg/mL uncoated SPIONs
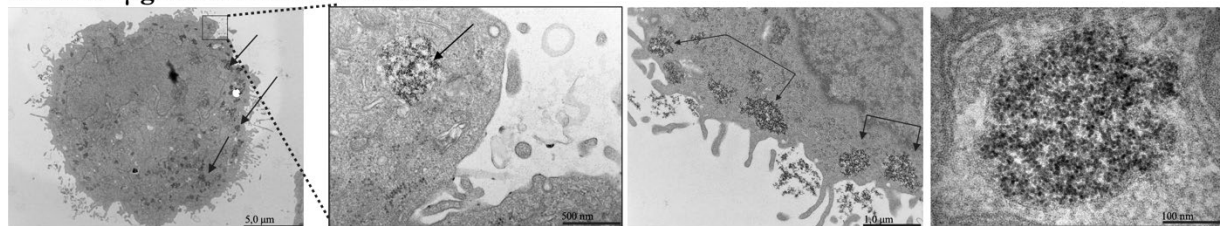
H16 Control
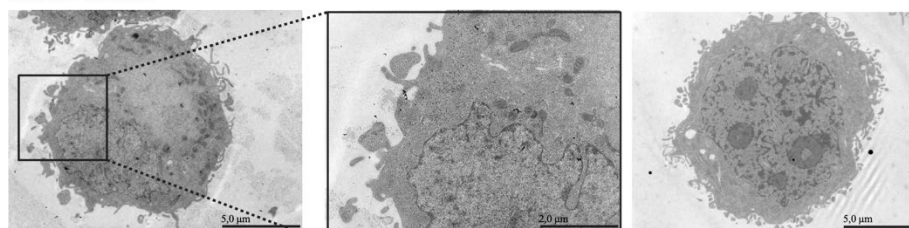
Figure 4.3.2 – TEM images of H16 cells labeled with uncoated SPIONs. *The figure also includes a control (lowermost images) without SPIONs. Black arrows indicate iron within the cell. The figure also represents a closer image (to the right) of a vesicle of SPIONs, where the sizes (5 nm) of the SPIONs are more closely visualized. N=1.*

4.4   Real-Time Cell Proliferation Assay of Iron-loaded BM Cells

A proliferation assay was carried out to provide information about the cytotoxic effects of different concentrations of SPIONs on cells. This was important information for the determination of SPION type and concentration for cell incubation with SPIONs prior to EV isolation. Following incubation with SPIONs for 24 hours, excess iron was removed through washing before plates were placed into the IncuCyte® Live-Cell Analysis System.

The IncuCyte® Live-Cell Analysis System was used for real-time image acquisition. Notably, discernible differences in confluency were observed between the control cells (no SPIONs) and cells incubated with three dextran-SPION concentrations at the beginning of imaging. **Fig. 4.4.1 a-b, d-e** illustrate consistently a low cell growth in both dextran-coated SPION-incubated H16 and LBM1 cell, suggestive of cellular death, opposite of the strong growth seen in the control cultures. The corresponding IncuCyte® images (**Fig. 4.4.1 c,f**) show elongated and healthy growing control cells, while those treated with dextran-coated SPIONs exhibited pronounced signs of cellular distress, characterized by their rounded apoptotic morphology. A one-way ANOVA analysis was performed on H16 and LBM1 cells (**Fig. 4.4.1 b,e**), revealing a significant difference in growth between the control cells and those incubated with dextran-coated SPIONs.
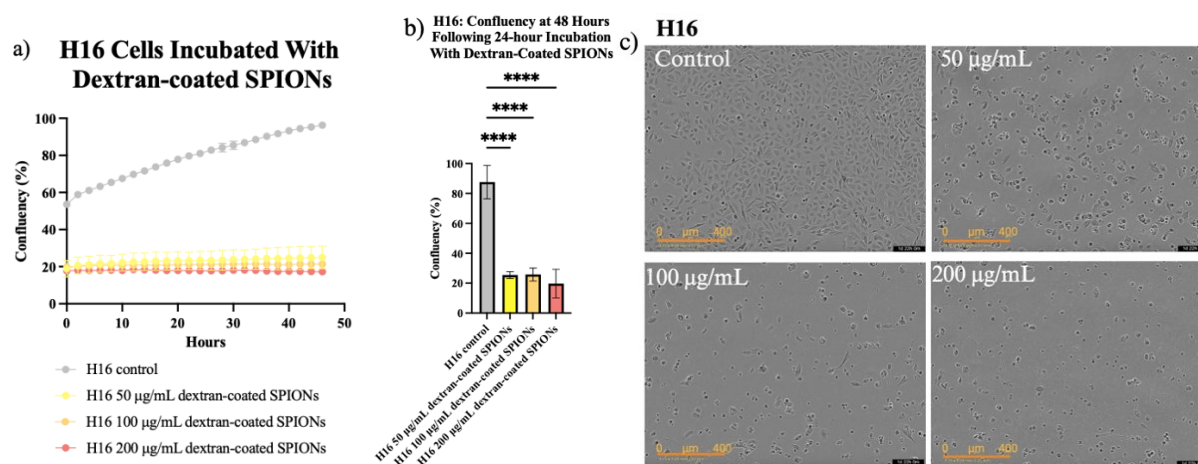
Figure 4.4.1 – Cell proliferation assay following 24-hour incubation with dextran-coated SPIONs: a-c) H16 and d-f) LBM1. a, d) Representative graph of 48 hour timelapse growth curve. b, e) Final % confluency after 48 hours of incubation. c, f) Representative images showing control along with the three dextran-coated SPION concentrations after 48 hours. The images were taken with a 10x objective. Scale bars=400 μm. N=3, mean ± SD. ****p<0,0001.

When exposed to high concentrations of uncoated SPIONs during a 48-hour incubation period, both H16 and LBM1 displayed normal growth patterns, as illustrated in **Fig. 4.4.2 a-b** and **d-e**. Live images captured after 48 hours, shown in **Fig. 4.4.2 c** (H16) and **f** (LBM1), reveal an even layer of healthy, proliferating cells. However, cells treated with SPION concentrations of 200 μg/mL exhibited a slower growth rate, particularly notable in the case of LBM1, where proliferation ceased after 24 hours (**Fig. 4.4.2 f**). This suggests that the highest SPION concentration can inhibit normal cell growth. It is worth noting, however, this experiment must be repeated to confirm these results.
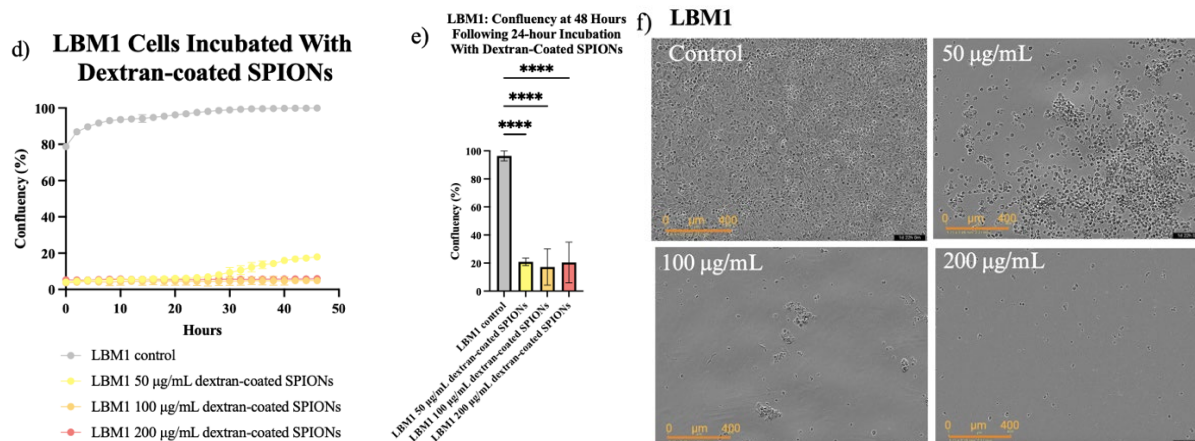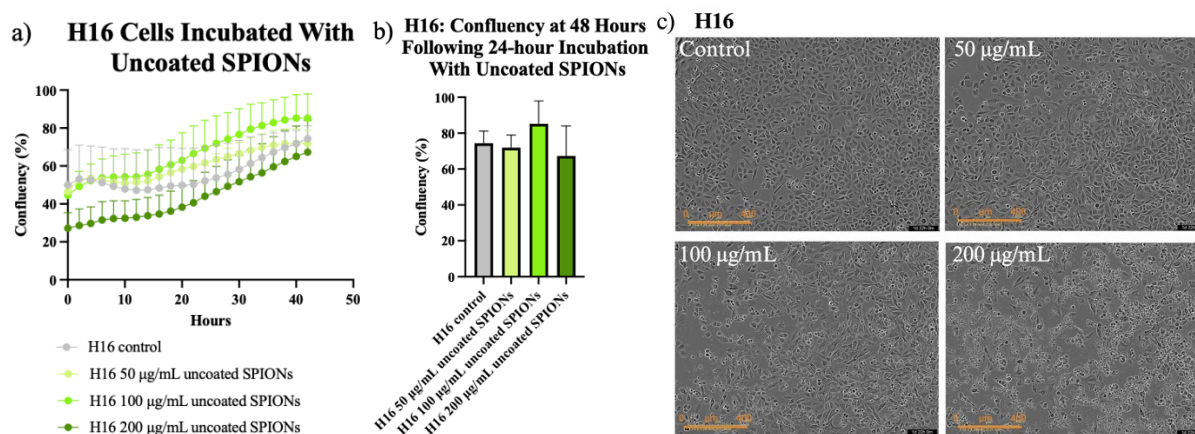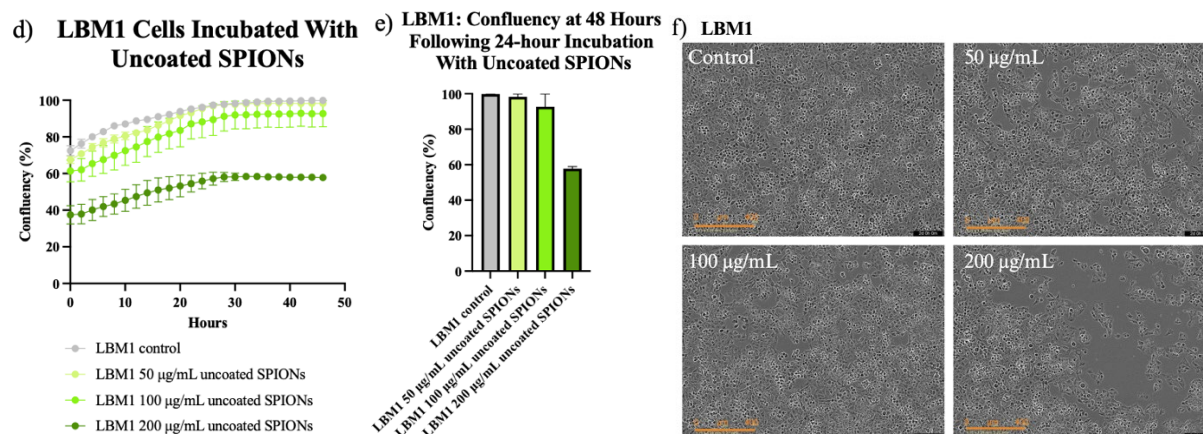
Figure 4.4.2 – Cell proliferation assay following 24-hour incubation with uncoated SPIONs: *a-c) H16 and d-f) LBM1. a, d) Representative graph of 48-hour timelapse growth curve. b, e) Final % confluency after 48 hours of incubation. c, f) Representative images showing control along with the three uncoated SPION concentrations after 48 hours. The images were taken with a 10x objective. Scale bars=400 μm. N=1, mean ± SD.*

4.5 Characterization of Iron Uptake in EVs

The colorimetric iron assay method was employed to quantify the iron concentration in the EV samples. H16 and LBM1 cell lines were chosen for this study due to their rapid growth rate. EVs were isolated through SEC due to change of isolation method. Both dextran-coated and uncoated SPIONs were used in this experiment. SPION concentrations of 50 and 100 μg/mL were used, as 200 μg/mL appeared cytotoxic to the cells based on Prussian blue staining and proliferation assay results. Additionally, a control group without SPIONs was included in each round of isolation. The samples were initially prepared in cell culture with SPION-incubation as described in **Section 3.5** before SEC.

Background values were determined using the 0 (blank) iron standard and subtracted from all readings to correct for background. The corrected values obtained from the appropriate iron standards were used to plot a standard curve. Iron was successfully detected colorimetric in the EV samples, and results were plotted on the iron assay standard curve (**Fig. 4.5.1 a**). Subsequently, the concentration of iron in EVs from H16 and LBM1 cells was calculated using the results and is presented in **Fig. 4.5.1 b** (nmol iron/μg EV). From the results obtained, EVs derived from LBM1 had a higher content of iron compared to EVs derived from H16. However, a SPION concentration of 100 μg/mL gave the highest concentration of EV-iron for both H16 and LBM1. An example of the calculations is presented in **Section 3.10**. Furthermore, TEM was used to detect dark spots within the EVs, validating the uptake

of iron. In **Fig. 4.5.1 c**, the dark areas are indicated by green arrows, providing visual confirmation of iron in the EVs. **Fig. 4.5.1 c** also illustrates a TEM sample comprised of dextran-coated SPIONs only. In this image, the SPIONs appear as individual black dots, although with slight variations in size.

Figure 4.5.1 – Characterization of iron uptake in EVs derived from H16 and LBM1: *a) Iron standard curve depicting colorimetric sample results, analyzed using a*

spectrophotometer with absorbance at 595 nm (y-axis), plotted against concentration of iron (nmol iron/well) (x-axis). The thick grey line represents the standard curve with 0, 2, 4, 6, 8, and 10 nmol iron/well, while the dotted line presents the calculated standard curve in a linear way. b) Calculated iron concentration in nmol iron/μg EV. c) TEM images illustrating EVs with iron oxide nanoparticles, including an image of dextran-coated SPIONs without EVs. All SPIONs used in these results were dextran-coated. N=1.

The same experiment was carried out for H16 and LBM1 incubated with uncoated SPIONs, and calculations were done in the same way as described above. While iron was successfully detected, the two types of SPIONs yielded similar results in terms of nmol iron per well, as depicted in **Fig. 4.5.2 a**. Both LBM1 and H16 cells incubated with 50 μg/mL of uncoated SPIONs exhibited a result of ~0,02 nmol iron/μg EV, while cells incubated with 100 μg/mL uncoated SPIONs showed a higher result of ~0,07 nmol iron/μg EV (**Fig. 4.5.2 b**). Furthermore, TEM imaging (**Fig. 4.5.2 c**) revealed darker areas within EVs, indicating the presence of SPIONs, as denoted by green arrows. Additionally, **Fig. 4.5.2 c** displays a TEM image with exclusively uncoated SPIONs as black dots, confirming their reported size (~5 nm).
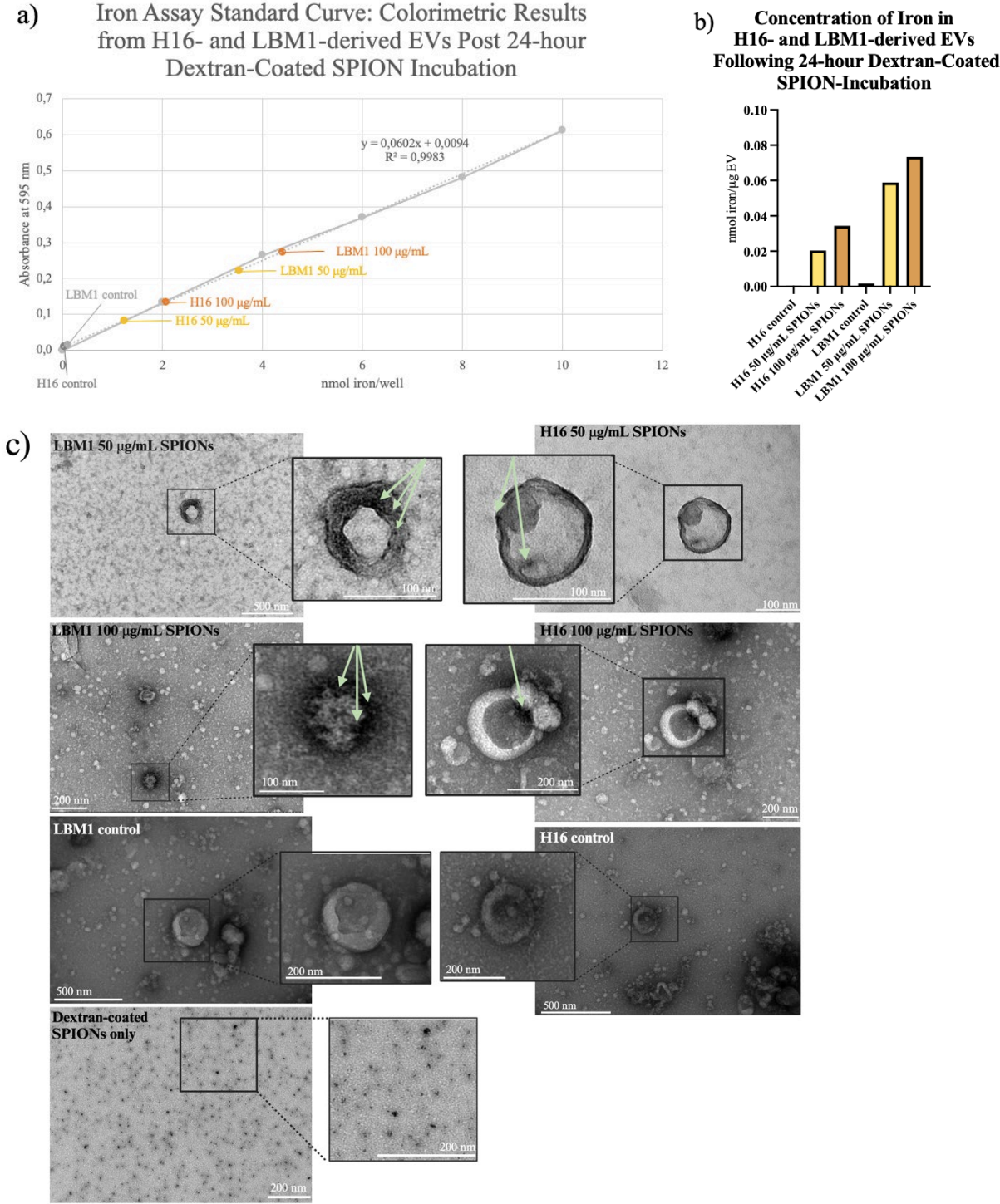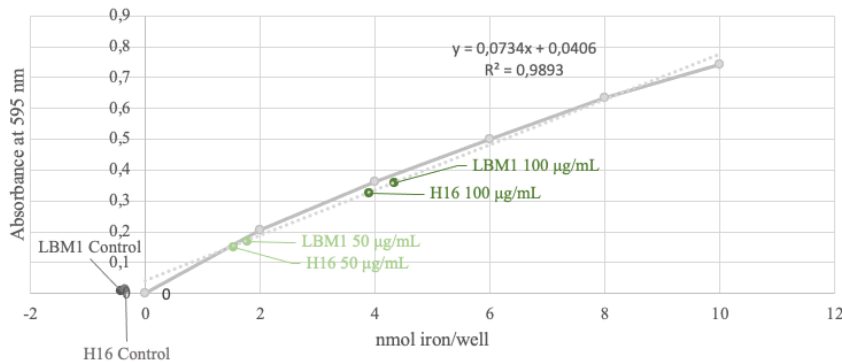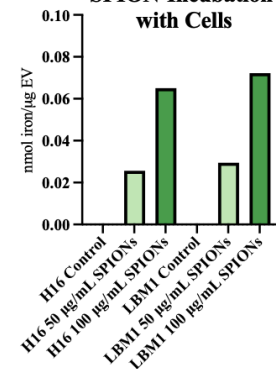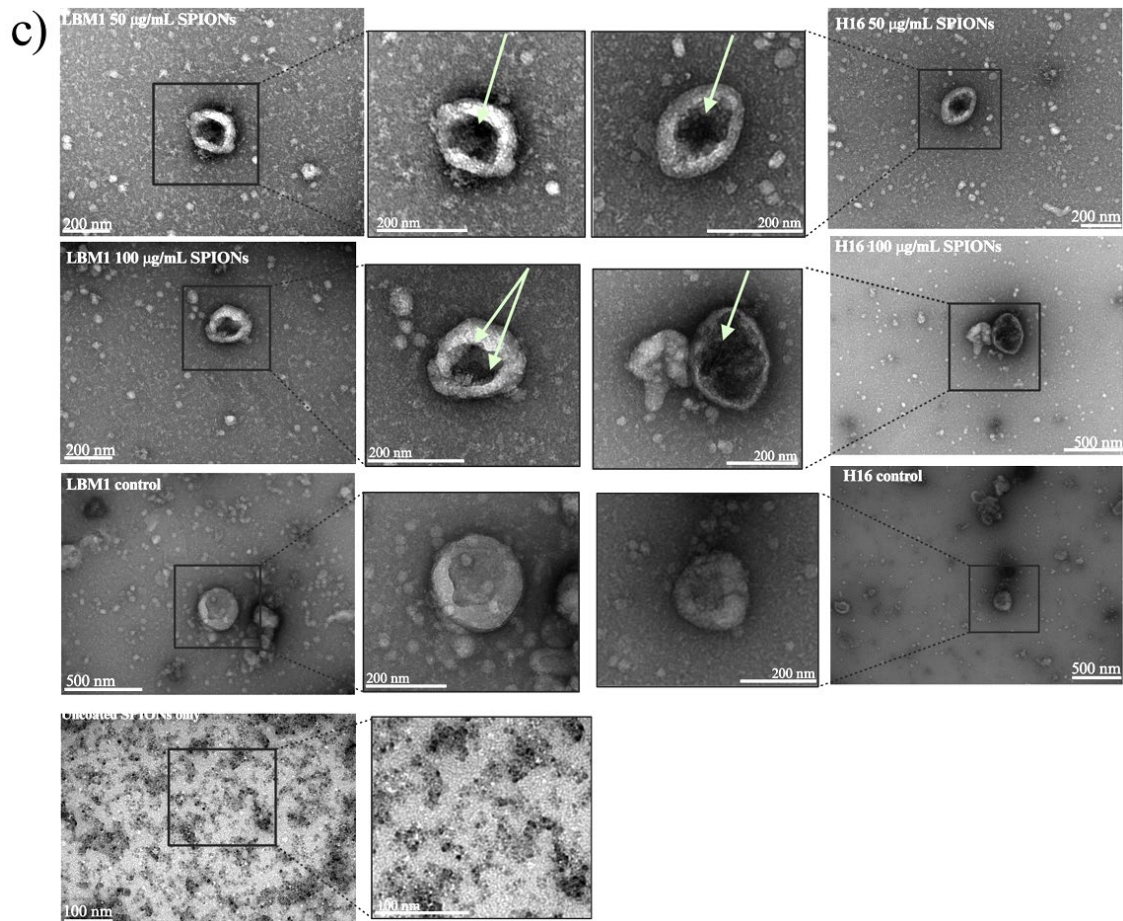
Figure 4.5.2 – Characterization of iron uptake in EVs derived from H16 and LBM1: a)
Iron standard curve depicting colorimetric sample results, analyzed using a
spectrophotometer with absorbance at 595 nm (y-axis), plotted against concentration of iron
(nmol iron/well) (x-axis). The thick grey line represents the standard curve with 0, 2, 4, 6, 8,
and 10 nmol iron/well, while the dotted line presents the standard curve in a linear way. b)
Calculated iron concentration in nmol iron/μg EV. c) TEM images illustrating nanoparticles
in EVs, including an image of uncoated SPIONs without EVs. All SPIONs used in these
results were uncoated. N=1.

4.6 Visualization of Iron in MRI of Agar Phantoms

LBM1 cells were chosen for this experiment because of their high proliferative capacity.
Table 4.6 presents the MRI results of agar phantoms with increasing concentrations of LBM1
cells, both labeled with uncoated SPIONs and unlabeled. The measured T2* and T2
relaxation times for cells and SPION-labeled cells are provided for each concentration. The
T2* and T2 relaxation times for unlabeled cells remained relatively consistent regardless of
concentration. In contrast, the T2* and T2 relaxation times for SPION-labeled cells exhibited
an increase of signal as the cell concentration decreased. Specifically, at a concentration of
4000 cells/μL, no signal was detected ($0,0 \pm 0,0$ ms), suggesting an excessively high iron-

loaded cell concentration. However, signals were reliably detected from 2000 cells/μL and below.

Table 4.6 – MRI results of phantoms with unlabeled LBM1 cells and labeled cells with uncoated SPIONs at a concentration of 200 μg/mL

Cells/μL	T2 (ms) Cells only	T2 (ms) SPION-labeled cells	T2* (ms) Cells only	T2* (ms) SPION-labeled cells
500	104,7 ± 6,6	56,3 ± 1,4	16,1 ± 10,7	2,9 ± 0,1
1000	91,6 ± 8,3	36,1 ± 0,9	13,3 ± 1,7	1,1 ± 0,3
2000	86,2 ± 4,4	11,8 ± 9,1	18,6 ± 3,0	0,1 ± 0,7
4000	89,6 ± 3,4	0,0 ± 0,0	10,5 ± 1,0	0,0 ± 0,0

In **Fig. 4.6.1 a**, no difference in signal was observed among the various concentrations of unlabeled cells. However, in **Fig. 4.6.1 b**, the T2 and T2* map images showed considerably reduced signals for the phantom containing 4000 cells/μL labeled with uncoated SPIONs. This suggests an excessively high concentration of labeled cells, as also seen in **Table 4.6**.
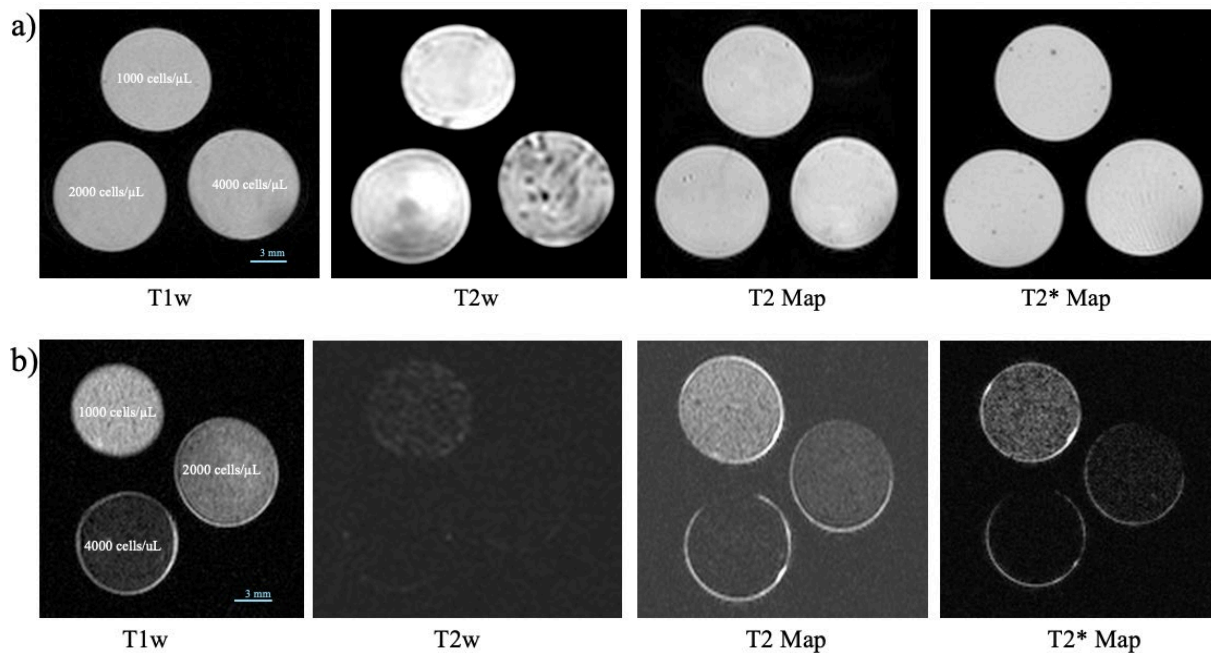
Figure 4.6.1 – MR images of agar phantoms with unlabeled and labeled LBM1 cells. a) unlabeled cells and b) cells labelled with uncoated SPIONs. Both a and b shows a T1-weighted (T1w) image, T2-weighted (T2w) image, T2 map, and T2 map. Different amounts (1000, 2000, and 4000) of cells/μL were imaged. Scale bar=3 mm.*

From the results obtained in **Fig. 4.6.2** it was confirmed that SPION-loaded EVs were detectable in MRI when loaded in a concentrated area of the agarose gel with both EV

volumes of 10 and 20 μL. The EV volume added to the phantoms was taken from isolated

EVs derived from LBM1 cells incubated 24 hours with 100 μg/mL uncoated SPIONs.
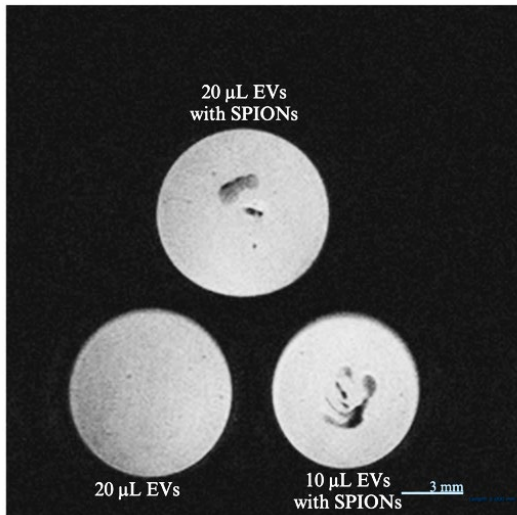
Figure 4.6.2 – MR images of phantoms with LBM1-derived EVs. *Two different volumes (10 and 20 μL SPION-labeled EVs injected into agarose, along with a control with unlabeled EVs. The image is from a T2-weighted image. Scale bar=3 mm.*

5. Discussion

BM remains a major challenge in cancer treatment due to its aggressive nature and limited therapeutic options. Many aspects of how the cancer cells metastasize are poorly understood, which is a limiting factor in the development of diagnostic and therapeutic strategies to prevent the metastatic spread[133]. EVs produced by cancer cells serve as a distinctive form of communication between cells, facilitating cell growth and survival, influencing the TME, and enhancing invasive and metastatic potential[134]. With a focus on being able to track EVs labeled with SPIONs and their role in the metastatic development, this study aimed to optimize SPION-labeling conditions for EVs derived from BM cells *in vitro*. The ultimate goal was to pave the way for future *in vivo* studies for real-time tracking with MRI, with an aim of developing novel targets for intervention and more effective methods of diagnosing and treating BM.

5.1 Comparative Evaluation of Differential Centrifugation and SEC for Isolating EVs

The importance of a good EV isolation method lies in the ability to provide consistent, pure, and representative EV samples of high yield, which is essential for accurate characterization and functional studies. Several techniques are available for isolating EVs, with two of the most common methods being differential centrifugation and SEC. An analysis of EV studies before 2015 revealed that 81% of the studies relied on ultracentrifugation[131]. However, in recent years, its popularity has declined, likely due to technological progress. Methods have been developed which is less time-consuming and labor-intensive. Further, there are potential drawbacks of differential centrifugation such as risk of contamination with similarly sized particles, aggregation of EVs, the method is time-consuming, and the equipment is costly[131,135]. SEC offers several major advantages over differential centrifugation, as it minimizes co-pelleting and aggregation of EVs and provides consistent and reproducible EV yields with high purity[136,137]. Based on a comprehensive assessment, our research group decided to change isolation method from differential centrifugation to SEC in November 2023.

TEM allows for the observation of morphology, size distribution, and internal structures of EVs using only a small amount of sample volume. The smallest EVs, exosomes, typically

appear as cup-shaped or spherical vesicles in the size range of 30-150 nm, while the bigger EVs, microvesicles, are larger (100 nm-1 μm) and have more irregular shapes compared to exosomes[138]. As seen in **Fig. 4.1.1 a**, and **Fig. 4.1.2.1 a**, the TEM analysis revealed cup-shaped EVs, a type of artifact that occur due to the drying process after negative staining. Cryo-TEM studies have demonstrated that EVs exhibit a perfectly spherical structure when observed in aqueous solutions[139]. The small particles observed in the background of the TEM images in **Fig. 4.1.2.1 a** are likely sEVs, but due to limitations of TEM resolution, detecting the membrane structure is challenging.

Based on TEM images for the two isolation methods, the smallest EVs, or exosomes, are predominantly present, as the greatest proportion of EVs reaches up to 200 nm. Although the sizes of EVs generally appear similar between differential centrifugation and SEC, there may be a slight variation in size between the two methods. EVs isolated by SEC tend to be slightly smaller, suggesting a higher proportion of sEVs or exosomes in these samples. Moreover, a slightly greater variation in size is observed in EVs from differential centrifugation, indicating a more heterogenous EV population compared to those seen in SEC TEM images. Considering the TEM findings, the results confirm successful isolation of H16-derived EVs using both differential centrifugation and SEC, and successful isolation of H10- and LBM1-derived EVs using SEC.

TEM can provide an overview of potential contamination and confirm purity; this can be evidenced by the presence of larger vesicles, apoptotic bodies, or cell debris such as aggregates or lipoproteins[140]. Despite its high resolution and capability to provide detailed morphological information, TEM has some limitations, including the need for sample fixation, which may alter the native structure of EVs as size and shape changes, uneven staining, and precipitation of dye crystals. Further, the holes in the grid membrane might be mistaken for sample particles[141]. In addition, the interpretation of TEM images requires expertise in sample preparation and image analysis. Therefore, Western blot and DLS are also used to comprehensively characterize EVs.

DLS is another common technique for determining particle size, which calculates the hydrodynamic radii of particles by analyzing fluctuations in the intensity of scattered light due to Brownian motion. While DLS can characterize particles ranging from 1 nm to 6 μm, its accuracy is best suited to homogenous samples and can be compromised by the presence of

larger particles, as it assumes a single population of particles with uniform size and shape[142]. Therefore, DLS is not an ideal method for analyzing EV size, as EVs consist of heterogenous and polydisperse populations.

The average size analysis of EVs isolated from the three cell lines using DLS showed that EV sizes obtained through SEC were generally smaller (**Fig. 4.1.2.3 a-c**) compared to those of H16-derived EVs via differential centrifugation (**Fig. 4.1.1 c**). These results align with results from the TEM images. EVs isolated through SEC exhibited a small peak below 100 nm and a larger peak above 100 nm, whereas those from differential centrifugation showed a single prominent peak between 100-1000 nm for H16. Both findings indicate a polydisperse sample, making them less suitable for DLS analysis. No notable differences were observed among the three dilutions measured. Triplicate measurements of H16-derived EVs from differential centrifugation showed that the 50x dilution displayed the smallest average and standard deviation (231,3 nm ± 38,0 nm), as shown in **Table 4.1.1**, which may suggest reduced clumping and aggregation. However, this pattern was not consistently observed in EVs isolated through SEC, as indicated in **Table 4.1.2**, with varying averages and standard deviations, suggesting little or no dependence on the dilutions. Despite these findings, the 50x dilution appears to be the most optimal dilution for future DLS analysis of EVs, as it requires the least sample volume. It is important to note that all samples were frozen at -80°C after isolation and left for a few days before being thawed and measured with DLS. This could potentially lead to aggregation, altering the actual size of the EVs.

Another common technique for size determination is nanoparticle tracking analysis (NTA), which involves illuminating nanoparticles in a sample with a laser beam and tracking their Brownian motion using a camera. The movement of individual particles is analyzed to determine their size and concentration. Due to its ability to simultaneously track multiple particles, NTA can characterize polydisperse samples effectively[142,143]. Filipe et al. studied polystyrene beads ranging from 60 to 1000 nm using both NTA and DLS. They found that the mean size values obtained by NTA were slightly smaller and closer to the expected values compared to the z-average provided by DLS. While DLS measurements are quick, non-destructive, and relatively simple, NTA requires several optimization steps by a skilled operator and a larger sample volume. In the context of EV studies, NTA is highly accurate for sizing both monodisperse and polydisperse samples and offers considerably better peak resolution[144]. However, Varga et al. noted the challenge in determining the uncertainty in

NTA measurements due to the high number of parameters involved in data evaluation and the absence of suitable transfer standards for EVs[145]. However, the lack of an NTA instrument at the institution limited the choice to using DLS for the analyses.

Western blot was used to identify common EV marker proteins, including FLOT1, TSG101, CD9, and CD81. Calnexin served as a negative control and was detected exclusively in cells for both isolation methods, for differential centrifugation for H16 (**Fig. 4.1.1 b)** and for SEC for H16, H10, and LBM1 (**Fig. 4.1.2.2**). Interestingly, FLOT1 was found in both cell lysates and EVs across all cell lines for both isolation methods, despite its classification as an EV marker. This observation has been observed in previous research; for example Li and colleagues detected FLOT1 in cell lysates and EVs derived from hepatocytes[146], while Casella et al. reported FLOT1 expression in EVs derived from microglia cells[147]. FLOT1 is a scaffold protein in lipid rafts, involved in intracellular processes such as endocytosis and membrane trafficking[148]. These roles can explain its presence in cell lysates as well as in EV lysates. Further, TSG101 exhibited the strongest expression in cells rather than EVs, which was particularly evident in samples isolated via SEC. Mol and colleagues compared the isolation of cardiomyocyte progenitor cell-derived EVs using differential centrifugation and SEC, observing stronger TSG101 signal in cells compared to EVs from both isolation methods[149]. TSG101 also has essential roles within cells beyond EV formation, including involvement in the ESCRT machinery, endosomal trafficking, and other intracellular processes[150]. These functions can explain its presence in both cell lysates and EV lysates. In contrast, CD9 and CD81 were exclusively positive for EVs, regardless of the isolation method used.

Based on a comprehensive analysis of the results discussed, EVs from H16, H10, and LBM1 have been successfully isolated through SEC, and H16 have been successfully isolated through differential centrifugation.

It has previously been reported that SEC isolation results in a higher EV yield compared to differential centrifugation[151]. This observation is consistent with the findings in **Table 4.1.1.1** and **Table 4.1.2.1**, where the EV yield was 20x higher after SEC isolation compared to differential centrifugation. Mol et al. recently demonstrated that the method of EV isolation can influence their functionality. They found that EVs isolated through SEC were more functional compared to those isolated from differential centrifugation[149]. Interestingly, several studies have suggested that combining both differential centrifugation and SEC yields the

highest quantity of pure and functional EVs[152-154]. However, this approach is more labor-intensive, expensive, and time-consuming compared to using SEC alone. Based on all of the above, SEC was found to be optimal because of its ability to yield higher quantities of EVs while ensuring their purity and functionality.

5.2   Unsuccessful Electroporation of EVs for SPION-Labeling

Several methods are available for directly labeling of EVs to encapsulate nanoparticles within their lumen. These methods include sonication, electroporation, incubation, and fusion, among others[155]. In this experiment, electroporation was used, which involves applying short electrical pulses to create temporary pores in the plasma membrane[156]. Through these pores, drugs or nucleotides can diffuse into the EVs. Additionally, SPIONs can also pass through the temporary pores in the EV membrane, transforming them into magnetic EVs and by this making them suitable for *in vitro* and *in vivo* imaging using MRI[157].

Electroporation has its limitations. The electric current generated during the process can lead to EV aggregation, thereby reducing loading efficiency[158]. Moreover, the high voltage (200 V) may rupture the EV membranes, leading to loss of EV integrity and reduced uptake of nanoparticles. This is supported by TEM images (**Fig. 4.2.1 b)**, where only a few electroporated EVs were detected. The possible aggregation and disruption of EVs might account for the lower iron concentration measured with the iron assay, as shown in **Fig. 4.2.1 a**. Furthermore, it is possible that that the iron nanoparticles themselves aggregated during electroporation, making them less available for uptake by the EVs. In contrast, the passive control, which contained a small amount of iron, showed better iron uptake by EVs compared to the electroporated SPION-EV sample, indicating that incubation with SPIONs without electroporation may result in more efficient iron uptake by EVs.

Concerns persist regarding the potential impact of electroporation on EV functionality. Fuhrmann et al. reported that the overall morphology of EVs remained unchanged following electroporation[159]. Pomatto et al. found no significant loss of native vesicle cargo during electroporation[160], suggesting minimal damage. However, they found a correlation between EV damage and higher voltages. Considering this, lower voltage settings should be explored to assess their effects. However, due to time constraints, the labeling method was promptly switched to natural incubation of cells before EV isolation.

Overall, these findings in addition to our own results suggest that the current application of electroporation has limited efficacy for loading iron nanoparticles into EVs.

5.3 Cellular SPION Uptake and Impact of Dextran-Coated and Uncoated SPIONs on Cell Viability

After unsuccessful electroporation attempts and due to the risk of membrane disruption in EVs, the labeling method was switched to natural cell incubation to avoid manipulating EV membranes. It has been shown that nanoparticles internalized via endocytosis accumulate within MVBs. These MVBs subsequently merge with the plasma membrane, facilitating the release of their cargo (exosomes)[161,162]. It is likely that SPIONs undergo a similar secretion process within the endosomal system.

From an earlier thesis within our research group, Berle demonstrated successful uptake of dextran-coated SPIONs by LBM1 and H16, with an optimal concentration of 10 μg/mL identified for future experiments[163]. However, Busato et al. studied SPION-labeled EVs from stem cells using higher concentrations of uncoated SPIONs (5 nm). Their MRI experiments aimed to determine the maximum nanoparticle concentrations detectable without compromising cell viability and to establish the minimum detectable number of cells labeled with SPIONs. This study found that a concentration of 200 μg/mL combined with 72 hours of incubation resulted in the highest R2 values without affecting cell viability[130]. Based on these findings, SPION concentrations of 50, 100, and 200 μg/mL were selected for these experiments, maintaining consistency between the dextran-coated and uncoated SPIONs.

Microscopic images (**Fig. 4.3.1 a-d**) confirmed successful cellular uptake of both dextran-coated (**Fig. 4.3.1. a-b**) and uncoated (**Fig. 4.3.1 c-d**) SPIONs in both H16 and LBM1 cells. However, there were differences in their impact on cellular viability. Dextran-coated SPION-labeling resulted in greater cell death compared to uncoated SPION-labeling, as evidenced by clumping, aggregation, and fewer cells. These findings align with Umanshankar et al.´s study on the impact of dextran-coated SPIONs on neural stem cell viability, where 20 μg/mL Molday ION dextran-coated SPIONs promoted cell proliferation, while concentrations of 50 μg/mL dextran-coated SPIONs led to decreased cell viability, likely due to elevated intracellular oxidative stress, as indicated by increased reactive oxygen species (ROS) production[164]. SPIONs usually exhibit low cell toxicity, but other *in vitro* studies suggest they

could induce cellular stress, alter gene expression, inhibit cell proliferation, and promote inflammation, depending on the concentration[165]. Cellular iron levels may affect cell viability and EV production, underscoring the importance of optimizing iron concentration, incubation time, and cell viability.

Cell viability following 24 and 48 hours of incubation with uncoated SPIONs appeared comparable for both H16 and LBM1 (**Fig. 4.3.1 c-d**). However, H16 cells exhibited a variation in viability with dextran-coated SPION incubation, showing more viable cells after 24 hours compared to 48 hours (**Fig. 4.3.1 a**). The differences in cell survivability between 24 hours and 48 hours of incubation with dextran-coated SPIONs in LBM1 cells were less pronounced (**Fig. 4.3.1 b**). Given successful cell labeling at both time points and to minimize potential toxicity, the 24-hour SPION incubation period was selected for further experimentation.

The presence of uncoated SPIONs in the cytoplasm of H16 cells was confirmed by TEM, as shown in **Fig. 4.3.2**. The observed localization of SPIONs within endocytic vesicles in the cytoplasm aligns with previous research, which indicates that SPIONs are not found in the nucleus[130,166,167]. While the exact mechanism of SPION cellular uptake remains unclear, the formation of vesicles suggests involvement of endocytic pathways. Inhibition studies have indicated that different endocytic pathways are used depending on the characteristics of the SPIONs: larger nanoparticles are typically incorporated via phagocytosis, while smaller nanoparticles are taken up by pinocytosis[168,169]. Additionally, SPIONs have been shown to be internalized through receptor-mediated endocytosis[170]. Another study demonstrated that different surface coatings can affect impact cellular uptake, independent of nanoparticle size[171]. Therefore, it is likely that the specific pathway of SPION incorporation depends on the nanoparticle´s properties.

Due to time constrains, only H16 cells were incubated with uncoated SPIONs in this experiment, and it was performed only once. Repeating the experiment and including LBM1 cells would be beneficial. Additionally, a quantitative analysis of the iron content within the cells would provide informative results.

5.4   Effects of Dextran-Coated and Uncoated SPIONs on Cell Proliferation

Dabrowska et al. and Gao et al. successfully labeled EVs derived from human bone marrow mesenchymal stem cells using a concentration of 20 µg/mL Molday ION dextran-coated SPIONs[172,173]. Berle used a maximum concentration of 30 µg/mL without observing any signs of cell death[163]. However, current research lacks evidence supporting successful labeling of EVs with higher concentrations (>50 µg/mL) of dextran-coated SPIONs while maintain cell viability and proliferation intact. As discussed in **Section 5.3**, Umanshakar et al. demonstrated cytotoxity at 50 µg/mL of Molday ION dextran-coated SPIONs, while Ma et al. showed that these SPIONs could promote cell proliferation at the concentrations ranging from 12,5 to 50 µg/mL in human dental pulp stem cells *in vitro* but exhibited toxic effects at concentrations exceeding 100 µg/mL. Furthermore, dextran-coated magnetic nanoparticles (MNPs) were found to be cytotoxic to PC-12 cells (derived from a rat pheochromocytoma) at concentrations >100 µg/mL, whereas uncoated maghemite iron oxide nanoparticles showed no cytotoxic effects up to a concentration of 100 µg/mL[174]. **Fig. 4.4.1 a-f** clearly illustrates that even a concentration of 50 µg/mL of dextran-coated SPIONs was too high, which led to cell death in both H16 and LBM1 cell lines. This was further confirmed by a one-way ANOVA analysis, which demonstrated a significant difference in confluency between control cells and cells incubated with dextran-coated SPIONs for both LBM1 and H16 (**Fig. 4.4.1 b, e**). Mahmoudi et al. highlighted several benefits of SPION coating, including prevention of large aggregate formation, preservation of the original structure, and increased blood circulation time[175]. Another factor contributing to cellular cytotoxicity could be the potential release of Rhodamine B, a fluorescent dye component of the SPIONs, at high concentrations, which may exert cytotoxic effects on cells.

Cells incubated with uncoated SPIONs exhibited healthy proliferative tendencies in both H16 and LBM1 cell lines compared to controls. In H16 cells, approximately 80% confluency was achieved after 48 hours across all SPION concentrations, with 200 µg/mL resulted in ~70% confluency (**Fig. 4.4.2 a-c**). LBM1 reached nearly 100% confluency after 48 hours for 50 and 100 µg/mL SPION concentration. However, at 200 µg/mL, proliferation ceased at ~50% confluency (**Fig. 4.4.2 d-f**), indicating an excessively high SPION concentration. As discussed previously in **Section 5.3**, Busato et al. found that stem cell viability was unaffected by incubation with uncoated SPIONs up to a concentration 200 µg/mL[130]. Additionally,

Kutchy et al. demonstrated that incubation with up to 400 µg/mL uncoated SPIONs in astrocytes did not affect the survivability[176]. However, in this case, a concentration of 200 µg/mL appeared to affect normal cell proliferation. A one-way ANOVA was not conducted for the experiments with uncoated SPIONs due to a single replicate, attributed to time limitations.

The larger size of dextran-coated SPIONs (35 nm) compared to uncoated ones (5 nm) can influence their cellular uptake and intracellular trafficking pathways. Larger nanoparticles may be taken up less efficiently by cells and may have different subcellular distribution patterns compared to smaller nanoparticles. These differences in intracellular behavior could impact cytotoxicity and may explain the lower cell viability and proliferation with dextran-coated SPIONs compared to incubation with uncoated SPIONs. In addition, uncoated SPIONs may be more efficiently internalized or processed by the cells. According to Benayas et al., an organic coating like dextran enhances internalization and cell survival at low SPION concentrations. However, at higher doses, a notable decrease in cell viability is typically found. This toxicity could originate from the coating itself, rather than the iron oxide core[177]. These findings support the results of the experiments with dextran-coated SPIONs in this paper, along with previous research on lower concentrations of dextran-coated SPIONs.

In conclusion, incubation with dextran-coated SPIONs at concentrations > 50 µg/mL significantly affected cell proliferation. Conversely, cells incubated with uncoated SPIONs demonstrated healthy and proliferative behavior at concentrations up to 100 µg/mL, with a decrease in proliferative capacity observed at 200 µg/mL.

5.5   Labeling EVs with SPIONs Through Cell Incubation

The iron assay standard curve presented in **Fig. 4.5.1 a-b** for dextran-coated SPIONs and **Fig. 4.5.2 a-b** for uncoated SPIONs clearly indicates the presence of iron in the EV samples. A concentration of 100 µg/mL resulted in the highest measured iron concentration. H16 cells exhibited lower uptake compared to LBM1 (**Fig. 4.5.1 a-b**), consistent with the results observed with uncoated SPIONs (**Fig. 4.5.2 a-b**), possibly due to differences in their capacities to take up and package internalized SPIONs, leading to differences in the amount of iron packed into EVs before secretion. However, it remains unclear whether a higher concentration of SPIONs would have made a difference. As discussed in **Section 5.4**, an

uncoated SPION concentration of 200 µg/mL seemed too excessive for the cells, while the dextran-coated SPION-loaded EVs were nonviable at a concentration of 50 µg/mL. Therefore, it would be prudent to stop working with dextran-coated SPIONs at concentrations > 50 µg/mL and instead proceed with uncoated SPIONs at high concentrations. For future perspectives, it would be valuable to incubate cells with a concentration of 150 µg/mL uncoated SPIONs and confirm their viability and proliferation to achieve the highest and most optimal SPION concentration.

Current research lacks evidence regarding the measurement of iron content inside isolated EVs from cells incubated with SPIONs, where most studies have focused on visual detection of iron using techniques as TEM, super-resolution structured illumination microscopy (SR-SIM), fluorescence microscopy, *in vivo* MRI detection, and Prussian Blue staining. However, Busato et al., utilizing the same uncoated SPIONs as in this study, found that the EVs contained 0,643 µg of iron per 100 µg of EV proteins, equivalent to 0,115 nmol iron/µg EV proteins[130]. They used a concentration of 200 µg/mL SPIONs, which parallels the findings in this study, where approximately 0,07 nmol iron/µg EV proteins were observed for both H16 and LBM1 incubated with 100 µg/mL uncoated SPIONs. If cells were incubated with 150 µg/mL uncoated SPIONs and remained viable and proliferative, it is possible that the iron concentration would be increased to the levels seen in Busato et al., based on the observed trend from 50 µg/mL (0,02-0,03 nmol/µg EV) to 100 µg/mL (0,07 nmol µg/EV) (**Fig. 4.5.2 b**).

SPIONs taken up by EVs are visualized as black areas or dots but can appear different in their arrangement and localization within the EV. Dabrowska et al. studying EV uptake of dextran-coated SPIONs demonstrated TEM images of SPIONs localized in the outer corner of the EV or close to/inside the lipid bilayer, appearing as single black dots[172]. This aligns with the findings in **Fig. 4.5.1 c**, where SPIONs can be visualized towards the outer corner of the EV or within the lipid bilayer membrane. However, the size of the EVs appear smaller in TEM compared to the producer´s stated size of 35 nm, as highlighted in the lowermost TEM image in **Fig. 4.5.1 c** where dextran-coated SPIONs are imaged alone. BioPAL stated that the mean core size of dextran-coated SPIONs were 8 nm, suggesting that the SPION core is more visible than the coating and core together. The control in **Fig. 4.5.1 c** lacks the black dotted areas, further supporting the visualization of SPIONs in the EV-SPION images. Additionally,

performing a fluorescent immunohistochemical (IHC) detection of EV-SPIONs could provide further evidence of successful incorporation of SPIONs into EVs.

SPIONs were also visualized in TEM for EVs with uncoated SPIONs, as presented in **Fig. 4.5.2 c**. However, the SPIONs appeared more centrally localized and clustered compared to the dextran-labeled EVs. This aligns with the study by Busato et al., where uncoated SPIONs were visualized in adipose stem cell-derived EVs, with several SPIONs gathered in one specific area of the EVs and more centralized[130]. The uncoated SPIONs were also imaged alone, presented in the lower part of **Fig. 4.5.2 c**, where the size of the SPIONs aligns with the producer's description of 5 nm.

Overall, both dextran-coated and uncoated SPIONs were visualized within EVs using TEM, and iron was successfully detected in EV samples through iron assay.

5.6   Tracking of SPION-labeled Cells and EVs in Agar Phantoms

Combining MRI with SPION-labeling provides an effective way of tracking cells within the brain[178,179]. T2* sequences are frequently used to track SPION-labeled cells, which can be visualized as local hypointense spots. This is because SPIONs alter the local magnetic field, leading to signal voids or areas of decreased signal intensity on MRI scans[180].

Busato et al. incubated adipose stem cells with 200 μg/mL uncoated SPIONs, ensuring comparable viability to unlabeled cells[130]. Consequently, for this study, the same SPION concentration was used, and the experiment conducted at an earlier stage than the proliferation assay. They tested various cell concentrations (ranging from 10^2 to 10^5) and identified 10^2 as the detection limit[130]. Aasen et al. labeled melanoma BM cells with 200 μg/mL of a nanoprobe (54,4 nm) and detected down to 750 cells/μL in agar phantoms. In this study, concentrations down to 500 cell/μL was examined. However, considering previous research and the lack of signals at 4000 cell/μL in this study (**Table 4.6**), future experiments should prioritize concentrations of 2000, 1000, 500, 250, and 125 cells/μL, along with a control without cells. Given the constraints of time, this experiment was performed only once and needs to be repeated for validation.

To measure the contrast produced by the SPIONs, the values of T2 and T2* were extracted from their corresponding exponential signal decays. **Table 4.6** illustrates minimal differences in T2* values among different concentrations of unlabeled cells, suggesting consistent signal levels. This is also applicable to the results obtained in T2, where signals did not vary a lot among different cell concentrations. These results indicate that different cell concentrations will not change the signals when cells are unlabeled. However, **Table 4.6** presents different signals for SPION-labeled cells based on number of cells labeled. With an increasing signal trend by lower cell concentration, T2 values of SPION-labeled cells should increase to around 70 ms with a cell concentration of 250 cell/μL, which is still lower than T2 for unlabeled 500 cell/μL. Comparable patterns are observed in the T2* signals. This indicates that a lower cell concentration should be tested, possibly as low as 125 cell/μL, which might represent the detection limit.

Fig. 4.6.1 a displays T1w, T2w, T2 map, and T2* map images, revealing no observable differences between 2000 cell/μL (bottom left), 4000 cell/μL (bottom right), and 1000 cell/μL (top). This consistency aligns with the findings in **Table 4.6**. However, the signals are clearly different in images presented in **Fig. 4.6.1 b** where 4000 cell/μL (bottom) resulted in no observable signals, different from 2000 (middle right) and 1000 cell/μL (top).

The golden standard for BM detection is MRI, offering exceptional soft tissue contrast and high-resolution representation of the tissue anatomy[181]. Thorsen et al. demonstrated that T1w high field MRI without contrast can detect metastases as small as 100 μm in size, equivalent to ~40-50 tumor cells determined by histology[182]. MRI is also a suitable method for visualization and tracking of SPION-labeled cells, and it has already been employed successfully to track cells in various disease models[125,183-185]. Sundstrøm et al. administered intracardial injections of SPION-labeled melanoma BM and tracked their distribution over a 24-hour period. They successfully developed a fully automated method for quantifying cancer cells in the brain, facilitating the monitoring of cancer cell dissemination and tumor progression[125].

To our knowledge, there has been limited research on the visualization of SPION-labeled EVs in phantoms. However, Liu et al. recently conducted a study on SPION-labeled human forebrain organoid-derived EVs, using the uncoated SPIONs at a concentration of 500 μg/mL.

They layered unlabeled and labeled EVs in an agar phantom and demonstrated a significant reduction in T2 and T2* values with labeled compared to unlabeled EVs. Labeled EVs exhibited a notable contrast with a homogenous darker layer in comparison to unlabeled EVs[186].

In this study, two different volumes were tested (10 and 20 μL), both of which were visible in MRI as illustrated in **Fig. 4.6.2**. Care was taken to avoid introducing marks of the needle during the addition of EV sample into the agar. Therefore, three different time periods (one, two, and three minutes) were tested, during which the agar stood at RT before the addition of the EV sample. Observations revealed that after two minutes, the agar remained viscous, and the insertion channel melted before solidifying. It is clear that SPION-labeled EVs were detected through MRI in **Fig. 4.6.2** when SPION-EVs are added in a concentrated area of the agar. However, due to time constraints, this experiment was conducted only once and necessitates repetition for validation. Furthermore, this experiment was limited to SPION-labeled EVs derived from LBM1, and the same experiment with H16 still needs to be carried out.

Taken together, this study successfully confirmed the feasibility of loading EVs with SPIONs for the purpose of visualizing on MRI.

Clinical Applications of SPIONs

SPIONs are indeed an interesting research topic, as they can be an attractive platform for cell tracking, tumor diagnosis, and drug delivery due to their unique magnetic properties and potential as theranostic agents. However, for SPIONs to find successful clinical utility, key structural characteristics must be met. These include regulating size, shape, robust magnetic properties, and having the right surface chemistry to ensure compatibility with biological systems[187]. While some SPIONs have received clinical approval for medical applications, questions persist regarding their potential toxicity, particularly following various modifications[188]. The most common investigated clinical application of SPIONs include serving as MRI contrast agents, magnetic hyperthermia, binding antibodies, and drug delivery[189]. The results achieved in clinical applications of SPIONs are promising, though precise feasibility parameters are still required. The main challenges now are to design nanoparticles that remain stable in the bloodstream and to develop surface modifications,

particularly ligands, that enable precise targeting of tumor cells[190]. A study by Jin et al. found that SPIONs show a promising future in clinical applications for imaging cancer metastasis and cell based therapy[191]. However, there is a lack of clinical studies involving SPIONs and BM, highlighting the importance of developing this field.

Conclusion

Overall, this study characterized EVs from three cell lines and demonstrated that SEC is a more efficient EV isolation method and yields a higher quantity of EVs compared to the gold standard, differential centrifugation. Through a comparative analysis of two different SPIONs, the uncoated SPIONs with a concentration of 100 μg/mL were optimal, and natural cell incubation with SPIONs over a 24-hour period showed the most successful uptake. SPIONs were successfully incorporated into H16 and LBM1 cells confirmed by Prussian blue staining and TEM, as well as into H16- and LBM1-derived EVs confirmed by TEM and iron assay. These advancements facilitated the visualization of SPION-labeled cells in agar phantoms using MRI, paving the way towards *in vivo* MRI tracking of BM-derived EVs. The promising results should be followed up with further studies to determine their potential use *in vivo*.

Future aspects

For a more comprehensive understanding of EVs role in metastasis development, and tracking labeled BM-derived EVs, several additional experiments should be performed.

In 1986, Bjerkvig developed a model for making organoids from fetal rat brain cells[192]. Studying organoids derived from 18-day pregnant rat fetuses will provide a viable model for studying BM-derived EVs. Introducing SPION-labeled EVs onto organoids and conducting studies as IHC and Prussian blue staining will provide insights into iron uptake within different cell types of the organoids. Furthermore, it will deepen our understanding of the mechanisms by which EVs operate before the arrival of tumor cells at the site of metastasis. Earlier research predominantly relied on 2D-cultured cell line models to study the role of tumor-derived EVs, which poorly simulate the TME. However, organoids closely resemble physiological cells in composition and behavior, offering a more physiologically relevant platform for investigation prior to *in vivo* studies. Organoids have been successfully used in

drug screening, gene editing, and other fields, and integrating them into EV studies holds promise for advancing our understanding of cancer development and therapeutic strategies[193].

Busato et al. successfully detected EV-SPIONs *in vivo* using MRI following intramuscular injection in the hind limbs[130]. This suggest a potential experiment for future *in vivo* research using the most optimal SPION concentration, likely to be 100 or 150 μg/mL of uncoated SPIONs. Additionally, Busato and colleagues conducted Prussian blue histological examination of extracted muscle tissue, confirming the presence of iron nanoparticles intramuscularly[130]. This experiment could be valuable for future investigation. However, conducting an *in vivo* project for this nature requires a high quantity of EVs, necessitating thorough investigation of organoids *in vitro* prior to proceeding *in vivo*.

To validate the results obtained in the MRI study, triplicate measurements should be conducted making more agar phantoms. These phantoms should include both labeled and unlabeled cells, as well as SPION-labeled EVs, from both LBM1 and H16 cell lines. Furthermore, additional investigation into the highest optimal concentration of uncoated SPIONs should be pursued through triplicate proliferation assay experiments, with 150 μg/mL being considered the potential highest optimal SPION concentration.

In conclusion, the initial future goal is to determine the specific brain cells targeted by SPION-loaded EVs through investigations using organoids. Experiments as Prussian blue staining and IHC can be performed on organoids before advancing to *in viv*o studies. Once a better understanding of EV targeting within the brain´s different cell populations is obtained, the overall future goal is to conduct *in vivo* experiments in a disease model.

References

1. Krieghoff-Henning E, Folkerts J, Penzkofer A, Weg-Remers S. Cancer – an overview. *Med Monatsschr Pharm*. Feb 2017;40(2):48-54. Krebs – ein Überblick.
2. Song Q, Merajver SD, Li JZ. Cancer classification in the genomic era: five contemporary problems. *Hum Genomics*. Oct 19 2015;9:27. doi:10.1186/s40246-015-0049-8
3. Anand P, Kunnumakkara AB, Sundaram C, et al. Cancer is a preventable disease that requires major lifestyle changes. *Pharm Res*. Sep 2008;25(9):2097-116. doi:10.1007/s11095-008-9661-9
4. World Health Organization. Cancer. Updated February 3, 2022. https://www.who.int/news-room/fact-sheets/detail/cancer
5. Prevention CfDCa. Cancer Treatment. Updated May 15, 2023. https://www.cdc.gov/cancer/survivors/patients/treatments.htm
6. Patel A. Benign vs Malignant Tumors. *JAMA Oncology*. 2020;6(9):1488-1488. doi:10.1001/jamaoncol.2020.2592
7. Wan Z, Yin T, Chen H, Li D. Surgical treatment of a retroperitoneal benign tumor surrounding important blood vessels by fractionated resection: A case report and review of the literature. *Oncol Lett*. 2016/05/01 2016;11(5):3259-3264. doi:10.3892/ol.2016.4395
8. Jang SJ, Gardner JM, Ro JY. Diagnostic approach and prognostic factors of cancers. *Adv Anat Pathol*. Mar 2011;18(2):165-72. doi:10.1097/PAP.0b013e31820cb39e
9. Pecorino L. *Molecular biology of cancer : mechanisms, targets, and therapeutics*. 3rd ed. Oxford University Press; 2012.
10. Retsas S. Cancer and the arts: metastasis-as perceived through the ages. *ESMO Open*. 2017;2(3):e000226. doi:10.1136/esmoopen-2017-000226
11. Spano D, Zollo M. Tumor microenvironment: a main actor in the metastasis process. *Clinical & Experimental Metastasis*. 2012/04/01 2012;29(4):381-395. doi:10.1007/s10585-012-9457-5
12. Fares J, Fares MY, Khachfe HH, Salhab HA, Fares Y. Molecular principles of metastasis: a hallmark of cancer revisited. *Signal Transduct Target Ther*. Mar 12 2020;5(1):28. doi:10.1038/s41392-020-0134-x
13. Hanahan D, Weinberg RA. Hallmarks of cancer: the next generation. *Cell*. Mar 4 2011;144(5):646-74. doi:10.1016/j.cell.2011.02.013
14. Shivakoti P. Metastasis Cancer: Symptoms and Diagnosis. *Journal of Tumor Research*. 2022;8(2)doi:10.35248/2684-1258.22.8.172
15. Lyden D, Ghajar CM, Correia AL, et al. Metastasis. *Cancer Cell*. Aug 8 2022;40(8):787-791. doi:10.1016/j.ccell.2022.07.010
16. Psaila B, Lyden D. The metastatic niche: adapting the foreign soil. *Nature Reviews Cancer*. 2009/04/01 2009;9(4):285-293. doi:10.1038/nrc2621
17. Takanori K. *Cancer Metastasis and Cancer Stem Cell/Niche*. Bentham Science Publishers; 2016.
18. Patras L, Paul D, Matei IR. Weaving the nest: extracellular matrix roles in pre-metastatic niche formation. *Front Oncol*. 2023;13:1163786. doi:10.3389/fonc.2023.1163786
19. Liu H, Zhang G, Gao R. Cellular and molecular characteristics of the premetastatic niches. *Animal Model Exp Med*. Oct 2023;6(5):399-408. doi:10.1002/ame2.12356
20. Dong G, Chen P, Xu Y, Liu T, Yin R. Cancer-associated fibroblasts: Key criminals of tumor pre-metastatic niche. *Cancer Letters*. 2023/07/10/ 2023;566:216234. doi:https://doi.org/10.1016/j.canlet.2023.216234
21. Liu Y, Cao X. Characteristics and Significance of the Pre-metastatic Niche. *Cancer Cell*. 2016/11/14/ 2016;30(5):668-681. doi:https://doi.org/10.1016/j.ccell.2016.09.011

22.	Geissler M, Jia W, Kiraz EN, et al. The Brain Pre-Metastatic Niche: Biological and Technical Advancements. *Int J Mol Sci*. Jun 13 2023;24(12)doi:10.3390/ijms241210055

23.	Celià-Terrassa T, Kang Y. Metastatic niche functions and therapeutic opportunities. *Nature Cell Biology*. 2018/08/01 2018;20(8):868-877. doi:10.1038/s41556-018-0145-9

24.	Eslami SZ, Cortés-Hernández LE, Alix-Panabières C. The Metastatic Cascade as the Basis for Liquid Biopsy Development. *Front Oncol*. 2020;10:1055. doi:10.3389/fonc.2020.01055

25.	Dujon AM, Capp JP, Brown JS, et al. Is There One Key Step in the Metastatic Cascade? *Cancers (Basel)*. Jul 22 2021;13(15)doi:10.3390/cancers13153693

26.	Weiss L, Ward PM. Cell detachment and metastasis. *Cancer Metastasis Rev*. 1983;2(2):111-27. doi:10.1007/bf00048965

27.	Weinberg RA. *The biology of cancer*. 2nd ed. Garland Science; 2014.

28.	Makrilia N, Kollias A, Manolopoulos L, Syrigos K. Cell Adhesion Molecules: Role and Clinical Significance in Cancer. *Cancer Investigation*. 2009/11/13 2009;27(10):1023-1037. doi:10.3109/07357900902769749

29.	Liu Q, Zhang H, Jiang X, Qian C, Liu Z, Luo D. Factors involved in cancer metastasis: a better understanding to "seed and soil" hypothesis. *Molecular Cancer*. 2017/12/02 2017;16(1):176. doi:10.1186/s12943-017-0742-4

30.	Théry C, Witwer KW, Aikawa E, et al. Minimal information for studies of extracellular vesicles 2018 (MISEV2018): a position statement of the International Society for Extracellular Vesicles and update of the MISEV2014 guidelines. *J Extracell Vesicles*. 2018;7(1):1535750. doi:10.1080/20013078.2018.1535750

31.	Janiszewska M, Primi MC, Izard T. Cell adhesion in cancer: Beyond the migration of single cells. *J Biol Chem*. Feb 21 2020;295(8):2495-2505. doi:10.1074/jbc.REV119.007759

32.	Tsuruo T, Fujita N. Platelet aggregation in the formation of tumor metastasis. *Proc Jpn Acad Ser B Phys Biol Sci*. 2008;84(6):189-98. doi:10.2183/pjab.84.189

33.	Drapela S, Gomes AP. Metabolic requirements of the metastatic cascade. *Current Opinion in Systems Biology*. 2021/12/01/ 2021;28:100381. doi:https://doi.org/10.1016/j.coisb.2021.100381

34.	Rejniak KA. Circulating Tumor Cells: When a Solid Tumor Meets a Fluid Microenvironment. *Adv Exp Med Biol*. 2016;936:93-106. doi:10.1007/978-3-319-42023-3_5

35.	Gómez-Cuadrado L, Tracey N, Ma R, Qian B, Brunton VG. Mouse models of metastasis: progress and prospects. *Dis Model Mech*. 2017/09// 2017;10(9):1061-1074. doi:10.1242/dmm.030403

36.	Nayak L, Lee EQ, Wen PY. Epidemiology of Brain Metastases. *Current Oncology Reports*. 2012/02/01 2012;14(1):48-54. doi:10.1007/s11912-011-0203-y

37.	Bekaert L, Emery E, Levallet G, Lechapt-Zalcman E. Histopathologic diagnosis of brain metastases: current trends in management and future considerations. *Brain Tumor Pathology*. 2017/01/01 2017;34(1):8-19. doi:10.1007/s10014-016-0275-3

38.	Boire A, Brastianos PK, Garzia L, Valiente M. Brain metastasis. *Nature Reviews Cancer*. 2020/01/01 2020;20(1):4-11. doi:10.1038/s41568-019-0220-y

39.	Smedby KE, Brandt L, Bäcklund ML, Blomqvist P. Brain metastases admissions in Sweden between 1987 and 2006. *Br J Cancer*. Dec 1 2009;101(11):1919-24. doi:10.1038/sj.bjc.6605373

40.	AlTamimi JO, AlJohani HA, Naaman N, Johar RA, Allam TA, Lary DAI. Brain Metastases in Adults: A Five-Year Observational Study From King Abdulaziz Medical City. *Cureus*. Nov 2022;14(11):e31197. doi:10.7759/cureus.31197

41.	Burney IA, Aal Hamad AH, Hashmi SFA, Ahmad N, Pervez N. Evolution of the Management of Brain Metastases: A Bibliometric Analysis. *Cancers (Basel)*. Nov 24 2023;15(23)doi:10.3390/cancers15235570

42.   Noh T, Walbert T. Chapter 6 - Brain metastasis: clinical manifestations, symptom management, and palliative care. In: Schiff D, van den Bent MJ, eds. *Handbook of Clinical Neurology*. Elsevier; 2018:75-88.

43.   Navarro-Olvera JL, Ariñez-Barahona E, Esqueda-Liquidano MA, Muñoz-Cobos A. Brain metastases: Literature review. 10.1016/j.hgmx.2016.04.006. *Revista Médica del Hospital General de México*. 2017;80(1):60-66. doi:10.1016/j.hgmx.2016.04.006

44.   Brenner AW, Patel AJ. Review of Current Principles of the Diagnosis and Management of Brain Metastases. *Front Oncol*. 2022;12:857622. doi:10.3389/fonc.2022.857622

45.   Amsbaugh MJ, Kim CS. Brain Metastasis. *StatPearls*. StatPearls Publishing Copyright © 2023, StatPearls Publishing LLC.; 2023.

46.   Tong E, McCullagh KL, Iv M. Advanced Imaging of Brain Metastases: From Augmenting Visualization and Improving Diagnosis to Evaluating Treatment Response. *Front Neurol*. 2020;11:270. doi:10.3389/fneur.2020.00270

47.   Cohen-Gadol A. Brain Metastsis: What the Patient Needs to Know. Updated September 25, 2023. https://www.aaroncohen-gadol.com/en/patients/brain-metastasis

48.   van den Bent MJ. The role of chemotherapy in brain metastases. *Eur J Cancer*. Oct 2003;39(15):2114-20. doi:10.1016/s0959-8049(03)00577-x

49.   Ahluwalia MS, Vogelbaum MV, Chao ST, Mehta MM. Brain metastasis and treatment. *F1000Prime Rep*. 2014;6:114. doi:10.12703/p6-114

50.   Ahmad A, Khan P, Rehman AU, Batra SK, Nasser MW. Immunotherapy: an emerging modality to checkmate brain metastasis. *Molecular Cancer*. 2023/07/15 2023;22(1):111. doi:10.1186/s12943-023-01818-7

51.   Katano A, Yamashita H. Brain metastasis: Recent treatment modalities and future-perspectives. *Oncol Lett*. Jun 2022;23(6):191. doi:10.3892/ol.2022.13311

52.   Davis FG, Dolecek TA, McCarthy BJ, Villano JL. Toward determining the lifetime occurrence of metastatic brain tumors estimated from 2007 United States cancer incidence data. *Neuro Oncol*. Sep 2012;14(9):1171-7. doi:10.1093/neuonc/nos152

53.   Ivanova M, Porta FM, Giugliano F, et al. Breast Cancer with Brain Metastasis: Molecular Insights and Clinical Management. *Genes (Basel)*. May 26 2023;14(6)doi:10.3390/genes14061160

54.   Koniali L, Hadjisavvas A, Constantinidou A, et al. Risk factors for breast cancer brain metastases: a systematic review. *Oncotarget*. Feb 11 2020;11(6):650-669. doi:10.18632/oncotarget.27453

55.   Kelly WJ, Shah NJ, Subramaniam DS. Management of Brain Metastases in Epidermal Growth Factor Receptor Mutant Non-Small-Cell Lung Cancer. *Front Oncol*. 2018;8:208. doi:10.3389/fonc.2018.00208

56.   Ramanujam S, Schadendorf D, Long GV. Systemic therapies for melanoma brain metastases: which drug for whom and when? *Chinese Clinical Oncology*. 2015;4(2):25.

57.   Tan C, Du X. KRAS mutation testing in metastatic colorectal cancer. *World J Gastroenterol*. Oct 7 2012;18(37):5171-80. doi:10.3748/wjg.v18.i37.5171

58.   Tria SM, Burge ME, Whitehall VLJ. The Therapeutic Landscape for KRAS-Mutated Colorectal Cancers. *Cancers (Basel)*. Apr 19 2023;15(8)doi:10.3390/cancers15082375

59.   Myall NJ, Yu H, Soltys SG, Wakelee HA, Pollom E. Management of brain metastases in lung cancer: evolving roles for radiation and systemic treatment in the era of targeted and immune therapies. *Neurooncol Adv*. Nov 2021;3(Suppl 5):v52-v62. doi:10.1093/noajnl/vdab106

60.   Khan M, Lin J, Liao G, et al. Whole Brain Radiation Therapy Plus Stereotactic Radiosurgery in the Treatment of Brain Metastases Leading to Improved Survival in Patients With Favorable Prognostic Factors. *Front Oncol*. 2019;9:205. doi:10.3389/fonc.2019.00205

61.	Chiarion-Sileni V, Murr R, Pigozzo J, Sarti S, Tomassi O, Romanini A. Brain metastases from malignant melanoma. *Forum (Genova)*. 2003;13(2):170-82; quiz 190.

62.	Diaz MJ, Mark I, Rodriguez D, et al. Melanoma Brain Metastases: A Systematic Review of Opportunities for Earlier Detection, Diagnosis, and Treatment. *Life*. 2023;13(3). doi:10.3390/life13030828

63.	Ene CI, Ferguson SD. Surgical Management of Brain Metastasis: Challenges and Nuances. *Front Oncol*. 2022;12:847110. doi:10.3389/fonc.2022.847110

64.	Tawbi H, To TM, Bartley K, et al. Treatment patterns and clinical outcomes for patients with melanoma and central nervous system metastases: A real-world study. *Cancer Med*. Jan 2022;11(1):139-150. doi:10.1002/cam4.4438

65.	Goulart CR, Mattei TA, Ramina R. Cerebral melanoma metastases: a critical review on diagnostic methods and therapeutic options. *ISRN Surg*. 2011;2011:276908. doi:10.5402/2011/276908

66.	Maldonado KA, Alsayouri K. Physiology, Brain. *StatPearls*. StatPearls Publishing Copyright © 2024, StatPearls Publishing LLC.; 2024.

67.	Rothwell J. Meet the brain neurophysiology. *Int Rev Neurobiol*. 2009;86:51-65. doi:10.1016/s0074-7742(09)86004-2

68.	Colonna M, Butovsky O. Microglia Function in the Central Nervous System During Health and Neurodegeneration. *Annu Rev Immunol*. Apr 26 2017;35:441-468. doi:10.1146/annurev-immunol-051116-052358

69.	Telano LN, Baker S. Physiology, Cerebral Spinal Fluid. *StatPearls*. StatPearls Publishing
Copyright © 2024, StatPearls Publishing LLC.; 2024.

70.	Gawdi R, Shumway KR, Emmady PD. Physiology, Blood Brain Barrier. *StatPearls*. StatPearls Publishing
Copyright © 2024, StatPearls Publishing LLC.; 2024.

71.	Daneman R, Prat A. The blood-brain barrier. *Cold Spring Harb Perspect Biol*. Jan 5 2015;7(1):a020412. doi:10.1101/cshperspect.a020412

72.	Dotiwala AK, McCausland C, Samra NS. Anatomy, Head and Neck: Blood Brain Barrier. *StatPearls*. StatPearls Publishing
Copyright © 2024, StatPearls Publishing LLC.; 2024.

73.	Gao H-m, Chen H, Cui G-Y, Hu J-X. Damage mechanism and therapy progress of the blood-brain barrier after ischemic stroke. *Cell & Bioscience*. 2023/11/01 2023;13(1):196. doi:10.1186/s13578-023-01126-z

74.	Theocharis AD, Skandalis SS, Gialeli C, Karamanos NK. Extracellular matrix structure. *Adv Drug Deliv Rev*. Feb 1 2016;97:4-27. doi:10.1016/j.addr.2015.11.001

75.	Zhang H, Yue X, Chen Z, et al. Define cancer-associated fibroblasts (CAFs) in the tumor microenvironment: new opportunities in cancer immunotherapy and advances in clinical trials. *Molecular Cancer*. 2023/10/02 2023;22(1):159. doi:10.1186/s12943-023-01860-5

76.	Quail DF, Joyce JA. The Microenvironmental Landscape of Brain Tumors. *Cancer Cell*. 2017/03/13/ 2017;31(3):326-341. doi:https://doi.org/10.1016/j.ccell.2017.02.009

77.	Brassart-Pasco S, Brézillon S, Brassart B, Ramont L, Oudart JB, Monboisse JC. Tumor Microenvironment: Extracellular Matrix Alterations Influence Tumor Progression. *Front Oncol*. 2020;10:397. doi:10.3389/fonc.2020.00397

78.	Sobierajska K, Ciszewski WM, Sacewicz-Hofman I, Niewiarowska J. Endothelial Cells in the Tumor Microenvironment. *Adv Exp Med Biol*. 2020;1234:71-86. doi:10.1007/978-3-030-37184-5_6

79.	Li Y, Zhao L, Li XF. Hypoxia and the Tumor Microenvironment. *Technol Cancer Res Treat*. Jan-Dec 2021;20:15330338211036304. doi:10.1177/15330338211036304

80.   Emami Nejad A, Najafgholian S, Rostami A, et al. The role of hypoxia in the tumor microenvironment and development of cancer stem cell: a novel approach to developing treatment. *Cancer Cell International*. 2021/01/20 2021;21(1):62. doi:10.1186/s12935-020-01719-5

81.   Lei X, Lei Y, Li JK, et al. Immune cells within the tumor microenvironment: Biological functions and roles in cancer immunotherapy. *Cancer Lett*. Feb 1 2020;470:126-133. doi:10.1016/j.canlet.2019.11.009

82.   Balta E, Wabnitz GH, Samstag Y. Hijacked Immune Cells in the Tumor Microenvironment: Molecular Mechanisms of Immunosuppression and Cues to Improve T Cell-Based Immunotherapy of Solid Tumors. *Int J Mol Sci*. May 27 2021;22(11)doi:10.3390/ijms22115736

83.   Pereira JFS, Jordan P, Matos P. A Signaling View into the Inflammatory Tumor Microenvironment. *Immuno*. 2021;1(2):91-118.

84.   Zhang J, Veeramachaneni N. Targeting interleukin-1β and inflammation in lung cancer. *Biomarker Research*. 01/27 2022;10doi:10.1186/s40364-021-00341-5

85.   Gurunathan S, Kang MH, Qasim M, Khan K, Kim JH. Biogenesis, Membrane Trafficking, Functions, and Next Generation Nanotherapeutics Medicine of Extracellular Vesicles. *Int J Nanomedicine*. 2021;16:3357-3383. doi:10.2147/ijn.S310357

86.   Doyle LM, Wang MZ. Overview of Extracellular Vesicles, Their Origin, Composition, Purpose, and Methods for Exosome Isolation and Analysis. *Cells*. 2019;8(7):727.

87.   Wolf P. The nature and significance of platelet products in human plasma. *Br J Haematol*. May 1967;13(3):269-88. doi:10.1111/j.1365-2141.1967.tb08741.x

88.   Tang TT, Lv LL, Lan HY, Liu BC. Extracellular Vesicles: Opportunities and Challenges for the Treatment of Renal Diseases. *Front Physiol*. 2019;10:226. doi:10.3389/fphys.2019.00226

89.   Chen J, Tan Q, Yang Z, Jin Y. Engineered extracellular vesicles: potentials in cancer combination therapy. *Journal of Nanobiotechnology*. 2022/03/15 2022;20(1):132. doi:10.1186/s12951-022-01330-y

90.   Hu Q, Su H, Li J, et al. Clinical applications of exosome membrane proteins. *Precis Clin Med*. Mar 2020;3(1):54-66. doi:10.1093/pcmedi/pbaa007

91.   Du S, Guan Y, Xie A, et al. Extracellular vesicles: a rising star for therapeutics and drug delivery. *Journal of Nanobiotechnology*. 2023/07/20 2023;21(1):231. doi:10.1186/s12951-023-01973-5

92.   Ginini L, Billan S, Fridman E, Gil Z. Insight into Extracellular Vesicle-Cell Communication: From Cell Recognition to Intracellular Fate. *Cells*. Apr 19 2022;11(9)doi:10.3390/cells11091375

93.   Bazzan E, Tinè M, Casara A, et al. Critical Review of the Evolution of Extracellular Vesicles' Knowledge: From 1946 to Today. *Int J Mol Sci*. Jun 15 2021;22(12)doi:10.3390/ijms22126417

94.   Li M, Liao L, Tian W. Extracellular Vesicles Derived From Apoptotic Cells: An Essential Link Between Death and Regeneration. *Front Cell Dev Biol*. 2020;8:573511. doi:10.3389/fcell.2020.573511

95.   Zaborowski MP, Balaj L, Breakefield XO, Lai CP. Extracellular Vesicles: Composition, Biological Relevance, and Methods of Study. *Bioscience*. Aug 1 2015;65(8):783-797. doi:10.1093/biosci/biv084

96.   Harmati M, Bukva M, Böröczky T, Buzás K, Gyukity-Sebestyén E. The role of the metabolite cargo of extracellular vesicles in tumor progression. *Cancer Metastasis Rev*. Dec 2021;40(4):1203-1221. doi:10.1007/s10555-021-10014-2

97.   Ghadami S, Dellinger K. The lipid composition of extracellular vesicles: applications in diagnostics and therapeutic delivery. *Front Mol Biosci*. 2023;10:1198044. doi:10.3389/fmolb.2023.1198044

98.   Fischer S, Deindl E. Characterization of RNA in Extracellular Vesicles. *Applied Sciences*. 2021;11(16). doi:10.3390/app11167520

99.   Shahraki K, Boroumand PG, Lotfi H, et al. An update in the applications of exosomes in cancer theranostics: from research to clinical trials. *Journal of Cancer Research and Clinical Oncology*. 2023/08/01 2023;149(10):8087-8116. doi:10.1007/s00432-023-04701-6

100.   Pitt JM, Kroemer G, Zitvogel L. Extracellular vesicles: masters of intercellular communication and potential clinical interventions. *J Clin Invest*. Apr 1 2016;126(4):1139-43. doi:10.1172/jci87316

101.   Robbins PD, Morelli AE. Regulation of immune responses by extracellular vesicles. *Nat Rev Immunol*. Mar 2014;14(3):195-208. doi:10.1038/nri3622

102.   Zeng F, Morelli AE. Extracellular vesicle-mediated MHC cross-dressing in immune homeostasis, transplantation, infectious diseases, and cancer. *Semin Immunopathol*. Sep 2018;40(5):477-490. doi:10.1007/s00281-018-0679-8

103.   Silva AM, Teixeira JH, Almeida MI, Gonçalves RM, Barbosa MA, Santos SG. Extracellular Vesicles: Immunomodulatory messengers in the context of tissue repair/regeneration. *European Journal of Pharmaceutical Sciences*. 2017/02/15/ 2017;98:86-95. doi:https://doi.org/10.1016/j.ejps.2016.09.017

104.   Marar C, Starich B, Wirtz D. Extracellular vesicles in immunomodulation and tumor progression. *Nat Immunol*. May 2021;22(5):560-570. doi:10.1038/s41590-021-00899-0

105.   Jin Y, Ma L, Zhang W, Yang W, Feng Q, Wang H. Extracellular signals regulate the biogenesis of extracellular vesicles. *Biological Research*. 2022/11/26 2022;55(1):35. doi:10.1186/s40659-022-00405-2

106.   Yue M, Hu S, Sun H, et al. Extracellular vesicles remodel tumor environment for cancer immunotherapy. *Molecular Cancer*. 2023/12/13 2023;22(1):203. doi:10.1186/s12943-023-01898-5

107.   Kwok ZH, Wang C, Jin Y. Extracellular Vesicle Transportation and Uptake by Recipient Cells: A Critical Process to Regulate Human Diseases. *Processes (Basel)*. Feb 2021;9(2)doi:10.3390/pr9020273

108.   Arif S, Moulin VJ. Extracellular vesicles on the move: Traversing the complex matrix of tissues. *European Journal of Cell Biology*. 2023/12/01/ 2023;102(4):151372. doi:https://doi.org/10.1016/j.ejcb.2023.151372

109.   Mulcahy LA, Pink RC, Carter DR. Routes and mechanisms of extracellular vesicle uptake. *J Extracell Vesicles*. 2014;3doi:10.3402/jev.v3.24641

110.   Esmaeili A, Alini M, Baghaban Eslaminejad M, Hosseini S. Engineering strategies for customizing extracellular vesicle uptake in a therapeutic context. *Stem Cell Research & Therapy*. 2022/03/28 2022;13(1):129. doi:10.1186/s13287-022-02806-2

111.   Veziroglu EM, Mias GI. Characterizing Extracellular Vesicles and Their Diverse RNA Contents. Review. *Frontiers in Genetics*. 2020-July-17 2020;11doi:10.3389/fgene.2020.00700

112.   Zhang D, Kiomourtzis T, Lam C, Le M. The Biology and Therapeutic Applications of Red Blood Cell Extracellular Vesicles. 2018.

113.   Xu R, Rai A, Chen M, Suwakulsiri W, Greening DW, Simpson RJ. Extracellular vesicles in cancer — implications for future improvements in cancer care. *Nature Reviews Clinical Oncology*. 2018/10/01 2018;15(10):617-638. doi:10.1038/s41571-018-0036-9

114.   Kumar MA, Baba SK, Sadida HQ, et al. Extracellular vesicles as tools and targets in therapy for diseases. *Signal Transduction and Targeted Therapy*. 2024/02/05 2024;9(1):27. doi:10.1038/s41392-024-01735-1

115. Tominaga N, Kosaka N, Ono M, et al. Brain metastatic cancer cells release microRNA-181c-containing extracellular vesicles capable of destructing blood-brain barrier. *Nat Commun*. Apr 1 2015;6:6716. doi:10.1038/ncomms7716

116. Sharma PC, Gupta A. MicroRNAs: potential biomarkers for diagnosis and prognosis of different cancers. *Translational Cancer Research*. 2020;9(9):5798-5818.

117. Rigg E, Wang J, Xue Z, et al. Inhibition of extracellular vesicle-derived miR-146a-5p decreases progression of melanoma brain metastasis via Notch pathway dysregulation in astrocytes. *J Extracell Vesicles*. Oct 2023;12(10):e12363. doi:10.1002/jev2.12363

118. van Geuns R-JM, Wielopolski PA, de Bruin HG, et al. Basic principles of magnetic resonance imaging. *Progress in Cardiovascular Diseases*. 1999/09/01/ 1999;42(2):149-156. doi:https://doi.org/10.1016/S0033-0620(99)70014-9

119. Inoue T, Kozawa E, Ishikawa M, Okada H. Application of Magnetic Resonance Imaging in the Evaluation of Nutritional Status: A Literature Review with Focus on Dialysis Patients. *Nutrients*. Jun 14 2021;13(6)doi:10.3390/nu13062037

120. Pai A, Shetty R, Hodis B, Chowdhury YS. Magnetic Resonance Imaging Physics. *StatPearls*. StatPearls Publishing
Copyright © 2024, StatPearls Publishing LLC.; 2024.

121. Berger A. Magnetic resonance imaging. *Bmj*. Jan 5 2002;324(7328):35. doi:10.1136/bmj.324.7328.35

122. Seeger LL. Physical principles of magnetic resonance imaging. *Clin Orthop Relat Res*. Jul 1989;(244):7-16.

123. Chavhan GB, Babyn PS, Thomas B, Shroff MM, Haacke EM. Principles, techniques, and applications of T2*-based MR imaging and its special applications. *Radiographics*. Sep-Oct 2009;29(5):1433-49. doi:10.1148/rg.295095034

124. Tada Y, C. Yang P. Iron Oxide Labeling and Tracking of Extracellular Vesicles. *Magnetochemistry*. 2019;5(4):60.

125. Sundstrøm T, Daphu I, Wendelbo I, et al. Automated tracking of nanoparticle-labeled melanoma cells improves the predictive power of a brain metastasis model. *Cancer Res*. Apr 15 2013;73(8):2445-56. doi:10.1158/0008-5472.Can-12-3514

126. Corot C, Warlin D. Superparamagnetic iron oxide nanoparticles for MRI: contrast media pharmaceutical company R&D perspective. *Wiley Interdiscip Rev Nanomed Nanobiotechnol*. Sep-Oct 2013;5(5):411-22. doi:10.1002/wnan.1225

127. Heyn C, Ronald JA, Mackenzie LT, et al. In vivo magnetic resonance imaging of single cells in mouse brain with optical validation. *Magn Reson Med*. Jan 2006;55(1):23-9. doi:10.1002/mrm.20747

128. Komuro H, Aminova S, Lauro K, Harada M. Advances of engineered extracellular vesicles-based therapeutics strategy. *Sci Technol Adv Mater*. 2022;23(1):655-681. doi:10.1080/14686996.2022.2133342

129. Welsh JA, Goberdhan DCI, O'Driscoll L, et al. Minimal information for studies of extracellular vesicles (MISEV2023): From basic to advanced approaches. *Journal of Extracellular Vesicles*. 2024;13(2):e12404. doi:https://doi.org/10.1002/jev2.12404

130. Busato A, Bonafede R, Bontempi P, et al. Magnetic resonance imaging of ultrasmall superparamagnetic iron oxide-labeled exosomes from stem cells: a new method to obtain labeled exosomes. *Int J Nanomedicine*. 2016;11:2481-90. doi:10.2147/ijn.S104152

131. Sidhom K, Obi PO, Saleem A. A Review of Exosomal Isolation Methods: Is Size Exclusion Chromatography the Best Option? *Int J Mol Sci*. Sep 4 2020;21(18)doi:10.3390/ijms21186466

132. Lennaárd AJ, Mamand DR, Wiklander RJ, El Andaloussi S, Wiklander OPB. Optimised Electroporation for Loading of Extracellular Vesicles with Doxorubicin. *Pharmaceutics*. Dec 24 2021;14(1)doi:10.3390/pharmaceutics14010038

133. Busatto S, Yang Y, Walker SA, et al. Brain metastases-derived extracellular vesicles induce binding and aggregation of low-density lipoprotein. *Journal of Nanobiotechnology*. 2020/11/07 2020;18(1):162. doi:10.1186/s12951-020-00722-2

134. Chang WH, Cerione RA, Antonyak MA. Extracellular Vesicles and Their Roles in Cancer Progression. *Methods Mol Biol*. 2021;2174:143-170. doi:10.1007/978-1-0716-0759-6_10

135. Yu LL, Zhu J, Liu JX, et al. A Comparison of Traditional and Novel Methods for the Separation of Exosomes from Human Samples. *Biomed Res Int*. 2018;2018:3634563. doi:10.1155/2018/3634563

136. Corso G, Mäger I, Lee Y, et al. Reproducible and scalable purification of extracellular vesicles using combined bind-elute and size exclusion chromatography. *Sci Rep*. Sep 14 2017;7(1):11561. doi:10.1038/s41598-017-10646-x

137. Böing AN, van der Pol E, Grootemaat AE, Coumans FA, Sturk A, Nieuwland R. Single-step isolation of extracellular vesicles by size-exclusion chromatography. *J Extracell Vesicles*. 2014;3doi:10.3402/jev.v3.23430

138. Gurung S, Perocheau D, Touramanidou L, Baruteau J. The exosome journey: from biogenesis to uptake and intracellular signalling. *Cell Communication and Signaling*. 2021/04/23 2021;19(1):47. doi:10.1186/s12964-021-00730-1

139. Jung MK, Mun JY. Sample Preparation and Imaging of Exosomes by Transmission Electron Microscopy. *J Vis Exp*. Jan 4 2018;(131)doi:10.3791/56482

140. Di Bella MA. Overview and Update on Extracellular Vesicles: Considerations on Exosomes and Their Application in Modern Medicine. *Biology (Basel)*. May 24 2022;11(6)doi:10.3390/biology11060804

141. Malenica M, Vukomanović M, Kurtjak M, et al. Perspectives of Microscopy Methods for Morphology Characterisation of Extracellular Vesicles from Human Biofluids. *Biomedicines*. May 26 2021;9(6)doi:10.3390/biomedicines9060603

142. Li X, Corbett AL, Taatizadeh E, et al. Challenges and opportunities in exosome research-Perspectives from biology, engineering, and cancer therapy. *APL Bioeng*. Mar 2019;3(1):011503. doi:10.1063/1.5087122

143. Sałaga-Zaleska K, Kuchta A, Bzoma B, et al. Nanoparticle Tracking Analysis of Urinary Extracellular Vesicle Proteins as a New Challenge in Laboratory Medicine. *International Journal of Molecular Sciences*. 2023;24(15):12228.

144. Filipe V, Hawe A, Jiskoot W. Critical Evaluation of Nanoparticle Tracking Analysis (NTA) by NanoSight for the Measurement of Nanoparticles and Protein Aggregates. *Pharmaceutical Research*. 2010/05/01 2010;27(5):796-810. doi:10.1007/s11095-010-0073-2

145. Varga Z, Yuana Y, Grootemaat AE, et al. Towards traceable size determination of extracellular vesicles. *Journal of Extracellular Vesicles*. 2014;3(1):23298. doi:https://doi.org/10.3402/jev.v3.23298

146. Li X, Chen R, Kemper S, Brigstock DR. Structural and Functional Characterization of Fibronectin in Extracellular Vesicles From Hepatocytes. *Front Cell Dev Biol*. 2021;9:640667. doi:10.3389/fcell.2021.640667

147. Casella G, Colombo F, Finardi A, et al. Extracellular Vesicles Containing IL-4 Modulate Neuroinflammation in a Mouse Model of Multiple Sclerosis. *Molecular Therapy*. 2018/09/05/ 2018;26(9):2107-2118. doi:https://doi.org/10.1016/j.ymthe.2018.06.024

148. Zhan Z, Ye M, Jin X. The roles of FLOT1 in human diseases (Review). *Mol Med Rep*. 2023/11/01 2023;28(5):212. doi:10.3892/mmr.2023.13099

149. Mol EA, Goumans M-J, Doevendans PA, Sluijter JPG, Vader P. Higher functionality of extracellular vesicles isolated using size-exclusion chromatography compared to ultracentrifugation. *Nanomedicine: Nanotechnology, Biology and Medicine*. 2017/08/01/ 2017;13(6):2061-2065. doi:https://doi.org/10.1016/j.nano.2017.03.011

150.   Ferraiuolo R-M, Manthey KC, Stanton MJ, Triplett AA, Wagner K-U. The Multifaceted Roles of the Tumor Susceptibility Gene 101 (TSG101) in Normal Development and Disease. *Cancers*. 2020;12(2). doi:10.3390/cancers12020450

151.   Takov K, Yellon DM, Davidson SM. Comparison of small extracellular vesicles isolated from plasma by ultracentrifugation or size-exclusion chromatography: yield, purity and functional potential. *J Extracell Vesicles*. 2019;8(1):1560809. doi:10.1080/20013078.2018.1560809

152.   Thomas S, Kaur J, Kamboj R, et al. Investigate the efficacy of size exclusion chromatography for the isolation of extracellular vesicles from C. elegans. *Journal of Chromatography B*. 2024/02/01/ 2024;1233:123982. doi:https://doi.org/10.1016/j.jchromb.2023.123982

153.   Wei R, Zhao L, Kong G, et al. Combination of Size-Exclusion Chromatography and Ultracentrifugation Improves the Proteomic Profiling of Plasma-Derived Small Extracellular Vesicles. *Biological Procedures Online*. 2020/06/23 2020;22(1):12. doi:10.1186/s12575-020-00125-5

154.   An M, Wu J, Zhu J, Lubman DM. Comparison of an Optimized Ultracentrifugation Method versus Size-Exclusion Chromatography for Isolation of Exosomes from Human Serum. *J Proteome Res*. Oct 5 2018;17(10):3599-3605. doi:10.1021/acs.jproteome.8b00479

155.   Liu Q, Huang J, Xia J, Liang Y, Li G. Tracking tools of extracellular vesicles for biomedical research. *Front Bioeng Biotechnol*. 2022;10:943712. doi:10.3389/fbioe.2022.943712

156.   Kumar P, Nagarajan A, Uchil PD. Electroporation. *Cold Spring Harb Protoc*. Jul 1 2019;2019(7)doi:10.1101/pdb.top096271

157.   Hu L, Wickline SA, Hood JL. Magnetic resonance imaging of melanoma exosomes in lymph nodes. *Magn Reson Med*. Jul 2015;74(1):266-271. doi:10.1002/mrm.25376

158.   Danilushkina AA, Emene CC, Barlev NA, Gomzikova MO. Strategies for Engineering of Extracellular Vesicles. *Int J Mol Sci*. Aug 26 2023;24(17)doi:10.3390/ijms241713247

159.   Fuhrmann G, Serio A, Mazo M, Nair R, Stevens MM. Active loading into extracellular vesicles significantly improves the cellular uptake and photodynamic effect of porphyrins. *J Control Release*. May 10 2015;205:35-44. doi:10.1016/j.jconrel.2014.11.029

160.   Pomatto MAC, Bussolati B, D'Antico S, et al. Improved Loading of Plasma-Derived Extracellular Vesicles to Encapsulate Antitumor miRNAs. *Mol Ther Methods Clin Dev*. Jun 14 2019;13:133-144. doi:10.1016/j.omtm.2019.01.001

161.   Malatesta M, Giagnacovo M, Costanzo M, et al. Diaminobenzidine photoconversion is a suitable tool for tracking the intracellular location of fluorescently labelled nanoparticles at transmission electron microscopy. *Eur J Histochem*. Apr 16 2012;56(2):e20. doi:10.4081/ejh.2012.20

162.   Keller S, Sanderson MP, Stoeck A, Altevogt P. Exosomes: From biogenesis and secretion to biological function. *Immunology Letters*. 2006/11/15/ 2006;107(2):102-108. doi:https://doi.org/10.1016/j.imlet.2006.09.005

163.   Berle BF. *3D Modelling of Brain Metastasis Microenvironment for Evaluation of Tumour-Stromal Interactions*. University of Bergen; 2023. https://hdl.handle.net/11250/3073289

164.   Umashankar A, Corenblum MJ, Ray S, et al. Effects of the iron oxide nanoparticle Molday ION Rhodamine B on the viability and regenerative function of neural stem cells: relevance to clinical translation. *Int J Nanomedicine*. 2016;11:1731-48. doi:10.2147/ijn.S102006

165.   Tada Y, C. Yang P. Iron Oxide Labeling and Tracking of Extracellular Vesicles. *Magnetochemistry*. 2019;5(4). doi:10.3390/magnetochemistry5040060

166.	Sun R, Dittrich J, Le-Huu M, et al. Physical and Biological Characterization of Superparamagnetic Iron Oxide- and Ultrasmall Superparamagnetic Iron Oxide-Labeled Cells: A Comparison. *Investigative Radiology*. 2005;40(8)

167.	Gu J, Xu H, Han Y, et al. The internalization pathway, metabolic fate and biological effect of superparamagnetic iron oxide nanoparticles in the macrophage-like RAW264.7 cell. *Science China Life Sciences*. 2011/09/01 2011;54(9):793-805. doi:10.1007/s11427-011-4215-5

168.	Fleige G, Seeberger F, Laux D, et al. In Vitro Characterization of Two Different Ultrasmall Iron Oxide Particles for Magnetic Resonance Cell Tracking. *Investigative Radiology*. 2002;37(9)

169.	Alam SR, Stirrat C, Richards J, et al. Vascular and plaque imaging with ultrasmall superparamagnetic particles of iron oxide. *J Cardiovasc Magn Reson*. Sep 18 2015;17(1):83. doi:10.1186/s12968-015-0183-4

170.	Schulze E, Ferrucci JT, Jr., Poss K, Lapointe L, Bogdanova A, Weissleder R. Cellular uptake and trafficking of a prototypical magnetic iron oxide label in vitro. *Invest Radiol*. Oct 1995;30(10):604-10. doi:10.1097/00004424-199510000-00006

171.	Saito S, Tsugeno M, Koto D, et al. Impact of surface coating and particle size on the uptake of small and ultrasmall superparamagnetic iron oxide nanoparticles by macrophages. *Int J Nanomedicine*. 2012;7:5415-21. doi:10.2147/ijn.S33709

172.	Dabrowska S, Del Fattore A, Karnas E, et al. Imaging of extracellular vesicles derived from human bone marrow mesenchymal stem cells using fluorescent and magnetic labels. *International Journal of Nanomedicine*. 2018/03/19 2018;13(null):1653-1664. doi:10.2147/IJN.S159404

173.	Gao Y, Jablonska A, Chu C, Walczak P, Janowski M. Mesenchymal Stem Cells Do Not Lose Direct Labels Including Iron Oxide Nanoparticles and DFO-89Zr Chelates through Secretion of Extracellular Vesicles. *Membranes*. 2021;11(7). doi:10.3390/membranes11070484

174.	Marcus M, Karni M, Baranes K, et al. Iron oxide nanoparticles for neuronal cell applications: uptake study and magnetic manipulations. *J Nanobiotechnology*. May 14 2016;14(1):37. doi:10.1186/s12951-016-0190-0

175.	Mahmoudi M, Sant S, Wang B, Laurent S, Sen T. Superparamagnetic iron oxide nanoparticles (SPIONs): Development, surface modification and applications in chemotherapy. *Advanced Drug Delivery Reviews*. 2011/01/01 2011;63(1):24-46. doi:https://doi.org/10.1016/j.addr.2010.05.006

176.	Kutchy NA, Ma R, Liu Y, Buch S, Hu G. Extracellular Vesicle-Mediated Delivery of Ultrasmall Superparamagnetic Iron Oxide Nanoparticles to Mice Brain. *Front Pharmacol*. 2022;13:819516. doi:10.3389/fphar.2022.819516

177.	Benayas E, Espinosa A, Portolés MT, Vila-del Sol V, Morales MP, Serrano MC. Cellular and Molecular Processes Are Differently Influenced in Primary Neural Cells by Slight Changes in the Physicochemical Properties of Multicore Magnetic Nanoparticles. *ACS Applied Materials & Interfaces*. 2023/04/12 2023;15(14):17726-17741. doi:10.1021/acsami.3c02729

178.	Bulte JWM. In Vivo MRI Cell Tracking: Clinical Studies. *American Journal of Roentgenology*. 2009/08/01 2009;193(2):314-325. doi:10.2214/AJR.09.3107

179.	Arbab AS, Janic B, Haller J, Pawelczyk E, Liu W, Frank JA. In Vivo Cellular Imaging for Translational Medical Research. *Curr Med Imaging Rev*. Feb 1 2009;5(1):19-38. doi:10.2174/157340509787354697

180.	Huang J, Zhong X, Wang L, Yang L, Mao H. Improving the magnetic resonance imaging contrast and detection methods with engineered magnetic nanoparticles. *Theranostics*. 2012;2(1):86-102. doi:10.7150/thno.4006

181.   Derks S, van der Veldt AAM, Smits M. Brain metastases: the role of clinical imaging. *Br J Radiol*. Feb 1 2022;95(1130):20210944. doi:10.1259/bjr.20210944

182.   Thorsen F, Fite B, Mahakian LM, et al. Multimodal imaging enables early detection and characterization of changes in tumor permeability of brain metastases. *J Control Release*. Dec 28 2013;172(3):812-22. doi:10.1016/j.jconrel.2013.10.019

183.   Lee D, Sohn J, Kirichenko A. Quantifying Liver Heterogeneity via R2*-MRI with Super-Paramagnetic Iron Oxide Nanoparticles (SPION) to Characterize Liver Function and Tumor. *Cancers (Basel)*. Oct 27 2022;14(21)doi:10.3390/cancers14215269

184.   Talluri S, Malla RR. Superparamagnetic Iron Oxide Nanoparticles (SPIONs) for Diagnosis and Treatment of Breast, Ovarian and Cervical Cancers. *Curr Drug Metab*. 2019;20(12):942-945. doi:10.2174/1389200220666191016124958

185.   Sillerud LO, Solberg NO, Chamberlain R, et al. SPION-enhanced magnetic resonance imaging of Alzheimer's disease plaques in AβPP/PS-1 transgenic mouse brain. *J Alzheimers Dis*. 2013;34(2):349-65. doi:10.3233/jad-121171

186.   Liu C, Helsper S, Marzano M, et al. Human Forebrain Organoid-Derived Extracellular Vesicle Labeling with Iron Oxides for In Vitro Magnetic Resonance Imaging. *Biomedicines*. 2022;10(12). doi:10.3390/biomedicines10123060

187.   Lin MM, Kim DK, Haj AJE, Dobson J. Development of Superparamagnetic Iron Oxide Nanoparticles (SPIONS) for Translation to Clinical Applications. *IEEE Transactions on NanoBioscience*. 2008;7(4):298-305. doi:10.1109/TNB.2008.2011864

188.   Wei H, Hu Y, Wang J, Gao X, Qian X, Tang M. Superparamagnetic Iron Oxide Nanoparticles: Cytotoxicity, Metabolism, and Cellular Behavior in Biomedicine Applications. *Int J Nanomedicine*. 2021;16:6097-6113. doi:10.2147/ijn.S321984

189.   Dulińska-Litewka J, Łazarczyk A, Hałubiec P, Szafrański O, Karnas K, Karewicz A. Superparamagnetic Iron Oxide Nanoparticles-Current and Prospective Medical Applications. *Materials (Basel)*. Feb 19 2019;12(4)doi:10.3390/ma12040617

190.   Musielak M, Piotrowski I, Suchorska WM. Superparamagnetic iron oxide nanoparticles (SPIONs) as a multifunctional tool in various cancer therapies. *Rep Pract Oncol Radiother*. Jul-Aug 2019;24(4):307-314. doi:10.1016/j.rpor.2019.04.002

191.   Jin R, Lin B, Li D, Ai H. Superparamagnetic iron oxide nanoparticles for MR imaging and therapy: design considerations and clinical applications. *Current Opinion in Pharmacology*. 2014/10/01/ 2014;18:18-27. doi:https://doi.org/10.1016/j.coph.2014.08.002

192.   Bjerkvig R. Reaggregation of Fetal Rat Brain Cells in a Stationary Culture System II: Ultrastructural Characterization. *In Vitro Cellular & Developmental Biology*. 1986;22(4):193-200.

193.   Zhang Y, Lu A, Zhuang Z, et al. Can Organoid Model Reveal a Key Role of Extracellular Vesicles in Tumors? A Comprehensive Review of the Literature. *Int J Nanomedicine*. 2023;18:5511-5527. doi:10.2147/ijn.S424737